

Nano- and Biomaterials for Sustainable Development

Guest Editors: An-Ya Lo, Chuan Wang, Wei Hsuan Hung, Anmin Zheng, and Biswarup Sen





Nano- and Biomaterials for Sustainable Development

Journal of Nanomaterials

Nano- and Biomaterials for Sustainable Development

Guest Editors: An-Ya Lo, Chuan Wang, Wei Hsuan Hung,
Anmin Zheng, and Biswarup Sen



Copyright © 2015 Hindawi Publishing Corporation. All rights reserved.

This is a special issue published in "Journal of Nanomaterials." All articles are open access articles distributed under the Creative Commons Attribution License, which permits unrestricted use, distribution, and reproduction in any medium, provided the original work is properly cited.

Editorial Board

Katerina Aifantis, Greece
Nageh K. Allam, USA
Margarida Amaral, Portugal
Xuedong Bai, China
Enrico Bergamaschi, Italy
Theodorian Borca-Tasciuc, USA
C. Jeffrey Brinker, USA
Christian Brosseau, France
Xuebo Cao, China
Sang-Hee Cho, Republic of Korea
Shafiq Chowdhury, USA
Cui Chunxiang, China
Miguel A. Correa-Duarte, Spain
Shadi A. Dayeh, USA
Ali Eftekhari, USA
Claude Estournes, France
Alan Fuchs, USA
Lian Gao, China
Russell E. Gorga, USA
Hongchen Chen Gu, China
Mustafa O. Guler, Turkey
John Zhanhu Guo, USA
Smrati Gupta, Germany
Michael Harris, USA
Zhongkui Hong, USA
Michael Z. Hu, USA
David Hui, USA
Y.-K. Jeong, Republic of Korea
Sheng-Rui Jian, Taiwan
Wanqin Jin, China
Rakesh K. Joshi, India
Zhenhui Kang, China

Fathallah Karimzadeh, Iran
Do Kyung Kim, Republic of Korea
Kin Tak Lau, Australia
Burtrand Lee, USA
Benxia Li, China
Jun Li, Singapore
Shijun Liao, China
Gong Ru Lin, Taiwan
J.-Y. Liu, USA
Jun Liu, USA
Tianxi Liu, China
Songwei Lu, USA
Daniel Lu, China
Jue Lu, USA
Ed Ma, USA
Gaurav Mago, USA
Sanjay R. Mathur, Germany
Nobuhiro Matsushita, Japan
A. McCormick, USA
Vikas Mittal, UAE
Weihai Ni, Germany
Sherine Obare, USA
Edward Andrew Payzant, USA
Kui-Qing Peng, China
Anukorn Phuruangrat, Thailand
Ugur Serincan, Turkey
Huaiyu Shao, Japan
Donglu Shi, USA
Suprakas Sinha Ray, South Africa
Vladimir Sivakov, Germany
Marinella Striccoli, Italy
Bohua Sun, South Africa

Saikat Talapatra, USA
Nairong Tao, China
Titipun Thongtem, Thailand
Somchai Thongtem, Thailand
Valeri P. Tolstoy, Russia
Tsung-Yen Tsai, Taiwan
Takuya Tsuzuki, Australia
Raquel Verdejo, Spain
Mat U. Wahit, Malaysia
Shiren Wang, USA
Yong Wang, USA
Cheng Wang, China
Zhenbo Wang, China
Jinquan Wei, China
Ching Ping Wong, USA
Xingcai Wu, China
Guodong Xia, Hong Kong
Zhi Li Xiao, USA
Ping Xiao, UK
Shuangxi Xing, China
Yangchuan Xing, USA
N. Xu, China
Doron Yadlovker, Israel
Ying-Kui Yang, China
Khaled Youssef, USA
Kui Yu, Canada
Haibo Zeng, China
Tianyou Zhai, Japan
Renyun Zhang, Sweden
Yanbao Zhao, China
Lianxi Zheng, Singapore
Chunyi Zhi, Japan

Contents

Nano- and Biomaterials for Sustainable Development, An-Ya Lo, Chuan Wang, Wei Hsuan Hung, Anmin Zheng, and Biswarup Sen
Volume 2015, Article ID 129894, 2 pages

Biocomposite of Cassava Starch Reinforced with Cellulose Pulp Fibers Modified with Deposition of Silica (SiO₂) Nanoparticles, Joabel Raabe, Alessandra de Souza Fonseca, Lina Bufalino, Caue Ribeiro, Maria Alice Martins, José Manoel Marconcini, Lourival M. Mendes, and Gustavo Henrique Denzin Tonoli
Volume 2015, Article ID 493439, 9 pages

Biosynthesis of Anisotropic Silver Nanoparticles by *Bhargavaea indica* and Their Synergistic Effect with Antibiotics against Pathogenic Microorganisms, Priyanka Singh, Yeon Ju Kim, Hina Singh, Ramya Mathiyalagan, Chao Wang, and Deok Chun Yang
Volume 2015, Article ID 234741, 10 pages

Organic Systems and Their Photorefractive Properties under the Nano- and Biostructuration: Scientific View and Sustainable Development, Natalia V. Kamanina, Sergey V. Serov, Yann Bretonniere, and Chantal Andraud
Volume 2015, Article ID 278902, 5 pages

Sustainable Nanopozzolan Modified Cement: Characterizations and Morphology of Calcium Silicate Hydrate during Hydration, N. Mohamed Sutan, I. Yakub, M. S. Jaafar, K. A. Matori, and S. K. Sahari
Volume 2015, Article ID 713258, 6 pages

Study of the Plasmon Energy Transfer Processes in Dye Sensitized Solar Cells, Tzu-ming Chien, Prathamesh Pavaskar, Wei Hsuan Hung, Stephen Cronin, Sheing-Hui Chiu, and Sz-Nian Lai
Volume 2015, Article ID 139243, 6 pages

Acute Toxicity of Double-Walled Carbon Nanotubes to Three Aquatic Organisms, Lungile P. Lukhele, Bhekie B. Mamba, Ndeke Musee, and Victor Wepener
Volume 2015, Article ID 219074, 19 pages

Editorial

Nano- and Biomaterials for Sustainable Development

An-Ya Lo,¹ Chuan Wang,² Wei Hsuan Hung,³ Anmin Zheng,⁴ and Biswarup Sen⁵

¹Department of Chemical and Materials Engineering, National Chin-Yi University of Technology, Taichung 41170, Taiwan

²Electrical and Computer Engineering, Michigan State University, East Lansing, MI 48824-1226, USA

³Department of Materials Science and Engineering, Feng Chia University, Taichung 40724, Taiwan

⁴Wuhan Institute of Physics and Mathematics, Chinese Academy of Sciences, Wuhan 430071, China

⁵Amity Institute of Biotechnology, Amity University Haryana, Gurgaon 122413, India

Correspondence should be addressed to An-Ya Lo; a.y.lo1125@gmail.com and Biswarup Sen; bisen0102@gmail.com

Received 18 April 2015; Accepted 18 April 2015

Copyright © 2015 An-Ya Lo et al. This is an open access article distributed under the Creative Commons Attribution License, which permits unrestricted use, distribution, and reproduction in any medium, provided the original work is properly cited.

With climate change and energy scarcity, the term “sustainability” has become the major challenge of the 21st century. Researches on clean and renewable energy are vital to break through this problem. Besides, any manners that help to reduce energy and resource consumption, enhance energy efficiency, and minimize the use and generation of hazardous substances are considered “sustainable” as well. Nano- and biorelated technologies have recently received immense attention for their applications on sustainable development. Therefore, there are many research efforts required to be addressed on the potential improvement of materials optical properties, noble metal nanoparticle preparation and properties, and biosynthesis, especially for organic and biocompatible ones, to achieve the upcoming challenges in the advanced applications. This special issue contains six papers; most of them involve both bio- and nanoengineering and technologies.

The paper “Biocomposite of Cassava Starch Reinforced with Cellulose Pulp Fibers Modified with Deposition of Silica (SiO₂) Nanoparticles” authored by J. Raabe et al. studies the effect of SiO₂ nanoparticle modification on the thermal stability, mechanical property, and hygroscopicity of cellulose fibers and their composites with starch. Results show improved tensile strength and reduced moisture absorption in the aforementioned reinforced starch, demonstrating the potential of such biodegradable material as replacement for conventionally used synthetic polymers.

The study titled “Organic Systems and Their Photorefractive Properties under the Nano- and Biostructuring:

Scientific View and Sustainable Development” demonstrates a potential impact of using organic systems such as DNA for modifying photorefractive properties of optoelectronic and biomedical application. The improvement of the photorefractiveness of the organic structures has been achieved by using nano- and biostructuring process, resulting in the changes of laser-induced refractive index and the rotation of the plane of polarization of light based on the model polyimide (PI) photosensitive donor-acceptor matrix and the nematic liquid crystal (NLC) compounds.

In the paper “Sustainable Nanopozzolan Modified Cement (NPMC): Characterizations and Morphology of Calcium Silicate Hydrate (C-S-H) during Hydration,” N. M. Sutan et al. have investigated the microstructural differences between two types of cement replacements as nanopozzolan modified cement (NPMC) and estimated the relationship between the pozzolanic reactivity and their physical/mechanical properties. It is found that the optimum dosage for MS and NS as the replacement in cement paste is 10% and 5%, respectively, which is due to the presence of the highest intensity in C-S-H. At this condition, the mechanical properties of NPMC in terms of compressive strength were improved by 67.8%. The synergies between MS and NS were well characterized by the XRD, FTIR, EDS spectroscopy analysis, and SEM morphology results that showed evidence of MS-NS interaction with the evidence of decreasing CH and increasing C-S-H.

The paper, titled “Biosynthesis of Anisotropic Silver Nanoparticles by *Bhargavaea indica* and Their Synergistic

Effect with Antibiotics against Pathogenic Microorganisms” authored by P. Singh et al., investigated the possibility to synthesize silver nanoparticles with various shapes by bacterial strain DC1. Without any extra reducing and capping agent, the strain *Bhargavaea indica* DC1 provides a rapid, ecofriendly, and economical route for the mass production of Ag-NPs. They indicate that the proposed method has also the potential to endow Ag-NPs with antimicrobial activity and also enhance the antimicrobial activity of antibiotics against pathogenic microorganisms, such as *Vibrio parahaemolyticus*, *Salmonella enterica*, *Staphylococcus aureus*, *Bacillus anthracis*, *Bacillus cereus*, *Escherichia coli*, and *Candida albicans*.

In the article entitled “Study of the Plasmon Energy Transfer Processes in Dye Sensitized Solar Cells” authors successfully demonstrated plasmonic enhancement of dye sensitized solar cells with up to 45% improvement in the cell power conversion efficiency by simply integrating a layer of island-like plasmonic gold nanoparticles with an N719/TiO₂ DSSC. Moreover, the further plasmonic energy transfer mechanism is also investigated and discussed in plasmonic DSSC system; this significant outcome would potentially benefit on achieving high solar energy conversion efficiency in DSSC system.

L. P. Lukhele et al. report the acute toxicity of double-walled carbon nanotubes (DWCNTs) to three aquatic organisms (algae, macroinvertebrate, and fish) of different trophic levels. The study of the effect of carbon nanotubes (CNTs) on the water bodies after consumption could indicate the long-term influence of the CNTs and their fate in the environment. The authors show different LC₅₀/EC₅₀ of DWCNTs for the three organisms, and humic acid and ionic strength of water were found to affect the toxicity levels. The acute toxicity of DWCNTs was dependent on their aggregation state in the aquatic system. Humic acid reduced the hydrodynamic size of the DWCNTs, whereas cations increased the size, thereby lowering the probability of interaction of DWCNTs with organisms.

Acknowledgments

The guest editors wish to thank all the authors for their valuable contribution to the special issue. We also express our sincere gratitude to all expert reviewers for their valuable time and effort to bring out and maintain the quality of the special issue.

An-Ya Lo
Chuan Wang
Wei Hsuan Hung
Anmin Zheng
Biswarup Sen

Research Article

Biocomposite of Cassava Starch Reinforced with Cellulose Pulp Fibers Modified with Deposition of Silica (SiO₂) Nanoparticles

Joabel Raabe,¹ Alessandra de Souza Fonseca,¹ Lina Bufalino,¹
Caue Ribeiro,² Maria Alice Martins,² José Manoel Marconcini,²
Lourival M. Mendes,¹ and Gustavo Henrique Denzin Tonoli¹

¹Department of Forest Science (DCF), Universidade Federal de Lavras, P.O. Box 3037, 37200-000 Lavras, MG, Brazil

²Laboratorio Nacional de Nanotecnologia para o Agronegocio (LNNA), Embrapa Instrumentacao, P.O. Box 741, 13560-970 Sao Carlos, SP, Brazil

Correspondence should be addressed to Gustavo Henrique Denzin Tonoli; gustavotonoli@yahoo.com.br

Received 30 October 2014; Revised 27 January 2015; Accepted 29 January 2015

Academic Editor: Chuan Wang

Copyright © 2015 Joabel Raabe et al. This is an open access article distributed under the Creative Commons Attribution License, which permits unrestricted use, distribution, and reproduction in any medium, provided the original work is properly cited.

Eucalyptus pulp cellulose fibers were modified by the sol-gel process for SiO₂ superficial deposition and used as reinforcement of thermoplastic starch (TPS). Cassava starch, glycerol, and water were added at the proportion of 60/26/14, respectively. For composites, 5% and 10% (by weight) of modified and unmodified pulp fibers were added before extrusion. The matrix and composites were submitted to thermal stability, tensile strength, moisture adsorption, and SEM analysis. Micrographs of the modified fibers revealed the presence of SiO₂ nanoparticles on fiber surface. The addition of modified fibers improved tensile strength in 183% in relation to matrix, while moisture adsorption decreased 8.3%. Such improvements were even more effective with unmodified fibers addition. This result was mainly attributed to poor interaction between modified fibers and TPS matrix detected by SEM analysis.

1. Introduction

Plant fibers have been studied as reinforcement in polymeric matrix in order to improve their physical and mechanical properties, as established practice for development of environmentally friendly products [1–8].

Starch is a promising material due to its high availability, renewable and biodegradable (even after being converted into a thermoplastic) character. Besides, this natural polymer presents interesting properties and characteristics for processing, being an attractive alternative to replace the synthetic polymers in applications that do not require long periods of use [9, 10]. Beyond many advantages, it should be noticed that there are some challenges to be addressed concerning thermoplastic starch competitiveness to partially replace conventional materials, such as lower mechanical strength and elasticity, high permeability to gases, as well as high hygroscopicity, and significant lower mechanical properties after water uptake [11].

Some strategies have been tested in order to minimize the high hygroscopicity of the cellulose fibers and to improve

the chemical compatibility between cellulose fibers and various polymeric matrices [12–14]. Modifications of fiber surface and structural properties are mainly based on the reactivity of the cellulose hydroxyls [13–16].

Hybrid organic-inorganic material was obtained in our previous work by deposition of SiO₂ nanoparticles on cellulose fiber surface [17]. Such modification with nanoparticles decreased the moisture adsorption of the fibers by reducing the amount of free hydroxyl groups, as reported elsewhere [18, 19]. Therefore, the aim of this study was to evaluate the feasibility of applying cellulose pulp fibers modified with silica (SiO₂) nanoparticles in thermoplastic starch (TPS). The thermal stability, tensile strength, and moisture adsorption of the composites were investigated.

2. Materials and Methods

2.1. Materials. *Eucalyptus* cellulose fibers were obtained from kraft pulping process, with average length of 0.81 ± 0.01 mm and average width of 15.9 ± 0.3 μ m. Chemical composition of

the fibers was cellulose (86.3%), hemicelluloses (12.9%), and ashes and extractives (0.8%).

The inorganic precursor tetraethyl orthosilicate ($C_8H_{20}O_4Si$ -TEOS, 98%) for SiO_2 synthesis was provided by Sigma Aldrich. Ammonium hydroxide (NH_4OH -30% v.v⁻¹) was the catalyst. Ethanol (CH_3CH_2OH -Neon 95%) was the solvent. Potassium sulfate (K_2SO_4 -Vetec P.A.) was used for humidity control in the moisture adsorption test.

Cassava starch, composed of 85.5% amylopectin and 14.5% amylose (purchased from SM Ltda., Brazil); bidistilled glycerin plasticizer (Synth 98%); stearic acid ($C_{18}H_{36}O_2$ -Synth 98%); and anhydrous citric acid ($C_6H_8O_7$ -Chenco 98%) were used for preparation of the TPS extruded composites.

2.2. Methods

2.2.1. Modification of the Cellulose Fiber Surface. Unmodified cellulose fibers were kept in deionized water under mechanical stirring for 24 h in order to achieve total disintegration of cellulose sheets and proper fiber dispersion. Water to fiber consistency was 100 mL.g⁻¹.

Fiber modification was carried out by sol-gel process based on previous studies [17–19]. A mass of 45 g of cellulose fibers was immersed in a solution composed of 3.6 L of ethanol, 405 mL of deionized water, and 67.5 mL of ammonium hydroxide. Constant and moderate mechanical stirring (300 rpm) was kept for 2 h, after which 8.4 g of TEOS per g of cellulose fiber solution was slowly added drop by drop and a solution with fiber consistency of 100 mL.g⁻¹ was prepared.

After addition of TEOS, the reaction was kept under stirring for 18 h, under controlled environmental conditions (temperature of $20 \pm 2^\circ C$ and relative humidity of $65 \pm 5\%$). The modified fibers were thoroughly washed with deionized water, filtered, and subsequently dried at $60 \pm 2^\circ C$ [17].

2.2.2. Processing of the Thermoplastic Starch (TPS) and Composites. The thermoplastic starch (TPS) was obtained from the physical mixture of cassava starch, glycerol, and deionized water in the mass proportions of 60/24/16, respectively. The contents of 1% (by weight) of stearic acid and 1% (by weight) of citric acid were used as antioxidants for extrusion, according to previous studies [12, 20, 21]. Modified (MF-5% and MF-10%) and unmodified (NMF-5% and NMF-10%) fibers were added to the TPS at 5% and 10% loads (based on total mass of the composite). The composites were processed in an 18 mm corotating twin-screw with L/D ratio of 40 (Laboratory Extruder ZSK 18 MEGAlab, Coperion, Germany) equipped with seven heating zones and a ribbon die. The screw rotation speed was 250 rpm and the temperature profile was set between 110 and 140°C in the seven heating zones. Extruded ribbons were pelletized and further processed in a single-screw extruder (AX Plásticos Ltda., Brazil) operating at 100 rpm under 130°C, 130°C, and 150°C heating zones for production of strips of 3 mm thickness. Tensile test samples were cut from these strips in a hydraulic press preheated for 2 min at 60°C, with the aid of a metal mold with the dimensions described in ASTM 638-10 [22].

2.2.3. Scanning Electron Microscopy (SEM). Morphological characteristics of the fibers and the fractured surface of the composites were evaluated by SEM micrographs in a JEOL JSM-6510 microscope, with a tungsten filament and operating at 15 kV. An energy dispersive spectroscopy (EDS) system (model JEOL 6742A-Ultradry Silicon Drift) with an active area of 10 mm² and 132 eV resolution was used to detect and semiquantify SiO_2 particles at the fiber surface. Average percentage of Si (% by mass) was obtained after five scans per sample in a 1 μm^2 area. The fiber samples were bonded over a carbon tape on the metallic stubs and carbon coated (for EDS measurements) and gold coated (for scanning electron microscopy (SEM) observations). Cryogenically fractured surfaces of the cross section of the test samples were prepared for microstructural evaluation by gold coating of the composites.

2.2.4. Thermogravimetric Analysis (TGA). Starch (in powder), plain TPS, and composites were subject to thermogravimetric analysis (TGA) in a TA Instruments analyzer (model Q500) as proposed in Tonoli et al. [23]. The 7–10 mg samples were heated in a Pt crucible from 25 to 600°C in a dynamic atmosphere of synthetic air (80% N₂ and 20% O₂) flowing at 60 mL.min⁻¹ and heating rate of 10°C.min⁻¹. The critical weight loss temperatures (*T*-onset), the temperature at which samples lost between 70 and 80% of mass (*T*-shoulder), and the temperature at which the final mass became stable (*T*-endset) were obtained from the TG curves.

2.2.5. Mechanical Properties (Tensile Test). Tensile tests of the TPS and composites were carried out according to ASTM D 638-10 [22], using universal testing machine (EMIC DL3000) with a 500 Kgf load cell. The test speed was set to 50 mm.min⁻¹ and the minimum of five replicates per composite material were tested in order to determine the Young modulus (*E*), ultimate tensile strength (σ_r), and deformation at break (ϵ_r) of the materials.

2.2.6. Moisture Adsorption Analysis. Five 1.0 cm × 4.0 cm × 0.2 cm samples of each formulation were predried for 48 h at 60°C, weighed, and placed in hermetically closed containers with $97 \pm 2\%$ of relative humidity (RH) and $20 \pm 2^\circ C$, using a saturated potassium sulfate solution, as prescribed by the ASTM E104 [24] standard. The moisture adsorbed by the samples by time was determined by weighing (0.0001 g precision) them at successive intervals until they reached constant weight. The amount of moisture adsorbed (MA) by the samples was calculated as follows:

$$MA (\%) = \left[\frac{(M_t - M_0)}{M_0} \right] \times 100, \quad (1)$$

where M_0 and M_t are the initial mass of the sample (prior to exposure to moisture) and the sample mass after *t* hours of exposure to moisture ($97 \pm 2\%$ RH), respectively. Each data point represents an average of five samples.

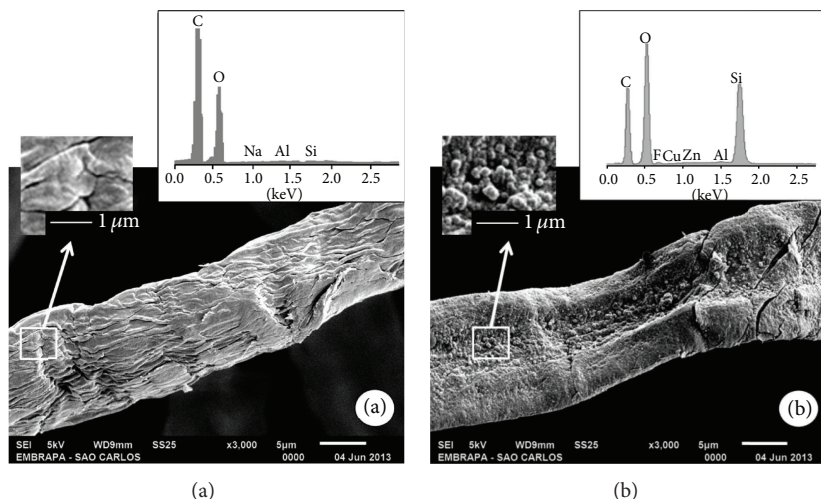


FIGURE 1: SEM micrographs and EDS measurements (detail) of (a) unmodified and (b) modified cellulose fibers.

3. Results and Discussion

3.1. Fiber Modification. Figure 1 shows SEM images and EDS analysis of unmodified and modified cellulose pulp fibers. Cellulose pulp fibers before modification (unmodified) showed a smooth and uniform surface (Figure 1(a)), with some apparent imperfections (detail) caused by the subsequent stages of drying during the pulping and bleaching process. The content of silicon (Si) in unmodified fibers (1.4%) was clearly lower compared with the modified fiber (17.7%), as seen in the peaks of EDS analysis (Figures 1(a) and 1(b), resp.). SEM and EDS of the modified fibers (Figure 1(b)) show that the SiO_2 nanoparticles (detail) were deposited on the surface of the cellulose fibers, as observed by the increasing of the silicon (Si) peak in the EDS measurement, confirming that the modification procedure was successful.

The deposition of SiO_2 nanoparticles caused the coating of imperfections found in unmodified cellulose fibers. SiO_2 deposition is achieved by the hydrolysis of the TEOS precursor and subsequent condensation of the resultant hydroxyl groups on the surface of the fibers [17, 25]. Although no information was available from EDS measurements about the thickness or degree of SiO_2 covering, the results strongly suggest that a hybrid cellulose + SiO_2 composite was formed since Si peak was remarkably intense in relation to C and O peaks [26]. Pinto et al. [18] succeeded in cellulose fibers modification by using TEOS precursor. The authors reported fibers coated with a homogeneous layer of SiO_2 nanoparticles, which provided a remarkable reduction in water uptake. Ashori et al. [19] conducted a similar work with bacterial cellulose and observed strong chemical interactions between cellulose and silica phases in addition to improvement of the composite mechanical strength. The above-mentioned studies clearly show the effectiveness of using TEOS precursor in the modification of cellulose fibers.

The moisture adsorption pattern of the unmodified and modified cellulose fibers exposed to $97 \pm 2\%$ RH is shown in Figure 2. After mass stabilization was reached, the unmodified fibers presented higher moisture adsorption ($25.0 \pm 0.5\%$)

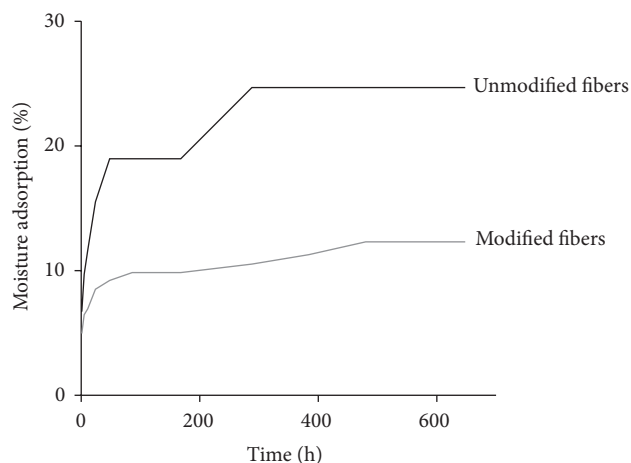


FIGURE 2: Moisture adsorption of unmodified and modified fibers.

than modified fibers ($12.3 \pm 1.0\%$). This result is attributed to the decrease of free hydroxyls, caused by deposition of SiO_2 nanoparticles on the surface of the fibers, reducing their hygroscopicity.

3.2. Thermal Analysis of the Composites. The thermal behaviors (TG and DTG) of the starch, TPS, and composites reinforced with modified fibers (MF) and unmodified (NMF) fibers are shown in Figure 3. For starch, there were three stages of mass loss clearly defined in TG curves. Steps two and three as much as main peaks are readily observed in DTG curves. The first occurred between 30°C and 150°C , corresponding to release of water and volatile. The second was observed between 250 and 350°C with most prominent degradation at 310°C related to starch decomposition [27]. Some gases such as CO_2 , CO , H_2O , and other small volatile are released during this stage along with carbonaceous residue formation [28, 29]. The last stage took place between 415 and 540°C and corresponds to decomposition of

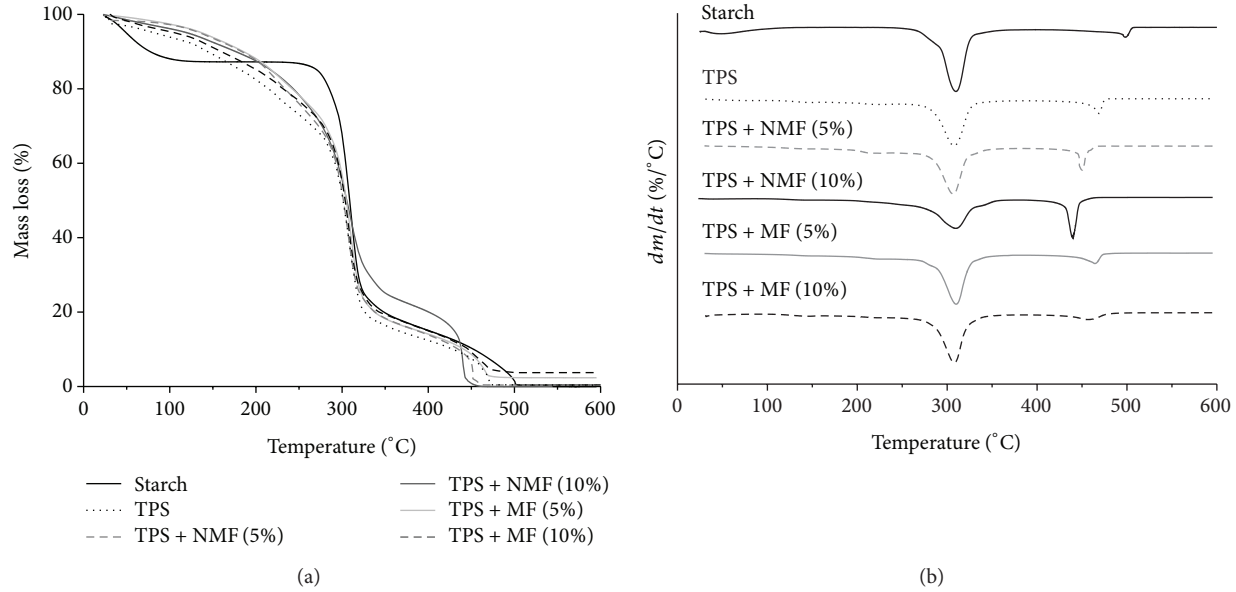


FIGURE 3: (a) TG and (b) DTG of the starch (powder), TPS, and composites reinforced with unmodified (NMF) and modified (MF) cellulose fibers. Analysis ran under synthetic air atmosphere.

TABLE 1: Thermal properties (obtained by TG and DTG analyses) of the starch, TPS, and composites.

| Sample | T -onset (°C) | DTG peak (°C) | T -shoulder (°C) | T -endset (°C) | Residue at 600°C (%) |
|-----------------|-----------------|---------------|--------------------|------------------|----------------------|
| Starch | 300 ± 7 | 310 ± 3 | 321 ± 6 | 502 ± 2 | 0.4 ± 0.3 |
| TPS | 291 ± 11 | 308 ± 1 | 321 ± 10 | 471 ± 4 | 0.4 ± 0.2 |
| TPS + NMF (5%) | 290 ± 3 | 307 ± 3 | 320 ± 7 | 459 ± 2 | 0.4 ± 0.4 |
| TPS + NMF (10%) | 291 ± 3 | 309 ± 2 | 325 ± 16 | 443 ± 2 | 0.0 ± 0.5 |
| TPS + MF (5%) | 293 ± 4 | 310 ± 3 | 322 ± 6 | 475 ± 7 | 2.4 ± 2.2 |
| TPS + MF (10%) | 292 ± 6 | 308 ± 3 | 320 ± 10 | 471 ± 2 | 3.7 ± 1.8 |

the previously formed residue since an oxidative atmosphere was used [27].

TPS exhibited a steady loss of weight from room temperature to near 250°C. This behavior is related to both the release of water adsorbed by the plastics during their acclimatization and combustion/volatilization of glycerol. This phenomenon hinders distinction between the first and second stage of TPS degradation and causes stronger mass loss ratio in the first stage in comparison to starch [30].

From the TG curve (Figure 3(a)), the initial (T -onset) and end (T -endset) degradation temperatures of starch, TPS, and composite formulations were determined (Table 1). TPS and composites showed a slight anticipation of the main weight loss event ($\sim 290^\circ\text{C}$) compared to starch granules ($\sim 300^\circ\text{C}$). This difference can be explained based on starch polymer chain fragmentation, due to TPS processing, by which organizational structure of the starch was partially destroyed causing the mobility of polymer chains to increase [31–33]. Fiber addition (both NMF and MF) slightly decreased weight loss ratio for temperatures below 250°C. NMF and MF levels were not greatly affected and the initial degradation temperature (Table 1, view T -onset) was similar for both TPS and composites. It is well known that unbleached fiber addition improves the thermal stability of the starch matrix

when good adhesion between the parts is achieved [34]. Such behavior was not observed in this work.

Figure 3(b) shows the maximum DTG peak between 250 and 350°C, which occurs around 310°C for all materials (Table 1). In addition, it can be noticed that starch exhibited the highest mass loss peak. The last thermal event after 400°C shows the decomposition of the carbonaceous residue that ranged from 498°C for starch to 467°C for TPS. Also, the increase in cellulose pulp load from 5% to 10% led to the decrease in temperature of maximum mass loss (from 450°C to 440°C for unmodified fibers and from 464°C to 456°C for modified fibers). This result suggests that cellulose and Si have a catalytic activity on the thermal decomposition of the starch carbonaceous product [27]. The residue contents remarkably raised with fiber load increase from 5 to 10%, as much as from unmodified to SiO₂ modified fibers.

3.3. Mechanical Performance of the Composites. The stress to strain curves for tensile test of TPS and composites is shown in Figure 4. All curves showed a linear region at low stress application, where the stress was proportional to the strain (elastic behavior), followed by plastic behavior and restriction, where the stress showed a constant pattern until failure.

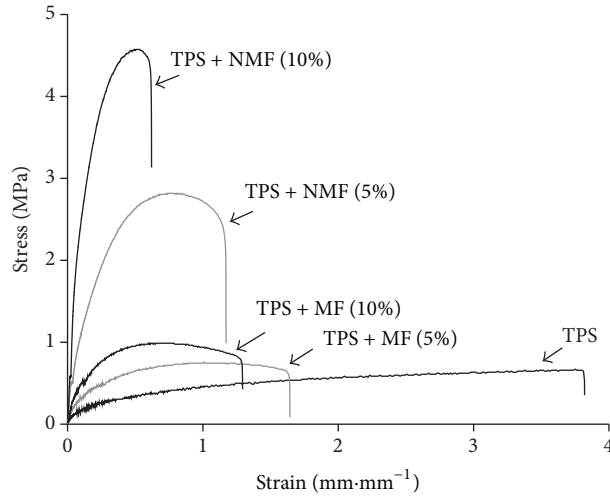


FIGURE 4: Stress to strain curves for tensile test of the TPS and composites reinforced with unmodified (NMF) and modified (MF) fibers.

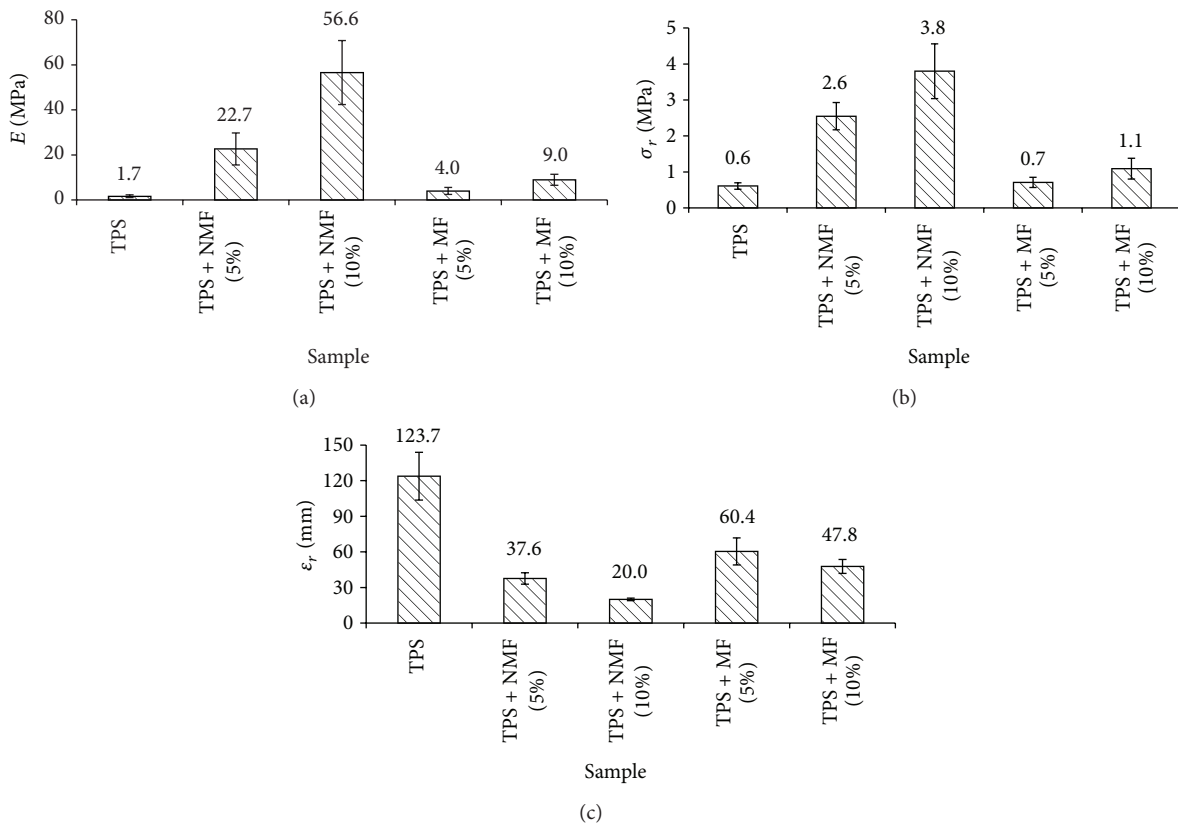


FIGURE 5: (a) Young modulus (E), (b) tensile strength (σ_r), and (c) strain at break (ϵ_r) of TPS and composites reinforced with unmodified (NMF) and modified (MF) fibers.

Inclusion of cellulose fibers and increase in fiber load led to an increase of Young modulus (E) and tensile strength (σ_r) of the composites in comparison to the TPS. Nevertheless, the strain at break (ϵ_r) decreased more than 50% with fiber addition (Figure 5).

Addition of 5% of unmodified fibers to TPS increased in 1335% and 433% Young modulus and tensile strength,

respectively. Inclusion of 10% of unmodified fibers to TPS increased in 3329% and 633% Young modulus and tensile strength, respectively. The improvement of the mechanical properties (tensile) with inclusion of different plant fibers and nanofibers in TPS composites was widely reported in literature [10, 35, 36]. For composites with modified fibers, the inclusion of 5% of fibers increased in 235% and 116%

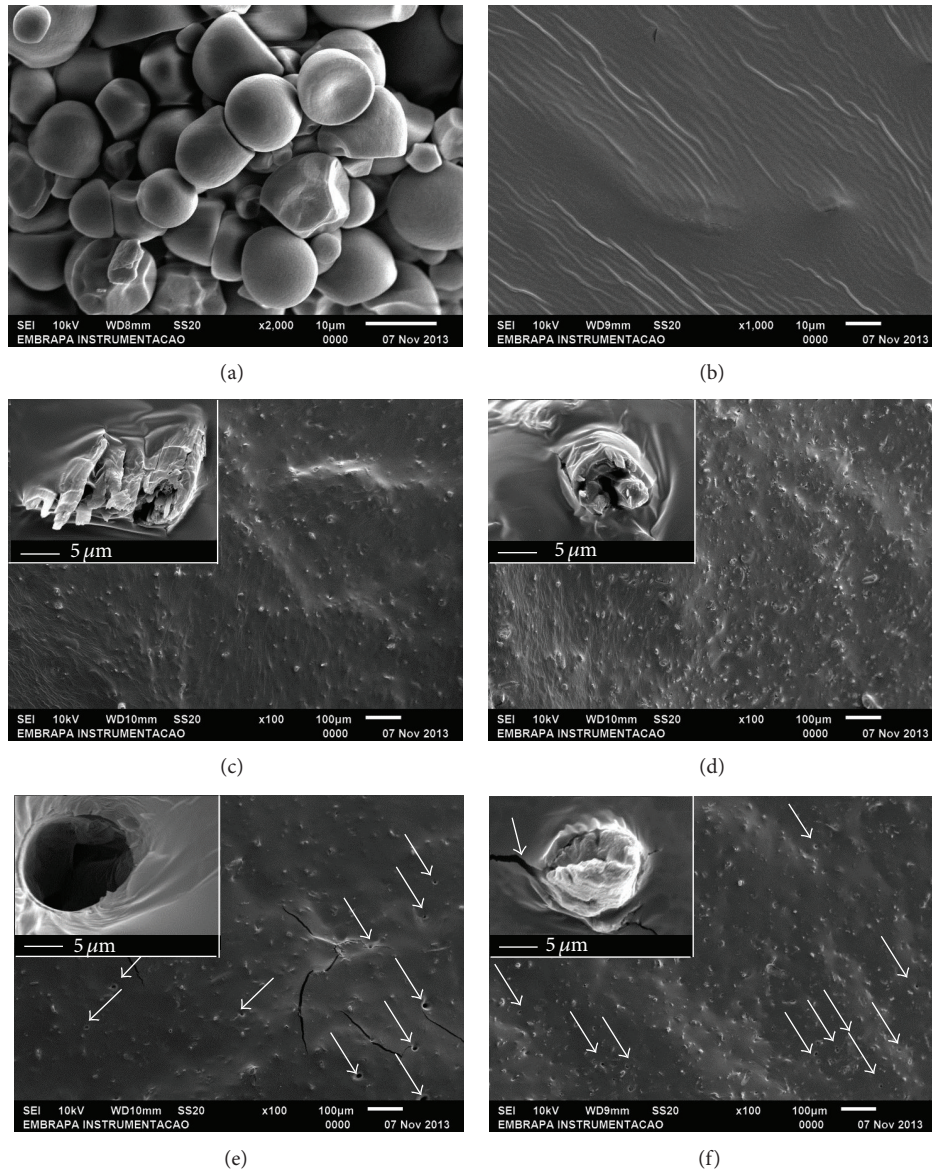


FIGURE 6: SEM micrographs of (a) raw starch; fractured surface of the (b) TPS; (c, d) composites reinforced with 5% and 10% of unmodified fibers (NMF), respectively; and (e, f) composites reinforced with 5% and 10% of modified fibers (MF). Arrows indicate holes in the composite after rupture.

the Young modulus and the tensile strength, respectively, while for 10% of fibers the increase was of 529% in the Young modulus and 183% in the tensile strength. The lower mechanical performance of composites reinforced with MF, in relation to NMF (unmodified) fibers, can be attributed to the poor adhesion of these fibers to the TPS matrix. SiO₂ nanoparticles deposition on fiber surface drastically reduces the free hydroxyl groups [25], making them into hydrophobic. Fewer free hydroxyl groups on fiber surface hinder their interaction with the matrix, which strongly affects mechanical performance [13, 14]. Effective wetting, uniform dispersion of all the components in the matrix, and strong interfacial adhesion are required to obtain high strength composites [37].

3.4. Microstructural Analyses of the Composites. Scanning electron microscopy (SEM) was used to observe the interaction and dispersion of the cellulose fibers in the TPS matrix. Micrographs of the starch powder and fractured surface of TPS and composites are depicted in Figure 6. The size of the starch granules was about 8 to 15 μm (Figure 6(a)) and their complete breakage due to extrusion can be observed in the TPS and composites.

The fractured surface of the TPS samples (Figure 6(b)) shows homogeneous and compact structure, besides no visible flaws and voids. TPS composites reinforced with unmodified fibers (5% and 10% of NMF, Figures 6(c) and 6(d), resp.) show good fiber dispersion in the TPS matrix, without evident agglutinations. Strong interaction between

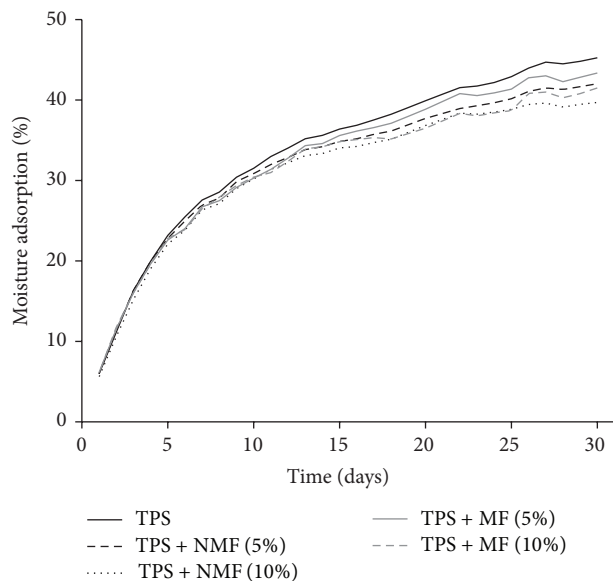


FIGURE 7: Moisture adsorption of the TPS and composites reinforced with unmodified (NMF) and modified (MF) fibers.

matrix and fibers was also observed (Figures 6(c) and 6(d) and details). SEM images evidence higher concentration of fibers in composites made with 10% of NMF (Figure 6(d)) in comparison to those with 5% NMF addition (Figure 6(c)). The same may be observed for composites with MF (Figures 6(e) and 6(f)). Fiber agglutinations are not desired because they limit the stresses transference from matrix to the fiber [38] and hence decrease mechanical strength of the composites. For composites reinforced with modified fibers it can be observed that fibers were pulled out from the TPS with fracture, leaving voids in the matrix (arrows in Figures 6(e) and 6(f)). Certainly this is a result of ineffective interaction between composite phases (details in Figures 6(e) and 6(f)) as stated elsewhere [39].

3.5. Moisture Adsorption of Composites. The TPS adsorbs moisture due to its hydrophilic nature [40], which directly affects applications of derivate products. The moisture adsorption curve of the materials during 30 days of exposure to $97 \pm 2\%$ RH ($20 \pm 2^\circ\text{C}$) is shown in Figure 7. The moisture uptake in the TPS and composites increased linearly up to five days, followed by a slower adsorption ratio.

The addition of cellulose fibers contributed to decreasing of moisture adsorption of TPS (Figure 7), similarly to results from other works [41–43]. Remarkable differences in water resistance among the evaluated materials become evident after the fifth day of exposure to humid environment. After 30 days, it was observed a reduction of 12.3% in moisture adsorption for composites reinforced with 10% NMF, in comparison to TPS. The composites reinforced with 5% and 10% of MF presented 4.2% and 8.3% decrease in water adsorption, respectively, in relation to TPS.

Lower enhancement of moisture adsorption found for composites reinforced with MF is possibly due to

formation of microcracks at the interface between phases (arrow in the detail of Figure 6(f)), which may favor moisture accumulation. Interactions by hydrogen bonding between starch molecules and cellulose fibers for both modified and unmodified fibers make composites more stable to humid conditions in relation to TPS [44].

Main results found in our work show that deposition of SiO_2 nanoparticles hindered the interfacial interaction between the cellulosic fibers and the TPS matrix. Future investigations with nonpolar matrices are recommended to advance the development of composites reinforced with the hybrid SiO_2 -cellulose materials proposed in this work, since a remarkable decrease in hydrophilic nature of cellulose fibers was achieved.

4. Conclusions

The main proposition of this work was to develop a new high strength composite made from TPS and *Eucalyptus* cellulose pulp fibers modified by SiO_2 nanoparticles superficial deposition. Improvements include the moisture adsorption decrease and higher thermal stability of composites in relation to TPS. Higher cellulose fiber load (10%) provided improvements in mechanical and moisture strength of the composites. Poorer interaction between composite phases was detected when modified fibers (MF) were used; hence higher strength was found for formulations with unmodified fibers. The modification of the fibers proposed in this work was successful, since a distinct surface characteristic of the cellulose pulp fibers was observed. Such modification is very promising for ongoing investigations towards development and improvement of renewable composites.

Conflict of Interests

The authors declare that there is no conflict of interests regarding the publication of this paper.

Acknowledgments

Financial support for this research project was provided by the Conselho Nacional de Desenvolvimento Científico e Tecnológico (CNPq), Fundação de Amparo à Pesquisa do Estado de São Paulo (Fapesp), Fundação de Amparo à Pesquisa do Estado de Minas Gerais (Fapemig), Coordenação de Aperfeiçoamento de Pessoa de Nível Superior (Capes, Edital Capes-Embrapa), and Empresa Brasileira de Pesquisa Agropecuária (Embrapa), in Brazil. Thanks also go to Rede Brasileira de Compósitos e Nanocompósitos Ligno-celulósicos (Religar).

References

- [1] C. A. Hemais, "Polímeros e a indústria automobilística," *Polímeros: ciência e tecnologia*, vol. 13, no. 2, pp. 107–114, 2003.
- [2] S. V. Joshi, L. T. Drzal, A. K. Mohanty, and S. Arora, "Are natural fiber composites environmentally superior to glass fiber reinforced composites?" *Composites Part A: Applied Science and Manufacturing*, vol. 35, no. 3, pp. 371–376, 2004.

- [3] F. N. P. Nicolai, V. R. Botaro, and V. F. C. Lins, "Effect of saline degradation on the mechanical properties of vinyl ester matrix composites reinforced with glass and natural fibers," *Journal of Applied Polymer Science*, vol. 108, no. 4, pp. 2494–2502, 2008.
- [4] A. Alemdar and M. Sain, "Biocomposites from wheat straw nanofibers: morphology, thermal and mechanical properties," *Composites Science and Technology*, vol. 68, no. 2, pp. 557–565, 2008.
- [5] A. Ashori, "Wood-plastic composites as promising green-composites for automotive industries!," *Bioresource Technology*, vol. 99, no. 11, pp. 4661–4667, 2008.
- [6] Y. Xue, Y. Du, S. Elder, K. Wang, and J. Zhang, "Temperature and loading rate effects on tensile properties of kenaf bast fiber bundles and composites," *Composites Part B: Engineering*, vol. 40, no. 3, pp. 189–196, 2009.
- [7] A. S. Fonseca, F. A. Mori, G. H. D. Tonoli, H. Savastano, D. L. Ferrari, and I. P. A. Miranda, "Properties of an Amazonian vegetable fiber as a potential reinforcing material," *Industrial Crops and Products*, vol. 47, pp. 43–50, 2013.
- [8] A. R. Kakroodi, S. Cheng, M. Sain, and A. Asiri, "Mechanical, thermal, and morphological properties of nanocomposites based on polyvinyl alcohol and cellulose nanofiber from *Aloe vera* rind," *Journal of Nanomaterials*, vol. 2014, Article ID 903498, 7 pages, 2014.
- [9] R. Belhassen, F. Vilaseca, P. Mutjé, and S. Boufi, "Thermoplasticized starch modified by reactive blending with epoxidized soybean oil," *Industrial Crops and Products*, vol. 53, pp. 261–267, 2014.
- [10] M. G. Lomelí-Ramírez, S. G. Kestur, R. Manríquez-González, S. Iwakiri, G. B. De Muniz, and T. S. Flores-Sahagun, "Biocomposites of cassava starch-green coconut fiber: part II—structure and properties," *Carbohydrate Polymers*, vol. 102, no. 1, pp. 576–583, 2014.
- [11] M. A. Huneault and H. Li, "Morphology and properties of compatibilized polylactide/thermoplastic starch blends," *Polymer*, vol. 48, no. 1, pp. 270–280, 2007.
- [12] A. de Campos, G. H. D. Tonoli, J. M. Marconcini et al., "TPS/PCL composite reinforced with treated sisal fibers: property, biodegradation and water-absorption," *Journal of Polymers and the Environment*, vol. 21, no. 1, pp. 1–7, 2013.
- [13] O. Faruk, A. K. Bledzki, H.-P. Fink, and M. Sain, "Biocomposites reinforced with natural fibers: 2000–2010," *Progress in Polymer Science*, vol. 37, no. 11, pp. 1552–1596, 2012.
- [14] M. M. Kabir, H. Wang, K. T. Lau, and F. Cardona, "Chemical treatments on plant-based natural fibre reinforced polymer composites: an overview," *Composites Part B: Engineering*, vol. 43, no. 7, pp. 2883–2892, 2012.
- [15] H. Liu, F. Xie, L. Yu, L. Chen, and L. Li, "Thermal processing of starch-based polymers," *Progress in Polymer Science*, vol. 34, no. 12, pp. 1348–1368, 2009.
- [16] P. A. Skreekumar, J. Kuruvilla, G. Unnikrishnan, and T. Sabu, "Surface-modified sisal fiber-reinforced eco-friendly composites: mechanical, thermal, and diffusion studies," *Polymer Composites*, vol. 32, no. 1, pp. 131–138, 2011.
- [17] J. Raabe, A. S. Fonseca, L. Bufalino et al., "Evaluation of reaction factors for deposition of silica (SiO₂) nanoparticles on cellulose fibers," *Carbohydrate Polymers*, vol. 114, pp. 424–431, 2014.
- [18] R. J. B. Pinto, P. A. A. P. Marques, A. M. Barros-Timmons, T. Trindade, and C. P. Neto, "Novel SiO₂/cellulose nanocomposites obtained by in situ synthesis and via polyelectrolytes assembly," *Composites Science and Technology*, vol. 68, no. 3–4, pp. 1088–1093, 2008.
- [19] A. Ashori, S. Sheykhnazari, T. Tabarsa, A. Shakeri, and M. Golalipour, "Bacterial cellulose/silica nanocomposites: preparation and characterization," *Carbohydrate Polymers*, vol. 90, no. 1, pp. 413–418, 2012.
- [20] A. Campos, K. B. R. Teodoro, J. M. Marconcini, L. H. C. Mattoso, and S. M. Martins-Franchetti, "Efeito do tratamento das fibras nas propriedades do biocompósito de amido termoplástico/policaprolactona/sisal," *Polímeros*, vol. 21, no. 3, pp. 217–222, 2011.
- [21] V. B. Carmona, A. De Campos, J. M. Marconcini, and L. H. C. Mattoso, "Kinetics of thermal degradation applied to biocomposites with TPS, PCL and sisal fibers by non-isothermal procedures," *Journal of Thermal Analysis and Calorimetry*, vol. 115, no. 1, pp. 153–160, 2014.
- [22] ASTM D638-10, "Standard test for tensile properties of plastics," Annual book of ASTM standards, 2010.
- [23] G. H. D. Tonoli, E. M. Teixeira, A. C. Corrêa et al., "Cellulose micro/nanofibres from *Eucalyptus kraft* pulp: preparation and properties," *Carbohydrate Polymers*, vol. 89, no. 1, pp. 80–88, 2012.
- [24] ASTM E104-12, "Standard practice for maintaining constant humidity by means of aqueous solutions," Annual book of ASTM standards, 2012.
- [25] B. P. Tripathi and V. K. Shahi, "Organic-inorganic nanocomposite polymer electrolyte membranes for fuel cell applications," *Progress in Polymer Science*, vol. 36, no. 7, pp. 945–979, 2011.
- [26] G. H. D. Tonoli, U. P. Rodrigues Filho, H. Savastano Jr., J. Bras, M. N. Belgacem, and F. A. Rocco Lahr, "Cellulose modified fibres in cement based composites," *Composites Part A: Applied Science and Manufacturing*, vol. 40, no. 12, pp. 2046–2053, 2009.
- [27] F. K. V. Moreira, D. C. A. Pedro, G. M. Glenn, J. M. Marconcini, and L. H. C. Mattoso, "Brucite nanoplates reinforced starch bionanocomposites," *Carbohydrate Polymers*, vol. 92, no. 2, pp. 1743–1751, 2013.
- [28] C. T. Greenwood, "The thermal degradation of starch," *Advances in Carbohydrate Chemistry and Biochemistry*, vol. 22, pp. 483–515, 1967.
- [29] X. Zhang, J. Golding, and I. Burgar, "Thermal decomposition chemistry of starch studied by ¹³C high-resolution solid-state NMR spectroscopy," *Polymer*, vol. 43, no. 22, pp. 5791–5796, 2002.
- [30] J. K. Pandey and R. P. Singh, "Green nanocomposites from renewable resources: effect of plasticizer on the structure and material properties of clay-filled starch," *Starch*, vol. 57, no. 1, pp. 8–15, 2005.
- [31] P. Aggarwal, D. Dollimore, and K. Heon, "Comparative thermal analysis study of two biopolymers, starch and cellulose," *Journal of Thermal Analysis*, vol. 50, no. 1–2, pp. 7–17, 1997.
- [32] P. Aggarwal and D. Dollimore, "A thermal analysis investigation of partially hydrolyzed starch," *Thermochimica Acta*, vol. 319, no. 1–2, pp. 17–25, 1998.
- [33] A. Vasquez, V. P. Cyras, V. A. Alvarez, and J. I. Moran, "Starch/clay nano-biocomposites," in *Environmental Silicate Nano-Biocomposites*, L. Avérous and E. Pollet, Eds., chapter 11.14, pp. 287–321, Springer, London, UK, 1st edition, 2012.
- [34] T. Phattaraporn, S. Waranyou, A. Fazilah, and W. Thawien, "Characterization and properties of rice starch films reinforced with palm press fibers," *International Food Research Journal*, vol. 17, pp. 537–547, 2010.
- [35] M. Hietala, A. P. Mathew, and K. Oksman, "Bionanocomposites of thermoplastic starch and cellulose nanofibers manufactured

- using twin-screw extrusion,” *European Polymer Journal*, vol. 49, no. 4, pp. 950–956, 2013.
- [36] J. P. López, P. Mutjé, A. J. F. Carvalho, A. A. S. Curvelo, and J. Gironès, “Newspaper fiber-reinforced thermoplastic starch biocomposites obtained by melt processing: evaluation of the mechanical, thermal and water sorption properties,” *Industrial Crops and Products*, vol. 44, pp. 300–305, 2013.
- [37] C. S. Wu, F. S. Yen, and C. Y. Wang, “Polyester/natural fiber biocomposites: preparation, characterization, and biodegradability,” *Polymer Bulletin*, vol. 67, no. 8, pp. 1605–1619, 2011.
- [38] M. F. Rosa, B.-S. Chiou, E. S. Medeiros et al., “Biodegradable composites based on starch/EVOH/glycerol blends and coconut fibers,” *Journal of Applied Polymer Science*, vol. 111, no. 2, pp. 612–618, 2009.
- [39] C. A. Teacă, R. Bodîrlău, and I. Spiridon, “Effect of cellulose reinforcement on the properties of organic acid modified starch microparticles/plasticized starch bio-composite films,” *Carbohydrate Polymers*, vol. 93, no. 1, pp. 307–315, 2013.
- [40] D. Preechawong, M. Peesan, P. Supaphol, and R. Rujiravanit, “Characterization of starch/poly(ϵ -caprolactone) hybrid foams,” *Polymer Testing*, vol. 23, no. 6, pp. 651–657, 2004.
- [41] N. Soykeabkaew, N. Laosat, A. Ngaokla, N. Yodsuwan, and T. Tunkasiri, “Reinforcing potential of micro- and nano-sized fibers in the starch-based biocomposites,” *Composites Science and Technology*, vol. 72, no. 7, pp. 845–852, 2012.
- [42] V. A. Alvarez, R. A. Ruseckaite, and A. Vázquez, “Mechanical properties and water absorption behavior of composites made from a biodegradable matrix and alkaline-treated sisal fibers,” *Journal of Composite Materials*, vol. 37, no. 17, pp. 1575–1588, 2003.
- [43] V. A. Alvarez, R. A. Ruseckaite, and A. Vázquez, “Degradation of sisal fibre/Mater Bi-Y biocomposites buried in soil,” *Polymer Degradation and Stability*, vol. 91, no. 12, pp. 3156–3162, 2006.
- [44] Y. Lu, L. Weng, and X. Cao, “Biocomposites of plasticized starch reinforced with cellulose crystallites from cottonseed linter,” *Macromolecular Bioscience*, vol. 5, no. 11, pp. 1101–1107, 2005.

Research Article

Biosynthesis of Anisotropic Silver Nanoparticles by *Bhargavaea indica* and Their Synergistic Effect with Antibiotics against Pathogenic Microorganisms

Priyanka Singh,¹ Yeon Ju Kim,¹ Hina Singh,¹ Ramya Mathiyalagan,²
Chao Wang,¹ and Deok Chun Yang^{1,2}

¹Department of Oriental Medicinal Biotechnology, College of Life Sciences, Kyung Hee University, Republic of Korea

²Graduate School of Biotechnology and Ginseng Bank, College of Life Sciences, Kyung Hee University,
Yongin 446-701, Republic of Korea

Correspondence should be addressed to Yeon Ju Kim; yeonjukim@khu.ac.kr and Deok Chun Yang; dcyang@khu.ac.kr

Received 18 November 2014; Accepted 1 January 2015

Academic Editor: An-Ya Lo

Copyright © 2015 Priyanka Singh et al. This is an open access article distributed under the Creative Commons Attribution License, which permits unrestricted use, distribution, and reproduction in any medium, provided the original work is properly cited.

The strain *Bhargavaea indica* DC1 isolated from four-year-old *P. ginseng* rhizospheric soil was used to perform rapid and extracellular biosynthesis of anisotropic silver nanoparticles. The ultraviolet-visible (UV-vis) spectra of the reaction mixture containing silver nanoparticles showed a peak at 460 nm, corresponding to the surface plasmon absorbance of silver nanoparticles. Field-emission transmission electron microscopy (FE-TEM) structural characterization revealed the nanobar, pentagon, spherical, icosahedron, hexagonal, truncated triangle, and triangular nanoparticles, with the size range from 30 to 100 nm. The energy-dispersive X-ray (EDX) analysis and elemental mapping results also confirmed that the silver was the predominant component of isolated nanoparticles. The X-ray diffraction (XRD) results correspond to the purity of silver nanoparticles and dynamic light scattering (DLS) result indicated that the average diameter of particles was 111.6 nm. In addition, enhancement in antimicrobial activity of commercial antibiotics was observed against various pathogenic microorganisms such as *Vibrio parahaemolyticus*, *Salmonella enterica*, *Staphylococcus aureus*, *Bacillus anthracis*, *Bacillus cereus*, *Escherichia coli*, and *Candida albicans*.

1. Introduction

Nanomaterials have been studied intensively and have received considerable attention in various scientific fields due to unique properties including ultra-small size, high surface-area-to-mass ratio, and high reactivity [1]. Chemical and physical methods for the synthesis of metal nanoparticles are well known, but the methodologies are expensive and not environmentally friendly, thus limiting the applications of metal nanoparticles in biological and medical platforms [2]. To overcome the limitation of physicochemical methodologies, the simple, low-cost, and eco-friendly technologies are needed whereby these nanoparticles can be synthesized while avoiding the use of toxic chemicals and solvents. The green synthesis is a feasible alternative, and various biological

species have been well studied for this purpose, including bacteria, yeast, fungi, and plant extracts [2–6]. Such research has led to new product developments and applications of biological species in different fields [7].

Among the many metal nanoparticles, silver nanoparticles are one of the most studied and prominent nanoproducts. Silver nanoparticles are well known for their inhibitory and bactericidal effects and have a broad range of applications in many fields [8, 9]. The reduction of Ag⁺ ions by some biological species and products causes the synthesis of silver nanoparticles with enhancing properties due to an increase in the surface plasmon resonance and large effective scattering cross section of individual nanoparticles [10]. Moreover, the activity of metal nanoparticles at nanostructure level can be easily tuned by varying specific characteristics [11]. These

unique properties of nanoparticles make them a superior and indispensable choice in many areas of biological activity [12].

Anisotropic particles provide greater versatility and options in many cases and applications. Studies suggest that shape of particles is one of the important factors, as most of the intrinsic properties depend on it. Nonspherical nanoparticles such as pentagons, cubes, nanospheres, icosahedrons, hexagons, truncated triangles, triangular prisms, and other more exotic structures of metal nanoparticles exhibit unique and fine-tuned properties which strongly differ and are more pronounced from those of spherical nanoparticles. Their unusual physiochemical property makes them ideal structures and valuable choice to be used for biomedical labelling, optical sensing and imaging, photonics, electronics, catalysis, and electronic devices among others. Furthermore, anisotropic particles provide templates for further synthesis of novel nanomaterials [9, 14]. Anisotropic silver and gold nanoparticles synthesized by chemical, physical, and biological system have been studied and demonstrated for their importance and applications in medical field [15–17].

The antibiotic resistance mechanism in microorganisms has become a major concern and has received considerable attention in the medical field [18]. Silver nanoparticles can play a major role in this area, as they have been found to be active against many multidrug resistant pathogenic microorganisms [19] and in addition, most of the microorganisms are less likely to develop defense mechanisms against metals as compared to antibiotics. Thus, here we report the biosynthesis of anisotropic silver nanoparticles by bacterial strain isolated from four-year-old *Panax ginseng* rhizospheric soil.

P. ginseng is a slow-growing, perennial, and herbal medicinal plant. The rhizospheric soil microflora of the *P. ginseng* have been well studied and explored for various applications such as the bioconversion of ginsenosides [20], plant growth promoting activity [21], and antimicrobial activity [22]. In the present study, a bacterial strain isolated from *P. ginseng* rhizospheric soil is demonstrated to be useful for an application in the field of nanotechnology, that is, for the synthesis of anisotropic silver nanoparticles. The biosynthesized anisotropic silver nanoparticles were characterized by UV-vis, FE-TEM, EDX, elemental mapping, XRD, and DLS. In addition, nanoparticles were tested for their antimicrobial properties against pathogenic microorganisms including *Bacillus anthracis*, *Vibrio parahaemolyticus*, *Salmonella enterica*, *Staphylococcus aureus*, *Escherichia coli*, *Bacillus cereus*, and *Candida albicans*. Furthermore, the silver nanoparticles have been tested in combination with commercial antibiotics including lincomycin, oleandomycin, novobiocin, vancomycin, penicillin G, rifampicin, and cycloheximide, for their ability to enhance the antibiotics' antimicrobial effects against pathogenic microorganisms.

2. Experimental

2.1. Media, Chemicals, and Microorganism. All media used were purchased from Difco, MB cell, Seoul, Korea. Analytical-grade silver nitrate (AgNO_3) and cycloheximide were purchased from Sigma-Aldrich Chemicals, USA. All

antibiotics used were purchased from Oxoid Ltd., England: vancomycin (VA30) 30 $\mu\text{g}/\text{disk}$, rifampicin (RD5) 5 $\mu\text{g}/\text{disk}$, oleandomycin (OL15) 15 $\mu\text{g}/\text{disk}$, penicillin G (P10) 10 $\mu\text{g}/\text{disk}$, novobiocin (NV30) 30 $\mu\text{g}/\text{disk}$, and lincomycin (MY15) 15 $\mu\text{g}/\text{disk}$.

The pathogenic bacterial strains used *Bacillus anthracis* [NCTC 10340], *Vibrio parahaemolyticus* [ATCC 33844], *Salmonella enterica* [ATCC 13076], *Staphylococcus aureus* [ATCC 6538], *Escherichia coli* [ATCC 10798], *Bacillus cereus* [ATCC 14579], and *Candida albicans* [KACC 30062]. The bacterial strains were cultured on nutrient agar media at 37°C and preserved at –70°C in glycerol stock vials for further study. *C. albicans* was cultured on Sabouraud dextrose agar at 28°C and preserved at –70°C in glucose yeast peptone broth (GYP) glycerol stocks vials.

2.2. Isolation of Bacteria. A bacterial strain DC1 was isolated from four-year-old *P. ginseng* rhizospheric soil (Sodang, Republic of Korea) on tryptic soy agar (TSA) and incubated at 30°C for 24 h. Its genomic DNA was extracted using a commercial genomic DNA extraction kit (Core Bio System). The 16S rRNA gene was amplified from the chromosomal DNA of the isolated strain using the universal bacterial primer set 27F, 518F, 800R, and 1512R [23, 24]. The purified PCR products were sequenced by Genotech (Daejeon, Korea). The 16S rRNA gene sequences of related taxa were obtained from the GenBank database and EzTaxon-e server [25].

2.3. Extracellular Synthesis of Silver Nanoparticles. The biological synthesis of silver nanoparticles was carried out as reported [11] with slight modification. Briefly, the bacteria were grown in tryptic soy broth (TSB) and kept in incubation for 24 h in a shaker held at 37°C and 120 rpm. The culture was then centrifuged at 8000 rpm for 5 min and the supernatant was used for the synthesis of silver nanoparticles. AgNO_3 was added to the culture supernatant to reach the concentration of 1 mM, and this reaction mixture was incubated in the orbital shaker at 200 rpm and 25°C. The extracellular synthesis of silver nanoparticles was monitored by visual inspection for a change in the color of the culture medium. After incubation was complete, the reaction mixture was first centrifuged at 2000 rpm for 5 min to remove any medium components, and then the biosynthesized silver nanoparticles were collected by high-speed centrifugation at 16000 rpm for 20 min. The product obtained was washed several times by centrifugation and redispersion in water to remove the unconverted silver ions and any medium components. Finally, the silver nanoparticles were collected in the form of a pellet and used for characterization.

2.4. Characterization of Silver Nanoparticles. UV-vis, FE-TEM, EDX, elemental mapping (quantitation method: Cliff-Lorimer ratio), and DLS were used to characterize the size, shape, composition, and other properties of the silver nanoparticles. The bioreduction was monitored by using a UV-vis spectrophotometer (Ultrospec 2100 pro); this was carried out by scanning the absorbance spectra of the reaction mixture over the wavelength range of 300–700 nm. TEM,

EDX, and elemental mapping were performed by using a FE-TEM (JEM-2100F, JEOL) operated at 200 kV. Samples for FE-TEM, EDX, and elemental mapping were prepared by dropping the unstained silver nanoparticles pellet solution onto a carbon-coated copper grid and drying in an oven at 60°C. FE-TEM was used for structural characterization of nanoparticles. EDX and elemental mapping were used to study the distribution of elements. The X-ray diffraction (XRD) analyses were performed on X-ray diffractometer, D8 Advance, Bruker, Germany, operated at 40 kV, 40 mA, with CuK α radiation, at a scanning rate of 6°/min, step size 0.02, over the 2θ range of 20–80°. The silver nanoparticles have been collected by centrifugation and washing several times with sterile water. Then, the particles were finally recovered by air drying and obtained in powder form.

DLS (particles size analyzer, Potal, Otsuka Electronics, Japan) was used to monitor size distribution profile of biologically synthesized silver nanoparticles. The hydrodynamic diameters and polydispersity index (PDI) were analysed at 25°C. As a reference dispersive medium pure water with refractive index 1.3328, viscosity 0.8878, and dielectric constant 78.3 was used.

The stability of silver nanoparticles was observed by keeping the anisotropic silver nanoparticles reaction mixture for different time interval at room temperature. In addition, the effect of change in pH on the stability of the silver nanoparticles was studied. The sodium hydroxide solution was added in the range of 4–10 pH and then the solution has been scanned by UV-vis spectrophotometer to observe the absorbance.

2.5. Analysis of Antimicrobial Activity of Silver Nanoparticles. Antimicrobial activity of the silver nanoparticles against pathogenic microorganisms, *S. aureus*, *B. anthracis*, *V. parahaemolyticus*, *S. enterica*, *E. coli*, *B. cereus*, and *C. albicans*, was tested by the well diffusion method, carried out using Muller-Hinton agar (MHA) plates. An overnight log-phase culture of each strain was spread evenly on an MHA plate by using a glass spreader. Wells were made on the MHA plates by using a gel puncture. 50 μ L of the biosynthesised silver nanoparticles reaction mixture was added into each of four wells and the plates were incubated at 37°C for 24 h.

Simultaneously, the synergistic effects of different commercial antibiotics with silver nanoparticles were also tested by the disk diffusion method. Similarly, an overnight log-phase culture of each strain was spread evenly on an MHA plate. Then, antibiotic disk of each of the commercial antibiotics was placed on the plate, and 30 μ L of a 100 ppm solution of silver nanoparticles was added over each disk (10 μ L, 3 times). Antibiotic disks without silver nanoparticles were used as negative control. The plates were allowed to dry and then incubated at 37°C for 24 h. After incubation, the susceptibility pattern of the test organisms was determined by measuring the diameter of the zone of inhibition for both the well diffusion and disk diffusion methods. Similarly, cycloheximide antimicrobial activity against *C. albicans* was evaluated and compared with addition of silver nanoparticles with same concentration.

3. Results and Discussion

3.1. Isolation and Identification of Bacteria. The bacterial strain DC1 used herein to carry out the extracellular biosynthesis of silver nanoparticles was isolated from four-year-old *P. ginseng* rhizospheric soil and showed 99.79% similarity with *Bhargavaea indica* [26]. The strain *Bhargavaea indica* DC1 16S rRNA sequence has been submitted to NCBI with accession number KM819013. The strain has been deposited to KCTC culture collection (KCTC 33595).

3.2. Synthesis and Characterization of Silver Nanoparticles. In this study, silver nanoparticles were successfully synthesised extracellularly in the culture supernatant of *B. indica* DC1.

The first indication of silver nanoparticles synthesis was that, upon addition of 1 mM silver nitrate into the flask containing a 24 h culture supernatant of the strain, the medium gradually turned brown, whereas no color change was observed in the control without bacteria. This brown color could be due to the excitation of surface plasmon vibrations, which would arise from the formation of silver nanoparticles in the reaction mixture [11]. Interestingly, the culture supernatant incubated with 1 mM silver nitrate mediated the biosynthesis of silver nanoparticles within 48 h. The 1 mM concentration for the synthesis of silver nanoparticles was selected based on the silver nitrate tolerating capacity of the isolate *B. indica* DC1. The strain showed optimum growth at 1 mM concentration. Moreover, the concentration of precursor (0.1–1 mM) for the synthesis of nanoparticles does not show any effect on the end product of reaction; thus the shape and size of nanoparticles were not affected by the precursor concentration ranging.

UV-vis is the most established method for structural characterization of metal nanoparticles. The reduction of silver ions during exposure to the supernatant of the strain DC1 was easily monitored by UV-vis. After the incubation period, the reaction mixture was scanned in the range of 300–700 nm, showing a major absorbance peak at 460 nm (Figure 1(a)). The broad peak is due to the anisotropic nature of the particles. It has been reported that the band in this region corresponds to the surface plasmon resonance of silver nanoparticles [27]. Thus, the reaction mixture indicates the formation of silver nanoparticles. The nanoparticles synthesize extracellularly, avoiding the downstream processing needed for intracellular synthesis.

Various researchers have reported evidence of the extracellular biosynthesis of silver nanoparticles, including TEM structural characterizations [28]. The anisotropic silver nanoparticles synthesised were successfully characterized by FE-TEM and revealed that the particles ranged in size from 30 to 100 nm and were of various shapes including nanobar, pentagon, spherical, icosahedron, hexagonal, truncated triangle, and triangular shapes (Figure 1(b)). Although the monodispersity is the main issue associated with the nanoparticles synthesis, the biosynthesised anisotropic silver nanoparticles are of great advantage in biological platforms, since the silver nanoparticles undergo shape-dependent interactions with microorganisms [9]. Reports suggest that the biosynthesised silver nanoparticles of different shapes can be separated by

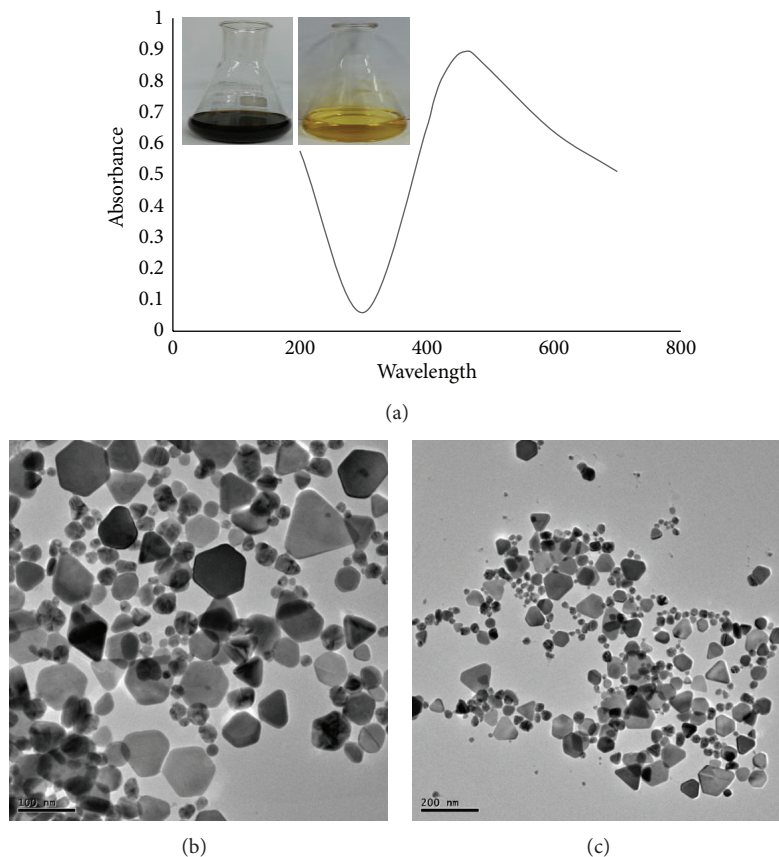


FIGURE 1: UV-vis spectra of culture supernatant of *Bhargavaea indica* DC1 treated with (1 mM) AgNO_3 (a). Transmission electron micrograph of anisotropic silver nanoparticles synthesised by *Bhargavaea indica* DC1, 100 and 200 nm (b).

centrifugation, as the nanoparticles show shape-dependent sedimentation behaviour [29]. The biological synthesis of anisotropic gold and silver nanoparticles by *Aspergillus niger* has been reported previously. The syntheses of anisotropic silver nanoparticles by *Morganella psychrotolerans* [30] and anisotropic gold nanoparticles by the fungal strain *Rhizopus oryzae* [31] have been studied. To our knowledge, this is the first report of the ability of *B. indica* DC1 to synthesise silver nanoparticles of various shapes and sizes. The exact mechanism behind the synthesis remains to be elucidated, but based on reports, the enzyme and proteins synthesised extracellularly by bacterial strain in the reaction mixture help in reducing the silver nitrate to silver nanoparticles. Moreover, the particles synthesised without any additional stabilizing and capping agent thus eliminating the main step of chemical synthesis and overcome the limitations. The cell-free supernatant containing extracellular enzymes and proteins functions as a reducing, shape-directing, and stabilizing agent [2, 31].

The purity of the biosynthesised silver nanoparticles was examined by EDX (Figure 2(a)); the EDX spectrum displayed an optical absorption band peak at 3 keV, which is the characteristic peak of nanosized metallic silver, corresponding to surface plasmon resonance [32]. Carbon and copper signals originating in the low-energy part of the spectrum arose from the use of the carbon-coated copper TEM grid. Similar

results have been observed in the study of biosynthesised silver nanoparticles by *Streptomyces hygroscopicus* [33] and mangrove *Streptomyces sp.* BDUKAS10 [6].

Figure 2(b) shows an elemental mapping result for the biosynthesised silver nanoparticles, showing the relative locations of elements in the TEM cross section. Results clearly demonstrate that the maximum deposition corresponds to silver nanoparticles, 55.95%. Other elements observed included carbon, 12.65%, and copper, 28.68%; these two elements were observed due to the carbon-coated copper grid used for TEM structural analysis. Chlorine was also observed in a very low amount, 2.71%, in the cross sections of the nanoparticles themselves. The distribution of silver element was clearly visible in elemental maps and was the predominant element. Thus, the EDX spectrum and elemental mapping gave confirmation that the nanoparticles consisted of silver only [6]. Figure 3 showed the X-ray diffraction pattern of silver nanoparticles and exhibited intense peaks in the whole spectrum of 2θ value ranging from 20 to 80 and this pattern was similar to Bragg's reflection of silver nanocrystals.

The DLS measurements of number, intensity, and volume distribution of nanoparticles show the size range from 50 to 150 nm with an average diameter of 111 nm and PDI 0.233 (Figures 4(a)–4(c)) which is different from the size measured by TEM, that is, 30–100 nm. Reports suggest that the size difference between the particles size analyses by DLS and

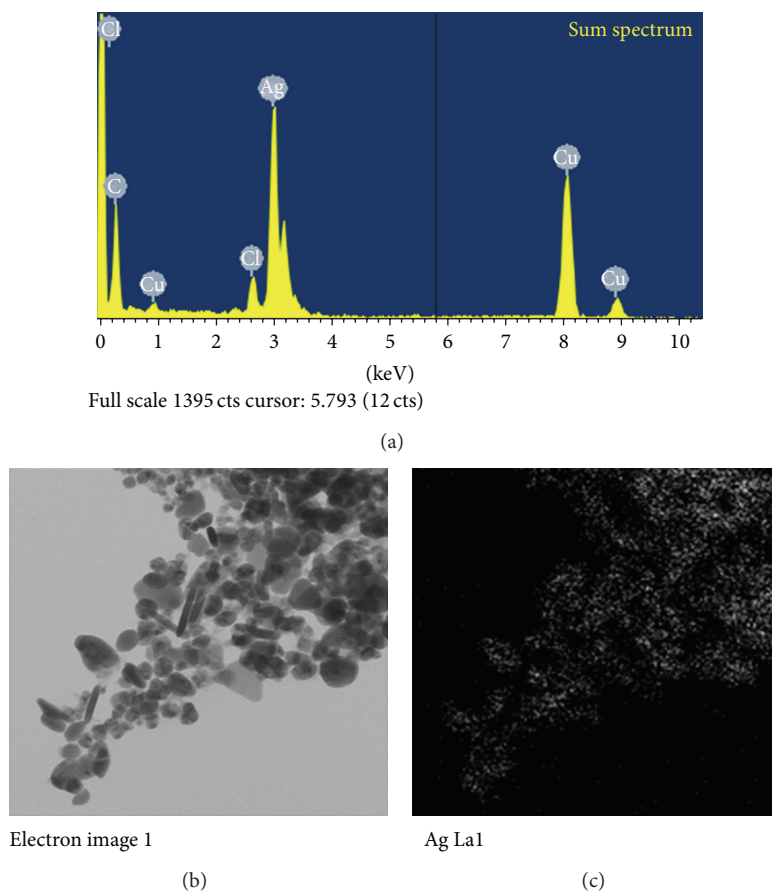


FIGURE 2: EDX spectra of the whole scan area showing major peak of anisotropic silver nanoparticles at 3 keV (a) and TEM micrograph of anisotropic silver nanoparticles pellet solution and silver nanoparticles; 55.95% (b), respectively.

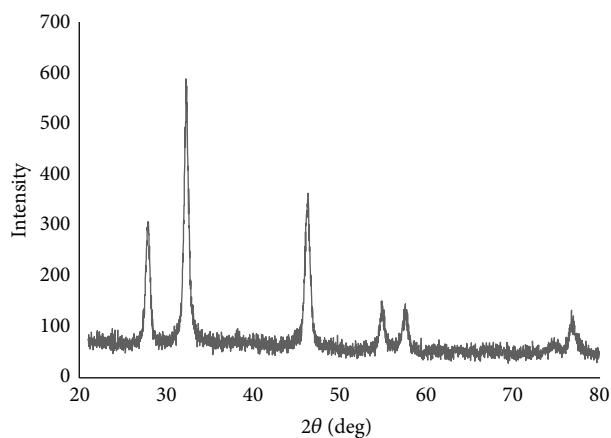


FIGURE 3: X-ray diffraction patterns of anisotropic silver nanoparticles obtained by *Bhargavaea indica* DC1.

TEM measurement has difference due to the fact that TEM visualizes the metallic core of the particles, whereas DLS measures the hydrodynamic diameter of the particles [34]. Thus, *B. indica* DC1 was demonstrated to be suitable for the simple, green, nonhazardous, economical, and eco-friendly

synthesis of antimicrobial anisotropic silver nanoparticles without any additional reducing and stabilizing agent.

Based on the incubation of reaction mixture for different time interval at room temperature, the stability of the nanoparticles was observed and was found that there was no observable variation in the UV-vis spectrum, which directed the stable nature of the anisotropic silver nanoparticles. In addition, the silver nanoparticles solution was observed before and after the addition of sodium hydroxide. In results, no major change in the wavelength was observed, which further confirmed the stability.

3.3. Antimicrobial Activity of Silver Nanoparticles against Test Microorganisms. The biosynthesised silver nanoparticles displayed antimicrobial activity against a range of pathogenic microorganisms such as *C. albicans*, *V. parahaemolyticus*, *S. aureus*, *B. anthracis*, *B. cereus*, *S. enterica*, and *E. coli* (Figure 5). The mean diameter of the zone of inhibition of all the four wells was determined for each microorganism, showing that the silver nanoparticles had the greatest antimicrobial activity against *C. albicans*, followed by *V. parahaemolyticus*, *S. aureus*, *B. anthracis*, *B. cereus*, *S. enterica*, and then *E. coli*. The study has been done in duplicate and average results were interpreted in Table 1. The results clearly indicate that

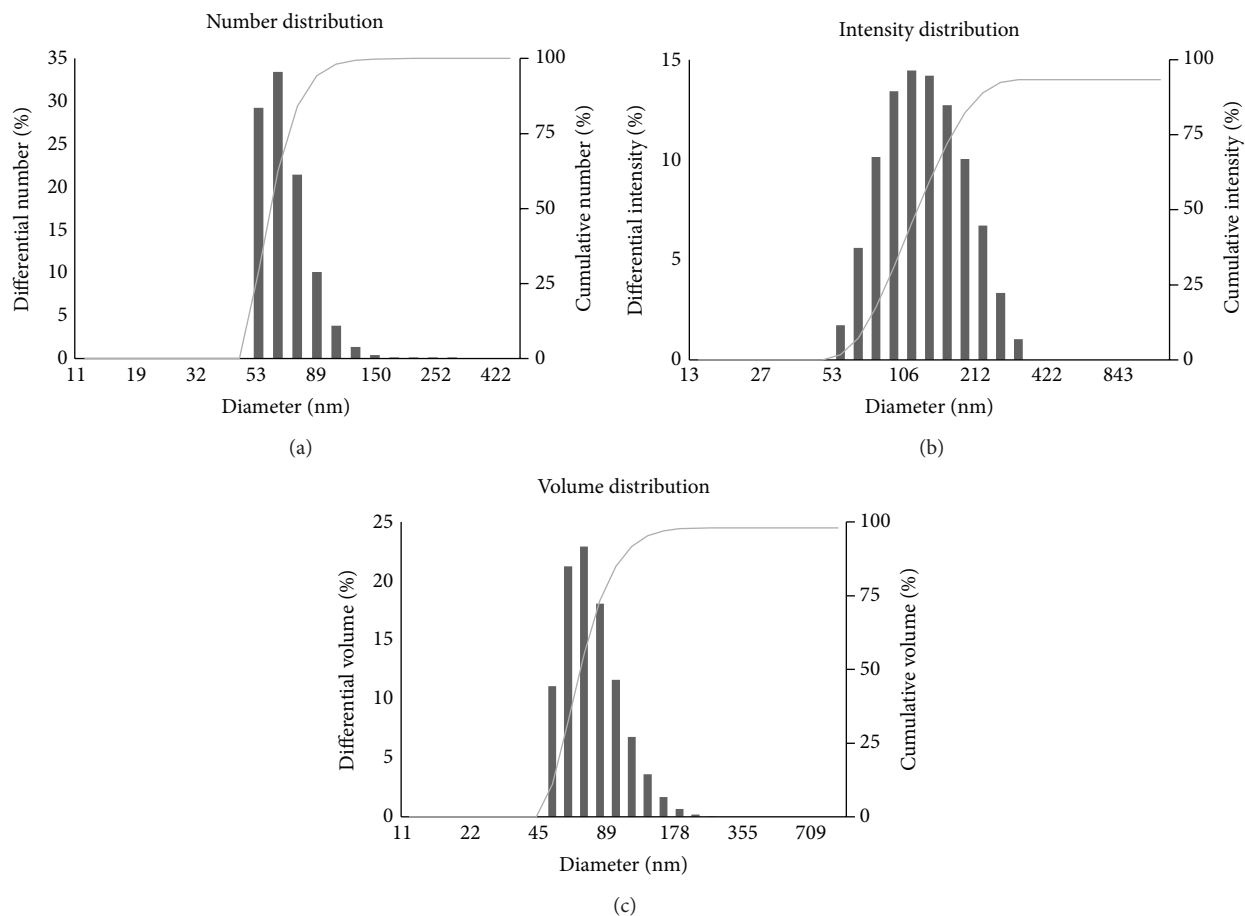


FIGURE 4: Particles size distribution of anisotropic silver nanoparticles according to number (a), intensity (b), and volume (c), respectively.

silver nanoparticles exert antimicrobial activity against tested microorganisms. Many studies have reported the antimicrobial activity of silver nanoparticles against pathogenic microorganisms [7, 11]. However, the mechanism of the metal nanoparticles' inhibitory action is still not clearly understood. There are reports suggesting that (i) the electrostatic attraction between the negatively charged bacterial cell and the positively charged nanoparticles leads to accumulation of nanoparticles on the bacterial membrane, resulting in an increase in cell permeability, (ii) the association of silver with oxygen and its reaction with sulphhydryl (S-H) groups on the cell wall forms R-S-S-R bonds, thereby blocking respiration, (iii) the silver nanoparticles interact with bacterial proteins, which finally leads to cell death, and (iv) the nanoparticles release silver ion which provide additional bactericidal effect [35].

The combination of silver nanoparticles with different commercial antibiotics was evaluated to determine its activity against six pathogenic bacteria using the disk diffusion method. Figure 6(a) represents the antimicrobial activity of partially purified silver nanoparticles and standard antibiotics antimicrobial activity against *S. enterica*, *E. coli*, *V. parahaemolyticus*, *B. anthracis*, *B. cereus*, and *S. aureus*, respectively. The synergistic effect of antibiotics

TABLE 1: Diameter of zone of inhibition (mm) of reaction mixture (50 μ L) containing anisotropic silver nanoparticles against pathogenic microorganisms.

| Number | Pathogenic microorganism | Zone of inhibition (mm) [†] |
|--------|---|--------------------------------------|
| 1 | <i>Candida albicans</i> [KACC 30062] | 23 \pm 0.5 |
| 2 | <i>Vibrio parahaemolyticus</i> [ATCC 33844] | 22 \pm 1 |
| 3 | <i>Staphylococcus aureus</i> [ATCC 6538] | 18 \pm 0.8 |
| 4 | <i>Bacillus anthracis</i> [NCTC 10340] | 16 \pm 0.6 |
| 5 | <i>Bacillus cereus</i> [ATCC 14579] | 15 \pm 0.4 |
| 6 | <i>Salmonella enterica</i> [ATCC 13076] | 14 \pm 1 |
| 7 | <i>Escherichia coli</i> [ATCC 10798] | 10 \pm 1 |

[†] Mean diameter of four wells, 50 μ L reaction mixture containing anisotropic silver nanoparticles.

(lincomycin, oleandomycin, novobiocin, vancomycin, penicillin G, and rifampicin) with biosynthesised silver nanoparticles increased the susceptibility of the tested microorganisms (Figure 6(b)). The disk diffusion tests clearly indicated that the strains of *S. enterica*, *E. coli*, and *V. parahaemolyticus* were completely resistant to the antibiotics, whereas the bacterial strains showed sensitivity to the disks when anisotropic

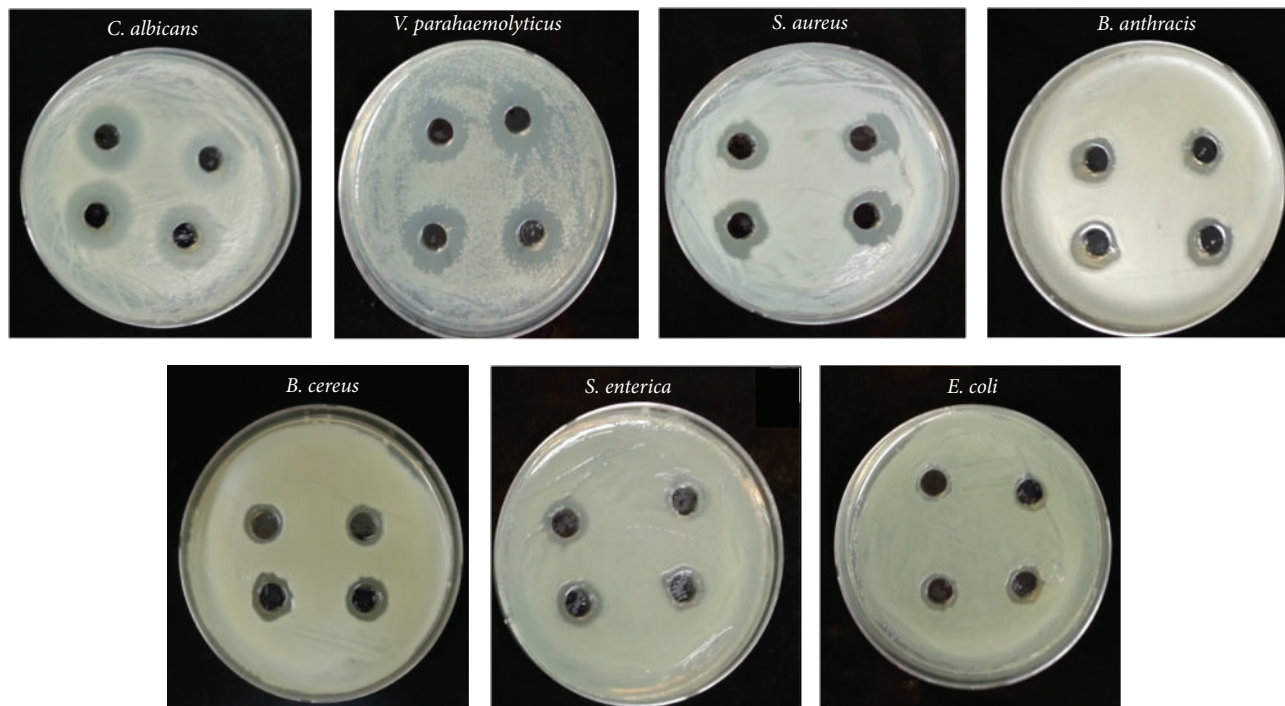


FIGURE 5: Zones of inhibition of 50 μL of reaction mixture containing anisotropic silver nanoparticles against pathogenic strains including *Candida albicans*, *Vibrio parahaemolyticus*, *Staphylococcus aureus*, *Bacillus anthracis*, *Bacillus cereus*, *Salmonella enterica*, and *Escherichia coli*, respectively.

TABLE 2: Individual and combined efficacy of commercial antibiotics with biosynthesised anisotropic silver nanoparticles against pathogenic microorganisms.

| Pathogenic strain | MY15 (a) | MY15 + AgNPs (b) | FA [‡] | OL15 (a) | OL15 + AgNPs (b) | FA [‡] | NV30 (a) | NV30 + AgNPs (b) | FA [‡] |
|----------------------------|----------------|---------------------|-----------------|----------------|---------------------|-----------------|----------------|---------------------|-----------------|
| <i>S. enterica</i> | 0 [†] | 12 \pm 0.5 | 3 | 0 [†] | 12 \pm 0.2 | 3 | 0 [†] | 14 \pm 0.9 | 4.44 |
| <i>E. coli</i> | 0 [†] | 13 \pm 0.3 | 3.69 | 0 [†] | 13 \pm 0.6 | 3.69 | 0 [†] | 14 \pm 1 | 4.44 |
| <i>V. parahaemolyticus</i> | 0 [†] | 15 \pm 0.4 | 5.25 | 0 [†] | 15 \pm 0.3 | 5.25 | 0 [†] | 17 \pm 0.6 | 7.02 |
| Average | | | 3.98 | | | 3.98 | | | 5.3 |
| <i>B. anthracis</i> | 14 \pm 0.1 | 16 \pm 0.1 | 0.31 | 15 \pm 0.4 | 18 \pm 0.2 | 0.44 | 19 \pm 0.2 | 22 \pm 0.3 | 0.34 |
| <i>B. cereus</i> | 16 \pm 0.2 | 18 \pm 0.6 | 0.26 | 22 \pm 0.3 | 24 \pm 0.5 | 0.19 | 22 \pm 0.1 | 25 \pm 0.4 | 0.29 |
| <i>S. aureus</i> | 25 \pm 0.1 | 28 \pm 0.5 | 0.25 | 22 \pm 0.2 | 25 \pm 0.7 | 0.29 | 30 \pm 0.3 | 34 \pm 1 | 0.28 |
| Average | | | 0.27 | | | 0.31 | | | 0.30 |
| Pathogenic strain | VA30 (a) | VA30 + AgNPs (b) | FA [‡] | P10 (a) | P10 + AgNPs (b) | FA [‡] | RD5 (a) | RD5 + AgNPs (b) | FA [‡] |
| <i>S. enterica</i> | 0 [†] | 12 \pm 0.3 | 3 | 0 [†] | 12 \pm 1 | 3 | 0 [†] | 13 \pm 0.5 | 3.69 |
| <i>E. coli</i> | 0 [†] | 13 \pm 0.4 | 3.69 | 0 [†] | 13 \pm 1.2 | 3.69 | 0 [†] | 13 \pm 0.2 | 3.69 |
| <i>V. parahaemolyticus</i> | 0 [†] | 14 \pm 0.2 | 4.44 | 0 [†] | 14 \pm 1.5 | 4.44 | 0 [†] | 15 \pm 0.3 | 5.25 |
| Average | | | 3.71 | | | 3.71 | | | 4.21 |
| <i>B. anthracis</i> | 15 \pm 0.5 | 19 \pm 0.7 | 0.6 | 0 [†] | 15 \pm 0.5 | 5.25 | 12 \pm 0.2 | 16 \pm 0.7 | 0.78 |
| <i>B. cereus</i> | 17 \pm 0.2 | 20 \pm 0.6 | 0.38 | 8 \pm 0.3 | 16 \pm 0.8 | 3 | 13 \pm 0.3 | 15 \pm 0.4 | 0.33 |
| <i>S. aureus</i> | 16 \pm 0.4 | 20 \pm 0.2 | 0.56 | 36 \pm 0.5 | 40 \pm 0.8 | 0.23 | 27 \pm 0.4 | 29 \pm 0.6 | 0.15 |
| Average | | | 0.52 | | | 2.83 | | | 0.42 |
| Pathogenic strain | CHX | | CHX + AgNPs | | FA [‡] | | | | |
| <i>C. albicans</i> | 0 [†] | | 13 \pm 0.5 | | 3.69 | | | | |

Notes. [†]In the absence of bacterial growth inhibition zones, the disc's diameter (6 mm) was used to calculate the fold increases [13].

[‡]Increase in fold area (FA) = $(b^2 - a^2)/a^2$.

MY15: lincomycin 15 $\mu\text{g}/\text{disk}$, OL15: oleandomycin 15 $\mu\text{g}/\text{disk}$, VA30: vancomycin 30 $\mu\text{g}/\text{disk}$, NV30: novobiocin 30 $\mu\text{g}/\text{disk}$, P10: penicillin G 10 $\mu\text{g}/\text{disk}$, and RD5: rifampicin 5 $\mu\text{g}/\text{disk}$; CHX: cycloheximide, 10 $\mu\text{g}/\text{disk}$; AgNPs: biosynthesised anisotropic silver nanoparticles, 30 μL (100 ppm).

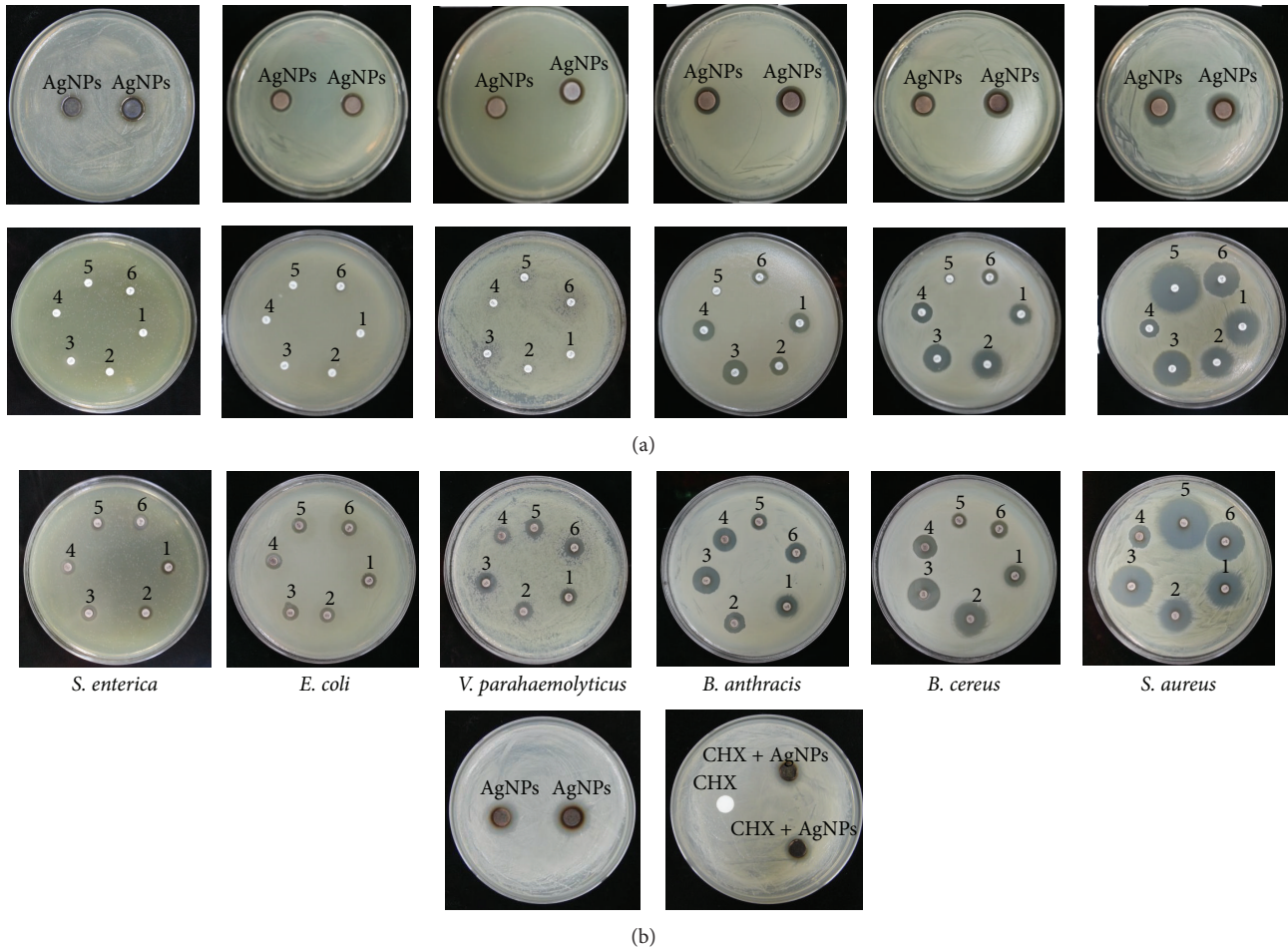


FIGURE 6: Zones of inhibition of partially purified silver nanoparticles pellet solution $30 \mu\text{L}$ (100 ppm) and standard antibiotics as control, against *Salmonella enterica*, *Escherichia coli*, *Vibrio parahaemolyticus*, *Bacillus anthracis*, *Bacillus cereus*, and *Staphylococcus aureus*, respectively (a). Zones of inhibition of standard antibiotics disks with anisotropic silver nanoparticles against *Salmonella enterica*, *Escherichia coli*, *Vibrio parahaemolyticus*, *Bacillus anthracis*, *Bacillus cereus*, *Staphylococcus aureus*, and *Candida albicans* (b), respectively. Note. (1) Lincomycin (MY15) $15 \mu\text{g}/\text{disk}$, (2) oleandomycin (OL15) $15 \mu\text{g}/\text{disk}$, (3) novobiocin (NV30) $30 \mu\text{g}/\text{disk}$, (4) vancomycin (VA30) $30 \mu\text{g}/\text{disk}$, (5) penicillin G (P10) $10 \mu\text{g}/\text{disk}$, and (6) rifampicin (RD5) $5 \mu\text{g}/\text{disk}$; cycloheximide (CHX) $10 \mu\text{g}/\text{disk}$ and anisotropic silver nanoparticles (AgNPs) $30 \mu\text{L}$ (100 ppm).

silver nanoparticle solution was added and results in the formation of a zone of inhibition for *S. enterica*, *E. coli*, and *V. parahaemolyticus*. The average increase in sensitivity pattern of antibiotics was calculated by average increase in fold area [35]. The average increase in fold area of the antibiotics against antibiotic resistant microorganisms was greatest for novobiocin, followed by rifampicin, lincomycin, and oleandomycin and then vancomycin and penicillin G. Similar results regarding increase in fold area have been observed against multidrug resistant *E. coli* [16]. The other pathogenic stains showed susceptibility to antibiotics disks alone, *B. anthracis*, *B. cereus*, and *S. aureus*, and showed increased susceptibility when the disks were combined with anisotropic silver nanoparticle solution, observed as increases in the diameter of the zone of inhibition for *B. anthracis*, *B. cereus*, and *S. aureus*. This clearly indicated the effect of biosynthesised anisotropic silver nanoparticles in enhancing the antimicrobial action of antibiotics.

The average increase in fold area against antibiotic sensitive microorganism, when anisotropic silver nanoparticles were added, was greatest for penicillin G, followed by vancomycin, rifampicin, oleandomycin, novobiocin, and lincomycin. In addition, in case of cycloheximide, the similar pattern of action was found against *C. albicans*. On the addition of silver nanoparticles with cycloheximide, the activity of cycloheximide increases. The study has been done in duplicate and average results were interpreted in Table 2. The present study shows results similar to those of a line of studies that presented increased efficacies of commercial antibiotics against pathogenic microorganisms [13, 16, 28]. It indicates that biosynthesised anisotropic silver nanoparticles show antimicrobial activity against pathogenic microorganisms. Moreover, the nanoparticles were shown to enhance the effect of commercial antibiotics against multidrug resistant bacteria. Thus, the biosynthesised anisotropic silver nanoparticles are ready for applications in the clinical field against

pathogenic microorganisms, although the exact mechanism of their action remains to be elucidated.

4. Conclusions

The most important advantage of this approach includes the possibility to obtain anisotropic silver nanoparticles of nanobar, pentagon, spherical, icosahedron, hexagonal, truncated triangle, and triangular shapes by *Bhargavaea indica* DC1. The anisotropic silver nanoparticles were synthesized by eco-friendly and economical manner and eliminating the hazardous effects of physiochemical synthesis. Moreover, the particles were synthesized extracellularly, without any extra reducing and capping agent, thus excluding the extra step in physiochemical synthesis. Furthermore, the methodology has greater advantage of easy bulk synthesis which can be exploited for large scale industrial scale-up production due to easy downstream processing.

The outcomes of study also indicated that the biosynthesized anisotropic silver nanoparticles had inherent antimicrobial activity and also enhanced the antimicrobial activity of commercial antibiotics against pathogenic microorganisms. The biosynthesized silver nanoparticles may have potential to be used as multifunctional nanoparticles for different applications on medical, clinical, and biological background such as targeting, diagnosis, drug delivery, and photoimaging. Further studies in order to understand the mechanism of action, surface engineering, specific targeting, and conjugation may be useful to develop novel nanoparticles for different applications.

Conflict of Interests

The authors declare that there is no conflict of interests regarding the publication of this paper.

Acknowledgments

This research was supported by the Korea Institute of Planning and Evaluation for Technology in Food, Agriculture, Forestry and Fisheries (KIPET no. 313038-03-2-SB010) and by a Next-Generation BioGreen 21 Program (SSAC, Grant no.: PJ009529032014) of the Republic of Korea.

References

- [1] L. Zhang, F. X. Gu, J. M. Chan, A. Z. Wang, R. S. Langer, and O. C. Farokhzad, "Nanoparticles in medicine: therapeutic applications and developments," *Clinical Pharmacology and Therapeutics*, vol. 83, no. 5, pp. 761–769, 2008.
- [2] N. Kulkarni and U. Muddapur, "Biosynthesis of metal nanoparticles: a review," *Journal of Nanotechnology*, vol. 2014, Article ID 510246, 8 pages, 2014.
- [3] M. Kowshik, S. Ashtaputre, S. Kharrazi et al., "Extracellular synthesis of silver nanoparticles by a silver-tolerant yeast strain MKY3," *Nanotechnology*, vol. 14, no. 1, p. 95, 2003.
- [4] N. Jain, A. Bhargava, S. Majumdar, J. C. Tarafdar, and J. Panwar, "Extracellular biosynthesis and characterization of silver nanoparticles using *Aspergillus flavus* NJP08: a mechanism perspective," *Nanoscale*, vol. 3, no. 2, pp. 635–641, 2011.
- [5] J. J. Antony, P. Sivalingam, D. Siva et al., "Comparative evaluation of antibacterial activity of silver nanoparticles synthesized using *Rhizophora apiculata* and glucose," *Colloids and Surfaces B: Biointerfaces*, vol. 88, no. 1, pp. 134–140, 2011.
- [6] P. Sivalingam, J. J. Antony, D. Siva, S. Achiraman, and K. Anbarasu, "Mangrove *Streptomyces* sp. BDUKAS10 as nanofactory for fabrication of bactericidal silver nanoparticles," *Colloids and Surfaces B: Biointerfaces*, vol. 98, pp. 12–17, 2012.
- [7] M. A. Dar, A. Ingle, and M. Rai, "Enhanced antimicrobial activity of silver nanoparticles synthesized by *Cryphonectria* sp. evaluated singly and in combination with antibiotics," *Nanomedicine: Nanotechnology, Biology, and Medicine*, vol. 9, no. 1, pp. 105–110, 2013.
- [8] A. R. Shahverdi, A. Fakhimi, H. R. Shahverdi, and S. Minaian, "Synthesis and effect of silver nanoparticles on the antibacterial activity of different antibiotics against *Staphylococcus aureus* and *Escherichia coli*," *Nanomedicine: Nanotechnology, Biology, and Medicine*, vol. 3, no. 2, pp. 168–171, 2007.
- [9] S. Pal, Y. K. Tak, and J. M. Song, "Does the antibacterial activity of silver nanoparticles depend on the shape of the nanoparticle? A study of the gram-negative bacterium *Escherichia coli*," *Applied and Environmental Microbiology*, vol. 73, no. 6, pp. 1712–1720, 2007.
- [10] S. Prabhu and E. K. Poulouse, "Silver nanoparticles: mechanism of antimicrobial action, synthesis, medical applications, and toxicity effects," *International Nano Letters*, vol. 2, no. 1, article 32, 2012.
- [11] S. Gurunathan, K. Kalishwaralal, R. Vaidyanathan et al., "Biosynthesis, purification and characterization of silver nanoparticles using *Escherichia coli*," *Colloids and Surfaces B: Biointerfaces*, vol. 74, no. 1, pp. 328–335, 2009.
- [12] N. Sanvicens and M. P. Marco, "Multifunctional nanoparticles—properties and prospects for their use in human medicine," *Trends in Biotechnology*, vol. 26, no. 8, pp. 425–433, 2008.
- [13] S. S. Birla, V. V. Tiwari, A. K. Gade, A. P. Ingle, A. P. Yadav, and M. K. Rai, "Fabrication of silver nanoparticles by *Phoma glomerata* and its combined effect against *Escherichia coli*, *Pseudomonas aeruginosa* and *Staphylococcus aureus*," *Letters in Applied Microbiology*, vol. 48, no. 2, pp. 173–179, 2009.
- [14] M. Tréguer-Delapierre, J. Majimel, S. Mornet, E. Duguet, and S. Ravaine, "Synthesis of non-spherical gold nanoparticles," *Gold Bulletin*, vol. 41, no. 2, pp. 195–207, 2008.
- [15] S. S. Shankar, A. Ahmad, R. Pasricha, and M. Sastry, "Bioreduction of chloroaurate ions by geranium leaves and its endophytic fungus yields gold nanoparticles of different shapes," *Journal of Materials Chemistry*, vol. 13, no. 7, pp. 1822–1826, 2003.
- [16] S. Priyadarshini, V. Gopinath, N. Meera Priyadarshini, D. MubarakAli, and P. Velusamy, "Synthesis of anisotropic silver nanoparticles using novel strain, *Bacillus flexus* and its biomedical application," *Colloids and Surfaces B: Biointerfaces*, vol. 102, pp. 232–237, 2013.
- [17] A. M. Goswami and S. Ghosh, "Biological synthesis of colloidal gold nanoparticles using *Penicillium citrinum* MTCC9999," *Journal of Biomaterials and Nanobiotechnology*, vol. 4, no. 2, pp. 20–27, 2013.
- [18] H. H. Lara, N. V. Ayala-Núñez, L. C. I. Turrent, and C. R. Padilla, "Bactericidal effect of silver nanoparticles against multidrug-resistant bacteria," *World Journal of Microbiology and Biotechnology*, vol. 26, no. 4, pp. 615–621, 2010.

- [19] M. K. Rai, S. D. Deshmukh, A. P. Ingle, and A. K. Gade, "Silver nanoparticles: the powerful nanoweapon against multidrug-resistant bacteria," *Journal of Applied Microbiology*, vol. 112, no. 5, pp. 841–852, 2012.
- [20] W. G. Weisburg, S. M. Barns, D. A. Pelletier, and D. J. Lane, "16S ribosomal DNA amplification for phylogenetic study," *Journal of Bacteriology*, vol. 173, no. 2, pp. 697–703, 1991.
- [21] K. K. Kim, M. K. Kim, J. H. Lim, H. Y. Park, and S.-T. Lee, "Transfer of *Chryseobacterium meningosepticum* and *Chryseobacterium miricola* to *Elizabethkingia* gen. nov. as *Elizabethkingia meningoseptica* comb. nov. and *Elizabethkingia miricola* comb. nov.," *International Journal of Systematic and Evolutionary Microbiology*, vol. 55, no. 3, pp. 1287–1293, 2005.
- [22] L. Wang, Q. M. Liu, B. H. Sung et al., "Bioconversion of ginsenosides Rb₁, Rb₂, Rc and Rd by novel beta-glucosidase hydrolyzing outer 3-O glycoside from *Sphingomonas* sp. 2F2: cloning, expression, and enzyme characterization," *Journal of Biotechnology*, vol. 156, no. 2, pp. 125–133, 2011.
- [23] R. T. Vendan, Y. J. Yu, S. H. Lee, and Y. H. Rhee, "Diversity of endophytic bacteria in ginseng and their potential for plant growth promotion," *Journal of Microbiology*, vol. 48, no. 5, pp. 559–565, 2010.
- [24] K. M. Cho, S. Y. Hong, S. M. Lee et al., "Endophytic bacterial communities in ginseng and their antifungal activity against pathogens," *Microbial Ecology*, vol. 54, no. 2, pp. 341–351, 2007.
- [25] O.-S. Kim, Y.-J. Cho, K. Lee et al., "Introducing EzTaxon-e: a prokaryotic 16s rRNA gene sequence database with phylotypes that represent uncultured species," *International Journal of Systematic and Evolutionary Microbiology*, vol. 62, part 3, pp. 716–721, 2012.
- [26] P. Verma, C. N. Seong, P. K. Pandey et al., "*Bhargavaea indica* sp. nov., a member of the phylum *Firmicutes*, isolated from Arabian Sea sediment," *Journal of Microbiology*, vol. 51, no. 1, pp. 36–42, 2013.
- [27] A. Maciolllek and H. Ritter, "One pot synthesis of silver nanoparticles using a cyclodextrin containing polymer as reductant and stabilizer," *Beilstein Journal of Nanotechnology*, vol. 5, no. 1, pp. 380–385, 2014.
- [28] S. Z. H. Naqvi, U. Kiran, M. I. Ali et al., "Combined efficacy of biologically synthesized silver nanoparticles and different antibiotics against multidrug-resistant bacteria," *International Journal of Nanomedicine*, vol. 8, pp. 3187–3195, 2013.
- [29] V. Sharma, K. Park, and M. Srinivasarao, "Shape separation of gold nanorods using centrifugation," *Proceedings of the National Academy of Sciences of the United States of America*, vol. 106, no. 13, pp. 4981–4985, 2009.
- [30] R. Ramanathan, A. P. O'Mullane, R. Y. Parikh, P. M. Smooker, S. K. Bhargava, and V. Bansal, "Bacterial kinetics-controlled shape-directed biosynthesis of silver nanoplates using *Morganella psychrotolerans*," *Langmuir*, vol. 27, no. 2, pp. 714–719, 2011.
- [31] S. K. Das, A. R. Das, and A. K. Guha, "Microbial synthesis of multishaped gold nanostructures," *Small*, vol. 6, no. 9, pp. 1012–1021, 2010.
- [32] H. Schneidewind, T. Schüler, K. K. Strelau et al., "The morphology of silver nanoparticles prepared by enzyme-induced reduction," *Beilstein Journal of Nanotechnology*, vol. 3, no. 1, pp. 404–414, 2012.
- [33] S. Sadhasivam, P. Shanmugam, and K. Yun, "Biosynthesis of silver nanoparticles by *Streptomyces hygroscopicus* and antimicrobial activity against medically important pathogenic microorganisms," *Colloids and Surfaces B: Biointerfaces*, vol. 81, no. 1, pp. 358–362, 2010.
- [34] A. R. Poda, A. J. Bednar, A. J. Kennedy et al., "Characterization of silver nanoparticles using flow-field flow fractionation interfaced to inductively coupled plasma mass spectrometry," *Journal of Chromatography A*, vol. 1218, no. 27, pp. 4219–4225, 2011.
- [35] J. R. Morones, J. L. Elechiguerra, A. Camacho et al., "The bactericidal effect of silver nanoparticles," *Nanotechnology*, vol. 16, no. 10, pp. 2346–2353, 2005.

Research Article

Organic Systems and Their Photorefractive Properties under the Nano- and Biostructuration: Scientific View and Sustainable Development

Natalia V. Kamanina,^{1,2} Sergey V. Serov,¹ Yann Bretonniere,³ and Chantal Andraud³

¹Lab for Photophysics of Media with Nanoobjects, Vavilov State Optical Institute, Kadetskaya Liniya V.O., Dom 5, Korpus 2, St. Petersburg 199053, Russia

²Saint-Petersburg Electrotechnical University "LETI", Prof. Popova Street, Dom 5, St. Petersburg 197376, Russia

³Laboratoire de Chimie, UMR CNRS 5182, Ecole Normale Supérieure de Lyon, France

Correspondence should be addressed to Natalia V. Kamanina; nvkamanina@mail.ru

Received 30 October 2014; Accepted 19 December 2014

Academic Editor: Wei Hsuan Hung

Copyright © 2015 Natalia V. Kamanina et al. This is an open access article distributed under the Creative Commons Attribution License, which permits unrestricted use, distribution, and reproduction in any medium, provided the original work is properly cited.

Essential improvement of the photorefractive parameters of the *organic* structures has been found via nano- and biostructuring process. The spectral and self-assembling features which can support the photorefractive effect of some conjugated materials, including the liquid crystal ones, have been presented. To investigate the laser-induced change of the refractive index of the nano- and bio-objects-doped materials the holographic recording technique has been used. Moreover some innovative perspective dyes have been applied to study the effect of the rotation of the polarization plane of light. The area of application of the modified materials has been discussed. The tendency to replace the nanotechnology process with the biotechnology ones has been predicted.

1. Introduction

Extended area of the optoelectronic and biomedical application [1–5] of the different inorganic and organic compounds requires the search for new methods to optimize the spectral and photorefractive properties of such types of the materials. It is connected with an innovative design and simple way to control the basic physical-technical parameters.

According to the perspective role, namely, of the organic materials in optoelectronics and biomedicine in comparison with the inorganic ones, the optical features of these systems occupy the special place. Among these features the photorefractive parameters responsible for the effects of the laser-matter interaction in the anisotropic media have been considered in more detail.

In the current paper two optical effects coincided with the photorefractivity, such as the laser-induced refractive index changing, and the rotation of the plane of polarization of light is considered based on the model polyimide (PI) photosensitive donor-acceptor matrix and the nematic

liquid crystal (NLC) compounds as well as on the solutions of noncentrosymmetric dyes. It should be mentioned that the organic systems with the initial intramolecular donor-acceptor interaction have been used in order to have the chance to dope them with the intermolecular acceptors with good advantage.

2. Theoretical Background

In order to analyze the optical processes of the materials one should take into account the following. When the electric field of the laser wave is less than the intra-atomic electric field $E_a = e/a^2$ correlated with the electron charge e and with the Bohr radius a , we should estimate the linear effect. But when the electric field of the laser wave is larger than the intra-atomic electric field E_a , we should draw the attention on the nonlinear optical features. Using this aspect, the values of optical susceptibility play important role in nonlinear optical effect. Really, the most important optical characteristic of all organic or inorganic materials with different symmetry

is the induced dipole, which can be expressed through the dipole polarizabilities $\alpha^{(n)}$ [6]. These are in turn related by the proportional dependence to the nonlinear susceptibility $\chi^{(n)}$ and to the local volume v of the materials (media). Thus, laser-matter interaction provokes the change in polarization of media and predicts the change in the important properties, such as dynamic, photorefractive, and photoconductive ones.

To predict the change of the cubic nonlinearity $\chi^{(3)}$, as minimum media local volume polarizability [7–9], the laser-induced change of the refractive index Δn_i can be calculated from the diffraction efficiency η [7–10] via realization of the Raman-Nath diffraction conditions ($\Lambda^{-1} \geq d$) using

$$\eta = \frac{I_1}{I_0} = \left(\frac{\pi \Delta n_i d}{2\lambda} \right)^2. \quad (1)$$

Here Δn_i is induced change of the refractive index, I_1 is the intensity in the first diffraction order, I_0 is the input laser intensity, d is the thickness of the medium, λ is the wavelength of the light incident on the medium, and Λ is the spatial frequency. Due to the fact that the refractive index depends on the light intensity in the media with the cubic nonlinearity, the nonlinear refractive index n_2 can be estimated via (2) and then cubic nonlinearity $\chi^{(3)}$ can be found via (3):

$$n = n_0 + n_2 I, \quad (2)$$

$$n_2 = \frac{16\pi^2}{n_0 c} \chi^{(3)}. \quad (3)$$

Here n_0 is the linear refractive index and c is the light velocity. It should be noticed that generally to calculate the nonlinear optical coefficients of the media with high value of the cubic nonlinearity we have used mechanism proposed in [7] and extended on the nanostructured materials in the publications [8–10].

Based on our previous results [8–12] and the current ones the model polyimide organic matrix and NLCs can be treated by pulsed nanosecond laser with good advantage to observe the dramatic change of the refractive index. Moreover, some anisotropic media based on the organic dyes solutions can support the evidences to use the innovative organic materials in the optical applications to resolve the different complicated tasks not only in the technical area but also in the biomedicine.

3. Experimental Results and Discussion

It should be remarked that the main accents are given on the study of the optical features of the structured organic materials.

3.1. Photorefractive Features of the Organics Activated by Laser Irradiation. The laser-induced change of the refractive index has been studied under the Raman-Nath diffraction conditions at spatial frequency of $90\text{--}120 \text{ mm}^{-1}$ and at the laser energy density of $0.03\text{--}0.6 \text{ J} \times \text{cm}^{-2}$. The scheme has been analogous to that shown in [13] and can be shortly shown in Figure 1.

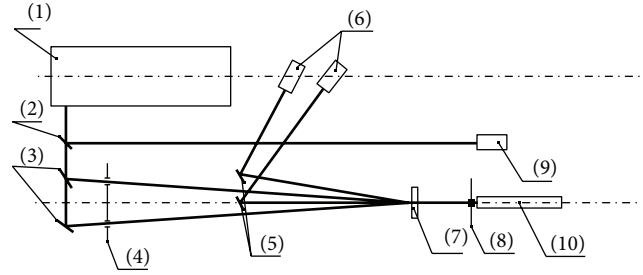


FIGURE 1: (1) Nd-laser with the converter to second harmonic, (2) plane-parallel plate, (3, 5) mirrors, (4, 8) blocking and absorbance diaphragms, (6) photodetectors, (7) samples, (9) synchronized device, and (10) an additional continuous Nd-laser to readout.

The wavelength of the second harmonic of the pulsed nanosecond Nd-laser was 532 nm and the laser pulse width was 10–30 ns. The main results are shown in Table 1. The database of the laser-induced change of the refraction index and thus general nonlinear features of the nano-object-doped materials with different sensitizers can be extended by including DNA.

Let us consider in detail results shown in Table 1. As the promising nanoobject fullerenes, the quantum dots, the shungites, and the carbon nanotubes have been considered as well as the bioparticles based on DNA, we have testified that the model consideration of domination of the *intermolecular* charge transfer under *intramolecular* one using different types and placement of the nanoobjects can be applied with good advantage. It should be mentioned that, in the sensitized organic conjugated system, for example, polyimide one, the pathway of the electrons included in the charge transfer process changes due to the fact that charge transfers from the intramolecular donor fragment of organic conjugated molecules (triphenylamine) not to its acceptor fragment (diimide) but to nanoobjects if the electron affinity energy of the nanoobjects is larger than the one for intramolecular acceptor fragment. For example, electron affinity energy of intramolecular acceptor fragment of polyimide is close to 1.1–1.4 eV, the electron affinity energy of shungite structure is ~ 2 eV, the one for fullerenes is ~ 2.65 eV, and the one for quantum dots is placed in the range of 3.8–4.2 eV. Thus, the intermolecular acceptor fragment electron affinity energy is essentially larger. Therefore, incorporated nanoobjects are stronger sensitizers and they dominate the acceptor fragments of intramolecular complexes. In this case the field gradient is formed, the additional dipole moment is observed, the increase of the local volume polarizability is found, and the increase of dipole polarizability and of the charge carrier mobility is revealed. The first consideration of this process has been made in [8] and extended in [9–12]. Regarding the DNA incorporation in the organic matrixes, it should be mentioned that these bioobjects revealed an additional shift in the spectral characteristics (that can support the possible formation of the charge transfer complex) which can be shown for the solution in Figure 2 and predicted the refractive index change with the value close to that observed before for the nano-object-doped organic materials.

TABLE I: Change of the refractive index Δn_i of the doped polyimides and LCs.

| Numbers | Structure studied | Nanoobject content wt.% | Energy density, $J \times cm^{-2}$ | Δn_i |
|---------|---------------------------------|-------------------------|------------------------------------|-----------------------|
| 1 | Pure polyimide | 0 | 0.6 | $10^{-4}-10^{-5}$ |
| 2 | Polyimide + malachite green dye | 0.2 | 0.6 | 2.87×10^{-4} |
| 3 | Polyimide + dye WD-C4 | 0.05 | 0.2 | 10.0×10^{-3} |
| 4 | Polyimide + QDs CdSe(ZnS) | 0.003 | 0.2-0.3 | 2.0×10^{-3} |
| 5 | Polyimide + C_{70} | 0.2 | 0.6 | 4.68×10^{-3} |
| 6 | Polyimide + C_{60} | 0.2 | 0.5-0.6 | 4.2×10^{-3} |
| 7 | Polyimide + shungite | 0.2 | 0.1-0.3 | 5.3×10^{-3} |
| 8 | NLC + polyimide + C_{70} | 0.2 | 0.1-0.3 | 1.2×10^{-3} |
| 9 | NLC + DNA* | 0.1 | 0.1 | 1.39×10^{-3} |
| 10 | NLC + QDs CdSe(ZnS) + DNA | 0.1 | 0.1 | 1.35×10^{-3} |

*Content of DNA in the water solution was $\sim 4.72 g \times L^{-1}$; the relation between LC and DNA was 5 : 1.

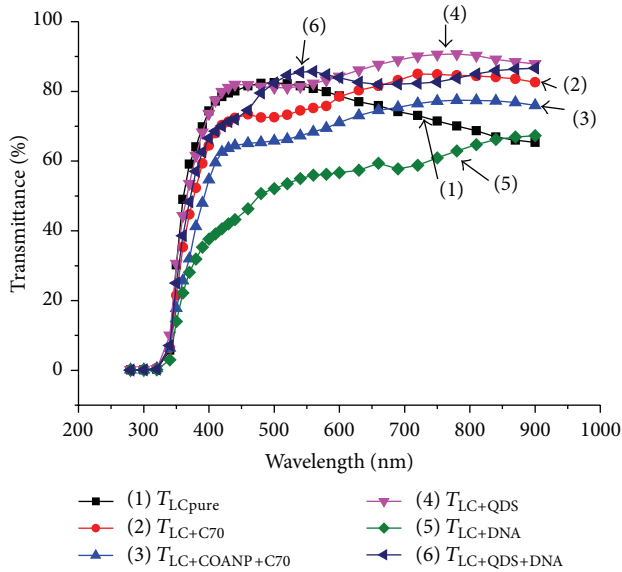


FIGURE 2: Spectral evidence of the formation of the CTC with DNA via observation of the bathochromic shift.

Indeed, the process of the DNA added in the organic matrix should be studied in detail in the future, but now one can testify that these renewable bioobjects can be considered as alternative ones to nanoobjects.

Using the obtained results, the nonlinear refraction n_2 and nonlinear third order optical susceptibility (cubic nonlinearity) $\chi^{(3)}$ for all systems have been calculated using a method described above. It was found that these parameters fall within the range: $n_2 = 10^{-10}-10^{-9} cm^2 \times W^{-1}$ and $\chi^{(3)} = 10^{-10}-10^{-9} cm^3 \times erg^{-1}$. It should be testified that the value of the obtained nonlinear optical coefficients for the organic materials studied in the current research is close to that received for the bulk silicon-based inorganic structures.

3.2. Rotation of the Plane of Polarization of Light. It should be mentioned that generally in order to operate with active media responsible for the rotation of the light polarization plane one can use classical 10% sugar-water solution. But,

using the innovative dyes with less concentration in the solvent, we can observe this effect at the same experimental conditions. The experimental scheme to measure the angle of the polarization plane rotation is shown in Figure 3.

We have used the dyes as JM271-C1 (atomic weight is close to 317.4), YB-C2 (345.5), WD-C4 (401.6), JM47-C7 (485.7), and YB-C11 (597.9). Some dyes formulas are shown in Figure 4.

The spectral results regarding the dyes solution in the tetrachlorethan are shown in Figure 5(a). The change of the rotation angle for the solution with different dyes is shown in Figure 5(b).

One can see that all dyes solutions permit rotating the plane of polarization of light with good advantage. It should be mentioned once again that we have used less content of each dye in the tetrachlorethan solvent than ones applied for traditional 10% sugar-water solution. Moreover, some saturation level has been observed for the molecular weight of dyes close to atomic weight of 375-400. It should be remarked that the 10% sugar-water solution rotates the light polarization plane with the angle of 3° at the same thickness of the cuvette of 10 mm. Thus these dyes can be considered as the alternative agents in comparison with sugar in order to realize the optical rotation effect for the polarization plane of light. Furthermore, for future comparative investigation, it will be necessary to functionalize the dyes in order to solve them in the water.

4. Conclusion

Based on the presented study and to analyze the received results one can say the following.

According to the database of the nonlinear features of the polyimide matrix and nematic liquid crystal materials from cyanobiphenyl group with different sensitizers, it can be prognosed that the different nanoobjects added in the model matrixes and new nature materials, for example, renewable DNA, can be considered as the good candidates to modify the photorefractive features of the organic materials with an initial donor-acceptor interaction. Moreover, it has been established that the nontoxic renewable bioparticles influence the photorefractive features of the organic conjugated

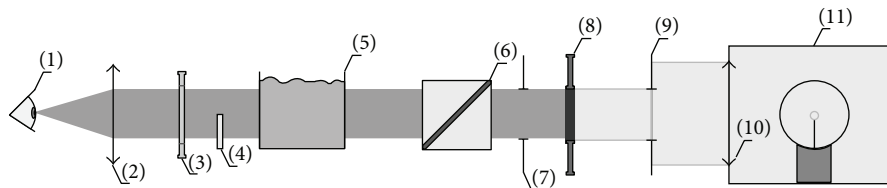


FIGURE 3: (1) Researcher's eye, (2) eyepiece, (3) polarizer, (4) rotated polarizes plate, (5) solution with dyes, (6) polarized prism, (7, 9) diaphragms, (8) filters, (10) lens, and (11) illuminator (lamp or He-Ne-laser at wavelength of 633 nm).

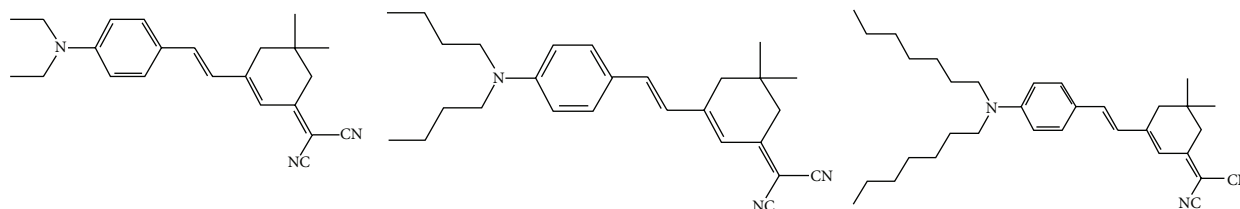


FIGURE 4: The structural formulas of some dyes used in the effect of the rotation of the polarization plane of the light: YB-C2, WD-C4, and JM47-C7 (from the left to right).

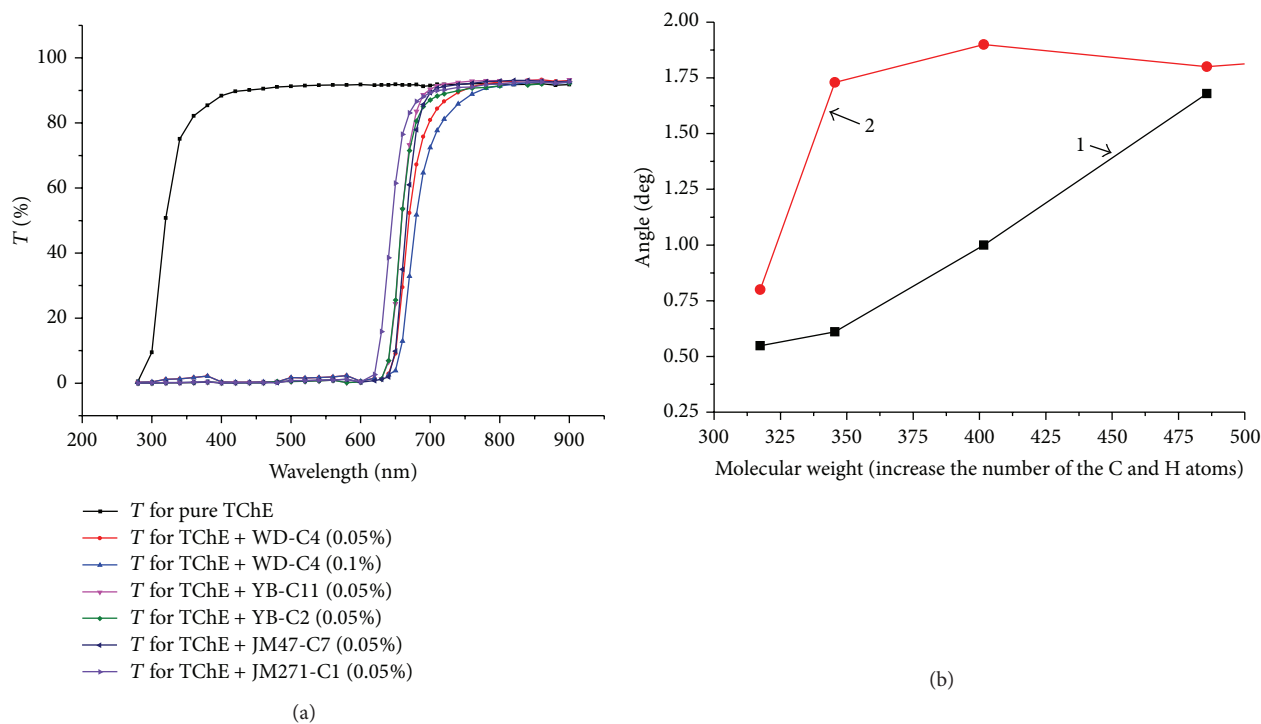


FIGURE 5: Transmittance spectra of the tetrachlorethane solutions of the dyes studied (a) and the dependence of the rotation angle of the polarization plane of light on the dyes molecular weight (b): (1) 0.05% solution and (2) 0.5% solution.

matrixes and can be predicted as alternative bioobjects instead of nanoobjects. For example, organic systems sensitized with the nanoparticles, such as fullerenes C_{60} and C_{70} , carbon nanotubes, or quantum dots, can be replaced by the renewable bioparticles sensitized materials. It can predict to apply the organic materials with DNA for the holographic recording, optical limiting, and the testing of the dynamic properties of the DNA-modified composites and

their possible application in the general telecommunication systems and in the biomedicine. Thus, as an important conclusion, we should tell and predict that the nanotechnology methods and components can be effectively replaced by the biotechnology ones.

Evidences to rotate the polarization plane of the light have been shown using innovative dyes in comparison with that for the general sugar-water solution. The threshold level for

the rotation angle on molecular mass has been established. It has been mentioned that for the future experiments and their explanation the procedure to functionalize the dyes to solve them in water should be needed.

Some unique approaches proposed in this consideration possibly can be useful in order to collect the new knowledge in the nano- and biomaterials science and to extend the area of the application of the structured organic systems. The results presented can be useful to apply them in the education process because the nanomaterials study area permits visualizing some physical effects and explaining some laws of the laser-matter interaction under the conditions of nanodimensional scale. It should be noticed that this study can be useful in order to reveal the new knowledge in the nano- and biostructured organic materials science in comparison with that obtained for the classical inorganic crystals.

Conflict of Interests

The authors declare that there is no conflict of interests regarding the publication of this paper.

Acknowledgments

The authors would like to acknowledge their colleagues: Professor D. P. Uskokovic (Institute of Technical Sciences of the Serbian Academy of Sciences and Arts, Belgrade, Serbia), Brazilian Ph.D. student Rodrigo Sabadini, Professor F. Kajzar (Université d'Angers, Institut des Sciences et Technologies Moléculaires, France), and Dr. V. I. Studeonov and Dr. P. Ya. Vasilyev (Vavilov State Optical Institute, St. Petersburg, Russia) for their help at the different steps and helpful discussion. Some parts of the results presented in the current paper have been discussed at the scientific seminar, Czestochowa University (December 12, 2012, Poland), at ICBB'14 Conference, in Gdansk Polytechnic University (May 14–17, 2014, Poland), and at the Nanotechnology Session in the framework of the MMT-2014 Conference (July 28–August 1, 2014, Ariel, Israel). The presented results are partially supported by Russian Foundation for Basic Research Fund, Grant no. 13-03-00044 (2013–2015) as well as by the FP7 Program, Marie Curie International Researchers Exchange Proposal “BIOMOLEC” (2011–2015).

References

- [1] K. Hosoda, R. Tada, M. Ishikawa, and K. Yoshino, “Effect of C₆₀ doping on electrical and optical properties of poly[(disilanyl)ene-oligophenylenes],” *Japanese Journal of Applied Physics*, vol. 36, no. 3B, part 2, pp. L372–L375, 1997.
- [2] W. Lee and H.-C. Chen, “Diffraction efficiency of a holographic grating in a liquid-crystal cell composed of asymmetrically patterned electrodes,” *Nanotechnology*, vol. 14, no. 9, pp. 987–990, 2003.
- [3] I. C. Khoo, A. Diaz, D. Kwon et al., “Nonlinear and electro-optics of nano-dispersed nematic liquid crystals with tunable negative-, zero-, and positive indices,” *Journal of Nonlinear Optical Physics & Materials*, vol. 16, no. 3, pp. 381–399, 2007.
- [4] A. D. Grishina, L. Licea-Jimenez, L. Y. Pereshivko et al., “Infrared photorefractive composites based on polyvinylcarbazole and carbon nanotubes,” *High Energy Chemistry*, vol. 40, no. 5, pp. 341–347, 2006.
- [5] Q. Peng, A. K. Dearden, J. Crean et al., “New materials graphyne, graphdiyne, graphone, and graphane: review of properties, synthesis, and application in nanotechnology,” *Nanotechnology, Science and Applications*, vol. 7, no. 2, pp. 1–29, 2014.
- [6] D. S. Chemla and J. Zyss, Eds., *Nonlinear Optical Properties of Organic Molecules and Crystals*, vol. 2, Academic Press, Orlando, Fla, USA, 1987, (Translated into Russian).
- [7] S. A. Akhmanov and S. Y. Nikitin, *Physical Optics*, Oxford University Press, Oxford, UK, 1997.
- [8] N. V. Kamanina, “Fullerene-dispersed nematic liquid crystal structures: dynamic characteristics and self-organization processes,” *Physics-Uspokhi*, vol. 48, no. 4, pp. 419–427, 2005.
- [9] N. V. Kamanina and D. P. Uskokovic, “Refractive index of organic systems doped with nano-objects,” *Materials and Manufacturing Processes*, vol. 23, no. 6, pp. 552–556, 2008.
- [10] N. V. Kamanina, A. Emandi, F. Kajzar, and A.-J. Attias, “Laser-induced change in the refractive index in the systems based on nanostructured polyimide: comparative study with other photosensitive structures,” *Molecular Crystals and Liquid Crystals*, vol. 486, pp. 1–11, 2008.
- [11] N. V. Kamanina, S. V. Serov, N. A. Shurpo et al., “Polyimide-fullerene nanostructured materials for nonlinear optics and solar energy applications,” *Journal of Materials Science: Materials in Electronics*, vol. 23, no. 8, pp. 1538–1542, 2012.
- [12] N. V. Kamanina, *Features of Optical Materials Modified with Effective Nanoobjects: Bulk Properties and Interface*, Nova Science Publishers, Novinka, New York, NY, USA, 2014.
- [13] N. V. Kamanina and N. A. Vasilenko, “Influence of operating conditions and interface properties on dynamic characteristics of liquid-crystal spatial light modulators,” *Optical and Quantum Electronics*, vol. 29, no. 1, pp. 1–9, 1997.

Research Article

Sustainable Nanopozzolan Modified Cement: Characterizations and Morphology of Calcium Silicate Hydrate during Hydration

N. Mohamed Sutan,¹ I. Yakub,¹ M. S. Jaafar,² K. A. Matori,² and S. K. Sahari¹

¹Department of Civil Engineering, Department of Chemical Engineering and Energy Sustainability, and Department of Electrical and Electronic Engineering, Faculty of Engineering, Universiti Malaysia Sarawak, Sarawak 94300, Malaysia

²Department of Civil Engineering, Faculty of Engineering, and Department of Physics, Faculty of Science, Universiti Putra Malaysia, Selangor 43400, Malaysia

Correspondence should be addressed to N. Mohamed Sutan; msnorsuzailina@feng.unimas.my

Received 17 December 2014; Revised 2 March 2015; Accepted 5 March 2015

Academic Editor: Anmin Zheng

Copyright © 2015 N. Mohamed Sutan et al. This is an open access article distributed under the Creative Commons Attribution License, which permits unrestricted use, distribution, and reproduction in any medium, provided the original work is properly cited.

There are environmental and sustainable benefits of partially replacing cement with industrial by-products or synthetic materials in cement based products. Since microstructural behaviours of cement based products are the crucial parameters that govern their sustainability and durability, this study investigates the microstructural comparison between two different types of cement replacements as nanopozzolan modified cement (NPMC) in cement based product by focusing on the evidence of pozzolanic reactivity in corroboration with physical and mechanical properties. Characterization and morphology techniques using X-ray diffraction (XRD), Fourier transform infrared spectroscopy (FTIR), energy-dispersive X-ray spectroscopy (EDS), and scanning electron microscopy (SEM) were carried out to assess the pozzolanic reactivity of cement paste modified with the combination of nano- and micro silica as NPMC in comparison to unmodified cement paste (UCP) of 0.5 water to cement ratio (w/c). Results were then substantiated with compressive strength (CS) results as mechanical property. Results of this study showed clear evidence of pozzolanicity for all samples with varying reactivity with NPMC being the most reactive.

1. Introduction

As the fourth largest consumer amongst Southeast Asia's countries, Malaysia consumed 17 million tons of cement by the end of 2011 [1]. With the high demand, large scale production is needed for its satisfaction that consequently releases more carbon dioxide (CO₂) that causes greenhouse effects. Cement replacement for cement based materials is one of the options to meet the increasing sustainability, green technology demands, and requirement in construction industry since it offers two distinct benefits to the environment: it significantly reduces the amount of CO₂ released into the atmosphere and minimizes massive landfill disposal. Therefore interest in cement research is moving towards finding viable whole or partial cement replacement like using industrial wastes such as microsilica (MS) and nanoscale materials such as nanosilica (NS). In addition, recently, research and development (R&D) on cement based

material is of interest to find new cement supplementary materials in nanoscale. For Malaysia, nanotechnology R&D was started by the government in 2001 and categorized as a strategic research (SR) program under IRPA in the Eighth Malaysia Plan (8MP) which spans from 2001 to 2005 and funded by the MOSTI [2].

MS and NS have one thing in common which is that they possess a pozzolanic characteristic. Pozzolanic materials have the high potential to be a substance to replace cement due to beneficial pozzolanic reaction that can improve cement based product properties. As generally known, calcium hydroxide (CH) or portlandite produced from the hydration process of cement will react with siliceous pozzolanic material to produce more C-S-H which is the substance that mainly contributes to strength for cement based material that can improve physical and mechanical properties such as reducing porosity and permeability. Hence, cement blended with pozzolanic material will have better strength and durability [3].

TABLE 1: Chemical and mineralogical composition of OPC.

| Component, % | CaO | SiO ₂ | Al ₂ O ₃ | Fe ₂ O ₃ | SO ₃ | MgO | Na ₂ O | K ₂ O | Others | LOI |
|--------------|------|------------------|--------------------------------|--------------------------------|-----------------|------|-------------------|------------------|--------|------|
| OPC | 63.0 | 21.69 | 5.75 | 3.25 | 2.35 | 1.97 | 0.50 | 0.28 | 0.11 | 1.00 |

Previous studies have shown that MS modified concrete was stronger and more durable compared to conventional concrete. Due to its high pozzolanicity, MS has a very high content of amorphous silicon dioxide (SiO₂) and very fine spherical particles sizes which are the main reasons for its high pozzolanic activity [4]. The rate of the pozzolanic activity is related to the surface area of pozzolan particles whereby the higher the surface area of pozzolan particle is or the finer the particle is, the more reactive it would be [5]. Hence, the research and development for cement based material is of interest to find new cement supplementary material which has a particle size of nanoscale (10⁻⁹ m). Incorporation of nanomaterials in cement and concrete production can lead to major improvement in the civil infrastructure because durability and sustainability of cement based product are determined by its microstructural mass transfer in nanoscale [6].

Previous studies have shown that MS modified concrete was stronger and more durable compared to conventional concrete. Due to its high pozzolanicity, MS has a very high content of amorphous silicon dioxide (SiO₂) and very fine spherical particles sizes which are the main reasons for its high pozzolanic activity [4]. Meanwhile NS is a new pozzolanic material that contains high percentage of silica with up to 99% purities and with small particle size in nanometer range. It is expected to have better performance due to the small particle size and high content of silica components [7–11]. Besides that, NS also acts as nuclei for cement phase and promotes cement hydration with its high pozzolanic reactivity, as nanoreinforcement and filler densifying the microstructure, leading to reducing porosity from a more compact and denser microstructure [12].

However there are no comparative studies on the potential performance of combination of MS and NS pozzolanic materials used as nanopozzolan modified cement (NPMC) in cement based products. Hypothetically, NPMC will produce a higher performance cement based product in terms of strength and durability due to their fineness and highly reactive pozzolanic properties. This study is an attempt to explore in that direction. Pozzolanic reactivity of MS, NS, and NPMC pastes was investigated and compared to unmodified cement paste (UCP). The efforts to investigate the potential usage of such nonconventional material which is typically of local or regional origin in cement based products will get a boost if there are systematic and comprehensive studies to quantify and characterize the performance of cement based products containing such materials and will contribute positively to waste management challenge.

2. Materials and Methods

2.1. Materials. Waste material and nanomaterial used as cement replacements in nanopozzolan modified cement

(NPMC) were microsilica from Grace Construction Sdn. Bhd. with 94.5% SiO₂ and Sigma-Aldrich silicon dioxide nanopowder (CAS 7631-86-9) of 10–20 nm particle size (BET) with 99.5% SiO₂. Cement used was ordinary Portland cement (OPC) (ASTM Type 1 recognized by ASTM C150) manufactured by Cahaya Mata Sarawak Cement Sdn. Bhd. (CMS) and it exceeds the quality requirements specified in the Malaysian Standard MS 522: Part 1: 1989 Specifications for OPC. The chemical composition of the OPC is given in Table 1.

2.2. Sample Preparation, Characterization by Using XRD, FTIR, and EDS, and Morphology Using SEM Techniques. The mix proportion for cement paste was set at 0.5 water to cement ratio (w/c) for all specimens that were casted into Universal Container 30 mL, diameter 28 × 85 mm for XRD, EDS, and SEM. All specimens were cured in the concrete laboratory at Universiti Malaysia Sarawak at daily room temperature (*T*) and relative humidity (RH) in the range of 18–28°C and 65–90%, respectively. The fine powder (passing 75 μm) and polished small samples were prepared and analysed using XRD, FTIR, EDS, and SEM on day 28. Ethanol was used to discontinue the hydration process of these samples. XRD analysis for all prepared samples was performed using PANalytical equipment with CuKα radiation and λ of 0.1546 nm. The specifications were count step: 4 sec/step, step size: 0.02 degrees, and range: 5–65 2θ. Shimadzu Fourier Transform Infrared Spectroscopy (FTIR) 81001 Spectrophotometer was used to perform the FTIR analysis. The spectrum measurement method applied was attenuated total reflection (ATR) method. Transmission infrared spectrum of each sample was recorded using a Fourier transform infrared spectrophotometer (IR Affinity-1) in the region of 400 to 4000 cm⁻¹ with 2.0 cm⁻¹ resolution. The samples were scanned 20 times. SEM images and EDS analysis for all prepared small polished samples were captured by scanning electron microscope and energy-dispersive X-ray spectroscopy (JSM-6701F) supplied by JEOL Company Limited, Japan, which followed the ASTM C 1723-10 (2010) code of practice.

2.3. Sample Preparation and Mechanical Test. The mix proportion mortar was set at (cement:sand:water) 1:1.67:0.5 (w/c) for all specimens that were casted into 150 mm cubes for compressive strength (CS) tests. All specimens were cured in the Concrete Laboratory at Universiti Malaysia Sarawak for 7, 14, and 28 days. CS test was performed according to BS 1881-116 (1983) on 150 mm cubes samples. It was used to determine the maximum compressive load that a sample can carry per unit area. Compressive strength test was performed to determine the maximum compressive load that the sample can carry

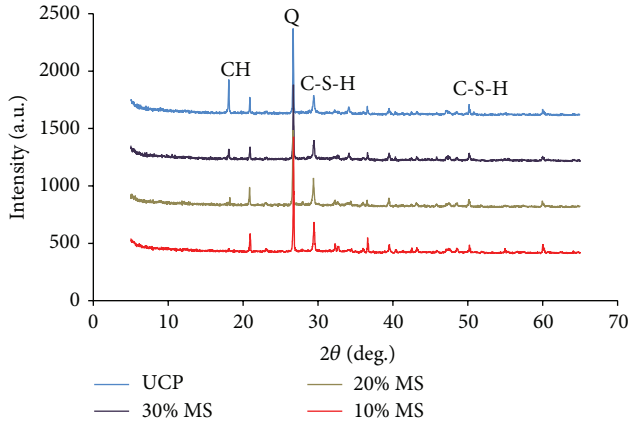


FIGURE 1: XRD pattern (CuK α radiation) for UCP and MS samples on day 28.

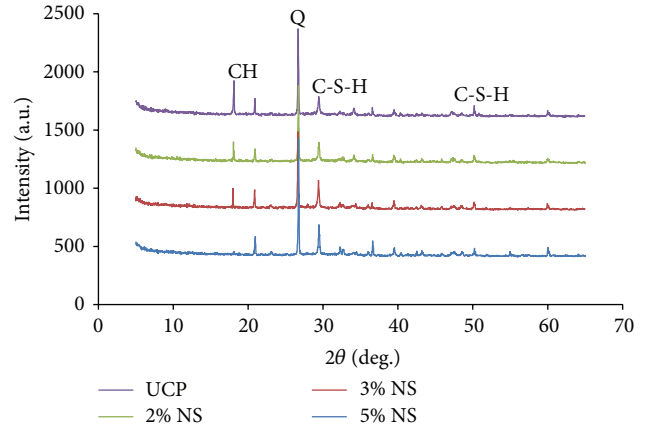


FIGURE 2: XRD pattern (CuK α radiation) of UCP and NS samples on day 28.

per unit area. The compressive strength is measured by using

$$\text{compressive strength} = \frac{\text{maximum load applied (N)}}{\text{cross-sectional area (mm}^2\text{)}}. \quad (1)$$

3. Results and Discussions

3.1. Identification of CH and C-S-H as Pozzolanic Reaction Indication

3.1.1. X-Ray Diffraction (XRD). The X-ray diffraction (XRD) patterns of UCP, 10% MS, 20% MS, and 30% MS on day 28 are given in Figure 1. It can be observed that crystalline CH (portlandite) appeared in all samples except for 30% MS sample at peaks around 18.07, 34.17, and 47.19 2θ while amorphous C-S-H was hardly visible but can be seen at peak around 29.54 and 50.0 2θ [13–16]. As for C-S-H, the intensity increased the most for 10% MS followed by 20% MS, UCP, and 30% MS showing that portlandite is consumed due to pozzolanic reaction with SiO₂ producing more C-S-H.

Figure 2 shows XRD patterns for UCP, 2% NS, 3% NS, and 5% NS on day 28. Portlandite was detected in all samples at peaks around 18.07, 34.17, and 47.19 2θ . We can observe the onset of semicrystalline Al-CSH at 29.5 and 49.5 2θ [13–15]. In the same figure, significant intensity of C-S-H can be found on sample 5% NS [13].

Based on the results, it can be concluded that the optimum dosage for MS and NS as cement replacement in cement paste is 10% and 5%, respectively. This is due to the highest intensity in C-S-H from the XRD characterization in both samples that indicated that more C-S-H were produced by pozzolanic reaction of 10% MS and 5% NS as cement replacement. Therefore NPMC of the combination of 10% MS and 5% NS was used and pozzolanic reactivity of the sample was characterized using FTIR, EDS, and SEM and further corroborated with compressive strength results.

3.1.2. Fourier Transform Infrared Spectroscopy (FTIR). Figure 3 shows that FTIR analysis focusing on pozzolanic

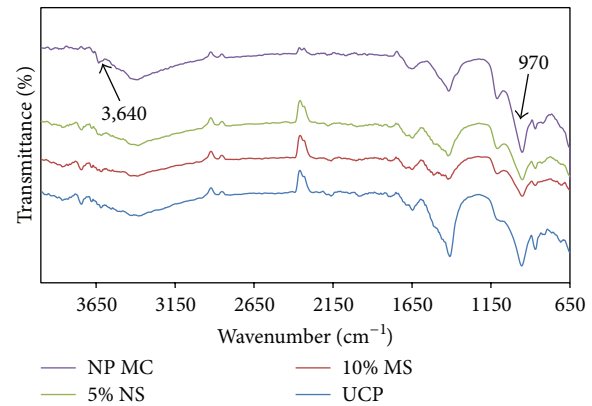


FIGURE 3: FTIR spectra for NPMC, 5% NS, 10% MS, and UCP on day 28.

activity was made on NPMC sample in comparison to 5% NS, 10% MS, and UCP samples. The evidence of pozzolanic activity can be found by comparing the intensity of CH and C-S-H band on day 28. The infrared spectrum wave number of CH and C-S-H is 3,640 cm^{-1} and 970 cm^{-1} , respectively [15, 16]. Figure 3 shows (a) CH and (b) C-S-H band for all samples. The sharpness of the spectrum's curve indicates the intensity of the substance. It can be clearly seen that C-S-H peaks are the strongest for NPMC which confirm and substantiate the results from XRD characterization.

3.1.3. Energy-Dispersive X-Ray Spectroscopy (EDS). Ca/Si and Si/Ca ratios obtained from EDS spectra were valid as the indication of the presence of CH and C-S-H. The presence of C-S-H reflected in Ca/Si ratio. The Ca/Si and Si/Ca ratios for NPMC, 5% NS, 10% MS, and UCP samples on day 28 were calculated from EDS spectra and are shown in Table 2. Results indicate the presence of C-S-H and CH for all samples which corroborate XRD characterization results in previous sections. From a compositional point of view, C-S-H gel is often characterized by its Ca/Si ratio, which typically ranges from 0.7 to 2.3 [17]. But the typical Ca/Si ratio of C-S-H

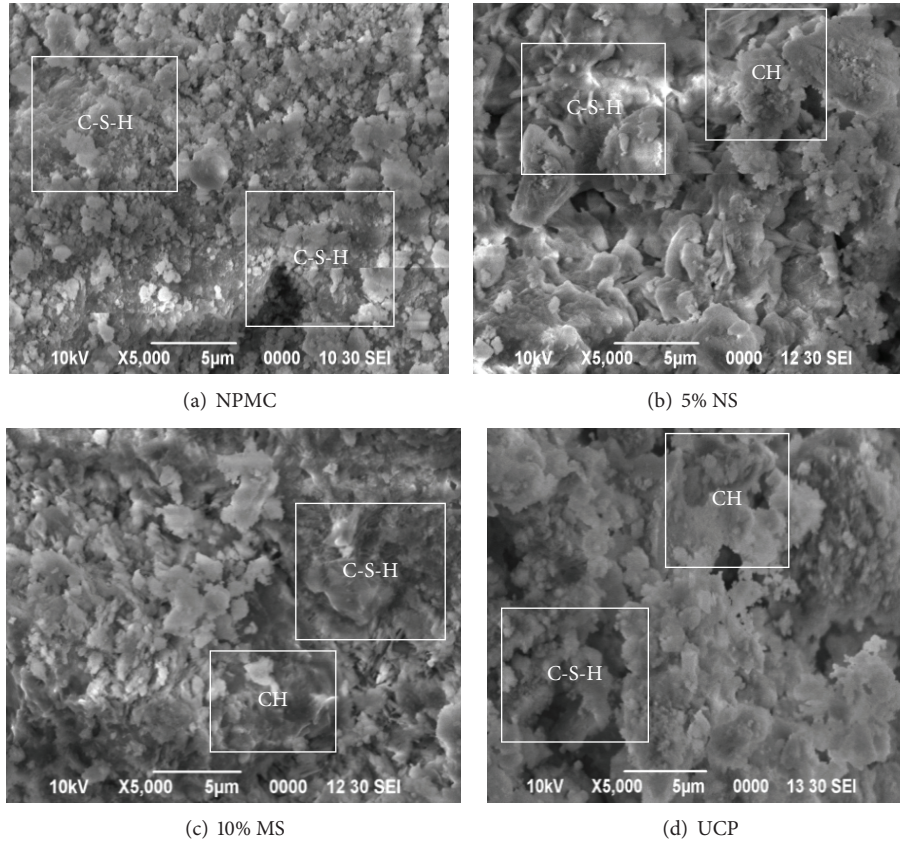


FIGURE 4: SEM images of (a) NPMC, (b) 5% NS, (c) 10% MS, and (d) UCP samples on day 28.

TABLE 2: Ca/Si and Si/Ca ratios obtained from EDS spectra.

| Samples | NPMC | 5% NS | 10% MS | UCP |
|---------|------|-------|--------|------|
| Ca/Si | 0.28 | 2.76 | 1.37 | 3.51 |
| Si/Ca | 3.57 | 0.36 | 0.73 | 0.28 |

in OPC is about 1.5–1.8, but reduced ratios are observed when pozzolans are used [16]. The surface charge on C-S-H depends on its Ca/Si ratio: when the Ca/Si ratio is high, the surface charge of C-S-H is positive and anions are adsorbed on the C-S-H fibers (but not cations as Na^+ and K^+ , which remain in the pore solution); when the Ca/Si ratio is lower than about 1.2–1.3, the surface charge of C-S-H becomes negative and alkali cations are incorporated on the C-S-H [17–19]. The Si/Ca ratio is somewhat variable but typically approximately 0.45–0.50 in hydrated Portland cement but up to perhaps about 0.6 if slag, fly ash, or microsilica is present, depending on the proportions. CH is formed mainly from alite hydration [17]. Since alite has a Ca/Si ratio of 3 to 1 and C-S-H has a Ca/Si ratio of approximately 1.5–1.8 to 1, therefore CH is produced from the additional CaO. Results clearly show the evidence of C-S-H and CH for all samples which complemented FTIR results.

3.1.4. Scanning Electron Microscope (SEM). Scanning electron microscope (SEM) morphological analysis was used to

further corroborate and substantiate the results from XRD and EDS. Since CH and C-S-H are the components of pozzolanic reaction, SEM images shown in Figure 4 focus on the presence of CH and C-S-H in the three critical samples mentioned previously. From SEM images CH crystals solid hexagonal platelike morphology and abundant presence of C-S-H flowery-like morphology are found in the sample as it is the by-product from the cement hydration [5]. It is also observed in Figure 4(a) that evidence of pozzolanic interaction between CH and NPMC produces abundant presence of C-S-H flowery-like morphology. On the other hand the presence of unreacted CH manifested in Figures 4(b), 4(c), and 4(d) indicates lesser pozzolanic interaction. These results correlated with XRD, EDS, and previous studies that confirmed the improvement of mortar that contains MS and NS manifested in reduced porosity and increased durability. The microstructural improvement contributes to the densification of interfacial transition zone and lesser porosity of the matrix is due to the consumption of and the reduction in the amount of CH due to pozzolanic reaction by MS and NS particles to form C-S-H as additional cementitious material [20].

3.2. Mechanical Property

3.2.1. Compressive Strength Test. Figure 5 illustrates the compressive strength results for NPMC, 5% NS, and 10% MS

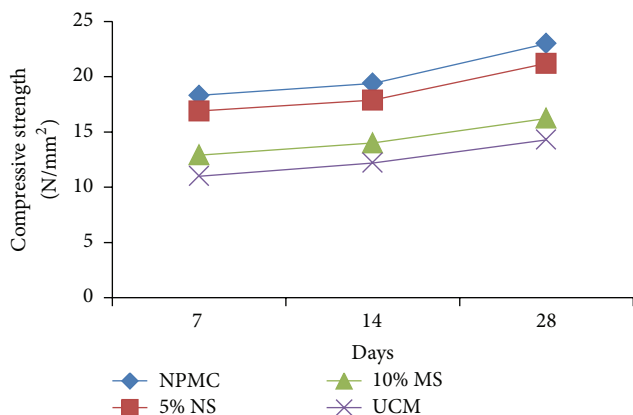


FIGURE 5: Compressive strength for NPMC, NS, MS, and UCM samples.

samples in comparison to UCM sample as a function of hydration time. All mortar samples show the normal trend for hydrating mortar [5]. NPMC has improved UCM compressive strength by 60.84%. Meanwhile, 5% NS and 10% MS have 48.3% and 13.45% of UCM strength, respectively. NPMC has the highest strength among all samples on day 28. This improvement is due to the amplified pozzolanic reactivity of both NS and MS that produce extra C-S-H gel that makes finer hydrated phases and densified microstructure matrix that compensates the agglomeration effect of MS [4–6, 8]. These effects may enhance the durability of concrete elements and structures. Results confirmed the findings from XRD, FTIR, EDS, and SEM by displaying the highest compressive strengths of NPMC sample.

4. Conclusion

It can be concluded that the optimum dosage for MS and NS as cement replacement in cement paste is 10% and 5%, respectively. This is due to the highest intensity in C-S-H from the XRD characterization in both samples which indicated that more C-S-H gel was produced by the addition of 10% MS and 5% NS. FTIR and EDS analysis on NPMC sample showed evidence of NS-MS interaction with the evidence of decrease in CH and increase in C-S-H indicated by Si/Ca and Ca/Si ratios. Furthermore, morphology from SEM images also reveals the same evidence of the combinative effects of MS and NS. The mechanical properties of NPMC in terms of compressive strength were improved by 60.8% that substantiated XRD characterization, FTIR analysis, EDS analysis, and SEM morphology results. The results in this study indicate the possibility of using NS to further improve MS modified mortar and cement based product properties. Further in-depth analysis and understanding on the behaviour of NPMC by using other characterization techniques are needed.

Conflict of Interests

The authors declare that there is no conflict of interests regarding the publication of this paper.

Acknowledgments

The authors wish to acknowledge the Ministry of Education and University Malaysia Sarawak for supporting this work under ERGS/TK04(02)/1011/2013(08) and RACE/c(1)/1108/2013(16) Grants.

References

- [1] *Research and Markets: Malaysia Cement Industry*, 2012, <http://www.businesswire.com/news/home/20120809005630/en/Research-Markets-Malaysia-Cement-Industry-1H12>.
- [2] U. Hashim, E. Nadia, and S. Salleh, “Nano technology development status in malaysia: industrialization strategy and practices,” *International Journal of Nanoelectronic and Material*, vol. 2, no. 1, pp. 119–134, 2009.
- [3] J. M. R. Dotto, A. G. de Abreu, D. C. C. dal Molin, and I. L. Müller, “Influence of silica fume addition on concretes physical properties and on corrosion behaviour of reinforcement bars,” *Cement & Concrete Composites*, vol. 26, no. 1, pp. 31–39, 2004.
- [4] A. Behnood and H. Ziari, “Effects of silica fume addition and water to cement ratio on the properties of high-strength concrete after exposure to high temperatures,” *Cement & Concrete Composites*, vol. 30, no. 2, pp. 106–112, 2008.
- [5] V. M. Malhotra and P. K. Mehta, *Pozzolanic and Cementitious Materials, Advances in Concrete Technology*, Taylor & Francis, London, UK, 2004.
- [6] L. Raki, J. Beaudoin, R. Alizadeh, J. Makar, and T. Sato, “Cement and concrete nanoscience and nanotechnology,” *Materials*, vol. 3, no. 2, pp. 918–942, 2010.
- [7] R. Olar, *Nanomaterials and Nanotechnologies for Civil Engineering*, Din Iaștomul Liv (Lviii), Fasc. 4, Buletinul Institutului Politehnic Din Iași Publicat De Universitatea Tehnică “Gheorghe Asachi”, Iași, Romania, 2011.
- [8] G. Quercia and H. J. H. Brouwers, “Application of nano-silica (nS) in concrete mixtures,” in *Proceedings of the 8th FIB PhD Symposium in Kgs, Lyngby*, Denmark, June 2010.
- [9] K. Sobolev, I. Flores, R. Hermosillo, and L. M. Torres-Martinez, “Nanomaterials and nanotechnology for high-performance cement composites,” *ACI Materials Journal*, vol. 254, pp. 93–120, 2008, SP-254-8.
- [10] K. Sobolev and M. F. Gutierrez, *How Nanotechnology Can Change the Concrete World, Part I and II*, American Ceramic Society Bulletin, 2005.
- [11] K. Sobolev and S. P. Shah, *Nanotechnology of Concrete: Recent Developments and Future Perspectives*, American Concrete Institute (ACI), Farmington Hills, Mich, USA, 2008.
- [12] K. Sobolev, I. Flores, L. M. Torres-Martinez, P. L. Valdez, E. Zarazua, and E. L. Cuellar, “Engineering of SiO₂ nanoparticles for optimal performance in nano cement-based materials,” in *Nanotechnology in Construction 3: Proceedings of the NICOM3*, pp. 139–148, Springer, Berlin, Germany, 2009.
- [13] J. R. Houston, R. S. Maxwell, and S. A. Carroll, “Transformation of meta-stable calcium silicate hydrates to tobermorite: reaction kinetics and molecular structure from XRD and NMR spectroscopy,” *Geochemical Transactions*, vol. 10, article 1, pp. 1–14, 2009.
- [14] P. Barnes and J. Bensted, *Structure and Performance of Cements*, Taylor & Francis, New York, NY, USA, 2008.
- [15] F. S. Shirazi, M. Mehrali, A. A. Oshkour, H. S. C. Metselaar, N. A. Kadri, and N. A. Abu Osman, “Mechanical and physical

- properties of calcium silicate/alumina composite for biomedical engineering applications,” *Journal of the Mechanical Behavior of Biomedical Materials*, vol. 30, pp. 168–175, 2014.
- [16] F. S. Shirazi, E. Moghaddam, M. Mehrli et al., “*In vitro* characterization and mechanical properties of β -calcium silicate/POC composite as a bone fixation device,” *Journal of Biomedical Materials Research Part A*, vol. 102, no. 11, pp. 3973–3985, 2014.
- [17] J. J. Chen, J. J. Thomas, H. F. W. Taylor, and H. M. Jennings, “Solubility and structure of calcium silicate hydrate,” *Cement and Concrete Research*, vol. 34, no. 9, pp. 1499–1519, 2004.
- [18] E. Traversa, *Nanotechnology (General)—216th ECS Meeting*, vol. 25, The Electrochemical Society, 2010.
- [19] H. A. Toutanji and T. El-Korchi, “The influence of silica fume on the compressive strength of cement paste and mortar,” *Cement and Concrete Research*, vol. 25, no. 7, pp. 1591–1602, 1995.
- [20] G. Quercia, G. Hüsken, and H. J. H. Brouwers, “Water demand of amorphous nano silica and its impact on the workability of cement paste,” *Cement and Concrete Research*, vol. 42, no. 2, pp. 344–357, 2012.

Research Article

Study of the Plasmon Energy Transfer Processes in Dye Sensitized Solar Cells

Tzu-ming Chien,¹ Prathamesh Pavaskar,² Wei Hsuan Hung,¹ Stephen Cronin,² Sheing-Hui Chiu,¹ and Sz-Nian Lai¹

¹Department of Materials Science and Engineering, Feng Chia University, Taichung 407, Taiwan

²Department of Electrical Engineering, University of Southern California, Los Angeles, CA 90089, USA

Correspondence should be addressed to Wei Hsuan Hung; whung@fcu.edu.tw

Received 20 November 2014; Accepted 28 January 2015

Academic Editor: Bin Zhang

Copyright © 2015 Tzu-ming Chien et al. This is an open access article distributed under the Creative Commons Attribution License, which permits unrestricted use, distribution, and reproduction in any medium, provided the original work is properly cited.

We report plasmon enhanced absorption in dye sensitized solar cells (DSSC) over a broad wavelength range. 45% enhancement in the power conversion efficiency is observed with the inclusion of plasmonic gold nanoparticles (NPs). Photocurrent spectra show enhancement over the entire dye absorption range from 450 nm to 700 nm, as well as in the near infrared (NIR) region above 700 nm due to the strong plasmon-induced electric fields produced by the gold NPs. The plasmon-induced electric field distribution of the island-like gold film is also investigated using finite-difference-time-domain (FDTD) calculations. Furthermore, photoluminescence spectra are performed in order to rule out the mechanism of plasmon energy transfer through Forster resonance energy transfer.

1. Introduction

Dye-sensitized solar cells (DSSCs) have gained much attention because of their promising power conversion efficiency and low fabrication cost. However, after the initial efficiency of 11% was reported in the mid-1990s [1, 2], further improvement in cell performance has been slow, and the efficiency has remained considerably lower than theoretical maximum values [3, 4]. Solar energy conversion consists of four basic processes: light absorption, exciton separation, carrier transportation, and collection. Several studies have investigated these four steps to improve cell performance, employing approaches such as increased molecular adsorption [5], broad spectrum absorption [6], and multiple exciton generation by a single photon [7, 8]. As an alternative to modifying the absorbing dye molecule, plasmonic metal nanoparticles, which have strong surface plasmon resonance, can be integrated to improve light harvesting. In surface plasmon resonance, the collective oscillation of free electrons confined at the surface of metals can be induced when the frequency of incident light matches the plasmon frequency of

irradiated metals [9–11]. These collective charge oscillations result in substantially enhanced electric fields near the surface of NPs, which can facilitate both light absorption and charge separation [12].

Plasmonic enhancement has been used in inorganic and organic thin-film solar cells [13–16] to increase the effective light absorption of host materials. Several methods have been developed for integrating plasmonic NPs into solar cells. For example, plasmonic nanostructures have been patterned on indium tin oxide (ITO) by applying electron beam lithography, which provides high controllability of nanostructures in shape, size, and separation [17], and nanoparticles have been blended within organic bulk heterojunction solar cells during active layer material synthesis [18, 19]. However, electron beam lithography is still not considered practical for large-scale fabrication, and the blending method poses problems of solubility and nonuniform distribution. Therefore, researchers are still searching for a simple and effective approach to incorporating plasmonic nanostructures into solar cells.

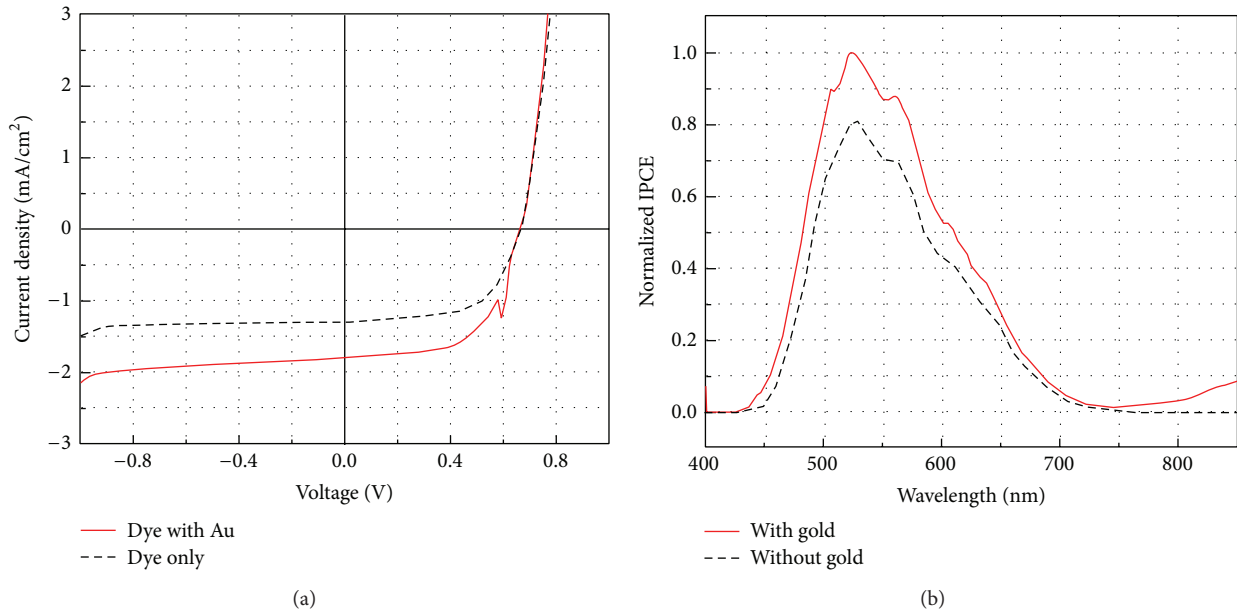


FIGURE 1: (a) J - V characteristics of dye sensitized solar cells and (b) normalized incident photon-to-current conversion efficiency spectra with and without island-like gold nanostructures.

This paper proposes a simple and rapid method for fabricating plasmonic DSSCs. In this study, plasmonic NPs were produced using electron beam evaporation of a 5 nm gold (Au) film on the surface of a dye-loaded TiO₂ electrode. Because 5 nm is not a sufficient thickness for forming a continuous Au film, the film forms island-like nanostructures with few-nanometer separation. Strong electric fields within nanogaps between the island structures are referred to as hot spots. In addition to the J - V characterization of DSSCs, the spectral response of the photocurrent is a measure for determining the enhanced region of absorption. Furthermore, FDTD simulations were conducted to investigate the distribution of plasmon-enhanced electric fields in the island-like nanostructures. Finally, the plasmonic energy transfer mechanism was examined using photoluminescence spectroscopy.

In this study, anodic TiO₂ (ATO) was prepared using electrochemically oxidizing titanium foils in an ethylene glycol electrolyte containing 0.25 wt% NH₄F and 2 wt% H₂O with an anodization potential of 30 V applied for 1 h [20, 21]. Crystalline TiO₂ can be achieved by performing an annealing treatment at 450°C for 5 h after anodization. Raman spectra were recorded after the annealing process and revealed the formation of anatase crystalline phase TiO₂. Ruthenium-based dye (N719) (Sigma-Aldrich, Inc.) was used as a sensitizer in the solar device. The dye-loading process was completed by soaking the ATO anode in the N719 dye solution for 24 h and then rinsing it with isopropyl alcohol to remove the unattached dye on the surface of the ATO. A 5 nm plasmonic Au layer was deposited on the annealed TiO₂ after the dye-loading process by using electron-beam evaporation at a rate of 1 Å/s. The counter electrode consisted of ITO with an additional 1 nm layer of platinum (Pt) on the surface, which accelerated the charge transfer process in

the reduction of triiodide (I₃⁻) [22]. Finally, the dye-loaded TiO₂ electrode and Pt-coated ITO counter electrode were assembled into a sandwich-type cell by using a hot-melting seal foil at a thickness of 100 μm purchased from Solarnix, Inc.

2. Results and Discussion

The J - V characteristics of dye-sensitized cells with and without the incorporation of the plasmonic Au layer were measured using an AM 1.5 solar simulator equipped with a 450 W xenon lamp with a power output of 100 mW/cm² calibrated according to a reference silicon photodiode. Figure 1(a) shows a comparison of the photovoltaic measurement with and without island-like plasmonic nanostructures subjected to irradiation. The plasmon-enhanced cell exhibited an approximately 45% power conversion enhancement in the photocurrent (1.81 mA/cm²) relative to that of the control cell (1.25 mA/cm²) with a similar value of the open circuit voltage (V_{oc}) and fill factor (FF), as shown in Table 1.

Photocurrent spectra were measured with and without the 5 nm Au layer and plotted as a function of wavelength, as shown in Figure 1(b). The plasmon-enhanced cell exhibited an enhancement in photocurrent over the entire dye absorption range from 450 to 700 nm as well as the near-infrared tail above 700 nm, which was due to additional charges from the TiO₂ and was verified according to the absorption spectrum of the TiO₂. This broad-band enhancement of the photocurrent is derived from the strong plasmon-induced electric fields and light scattering around the metal nanostructures, which resulted in widely enhanced light absorption in the actively absorbing host materials. Although the enhancement factors (EFs) were large, the overall efficiency of the devices

TABLE 1: Summary characteristics of dye sensitized solar cell with and without plasmonic gold nanoparticles.

| | J_{sc} (mA/cm ²) | V_{oc} (V) | FF | Efficiency (%) | Enhancement (%) |
|--------|--------------------------------|--------------|------|----------------|-----------------|
| w/o Au | 1.28 | 0.67 | 0.61 | 0.52 | 45% |
| w/ Au | 1.81 | 0.66 | 0.62 | 0.74 | |

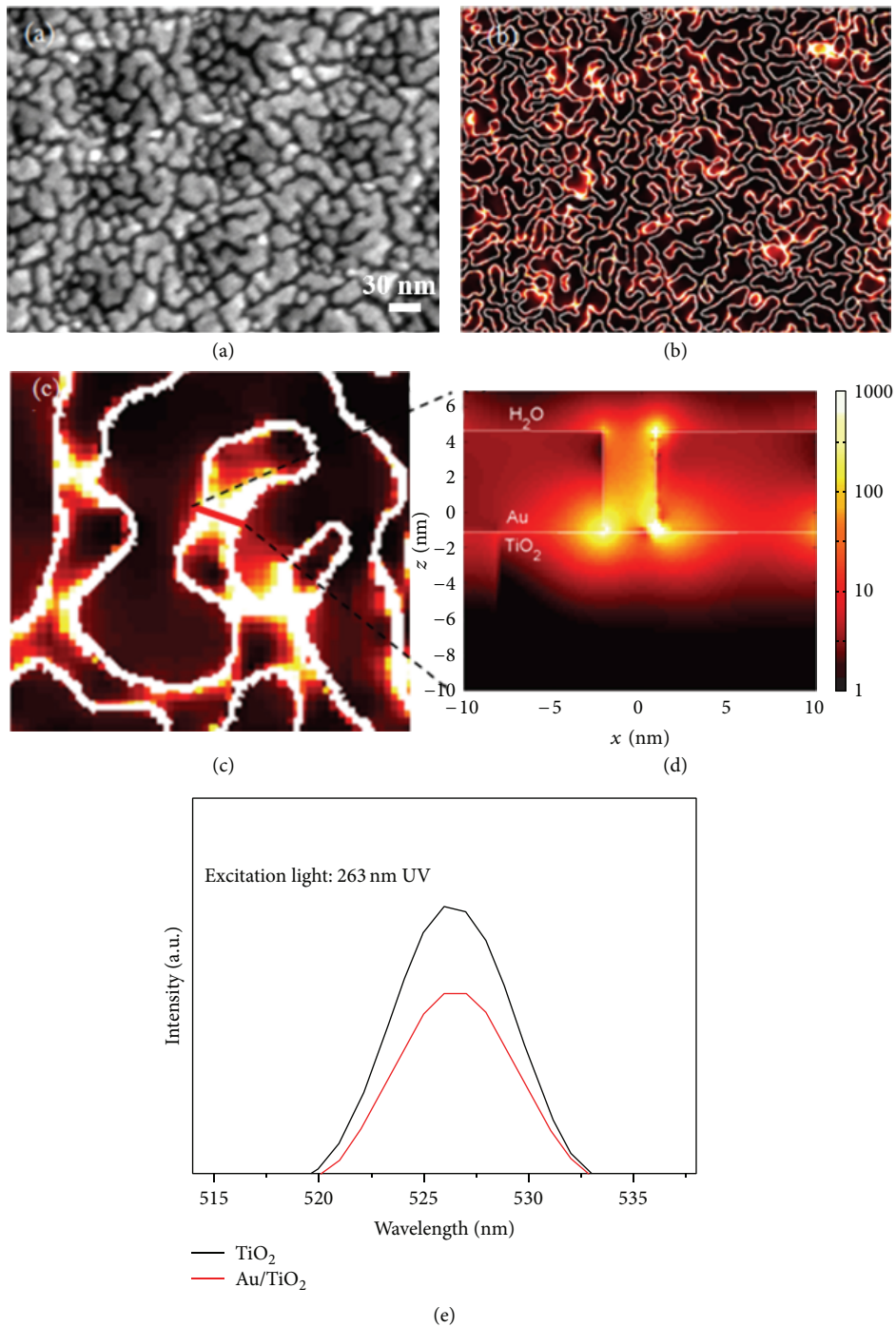


FIGURE 2: (a) SEM image of a 5 nm thick Au island film. (b–d) simulated electric field intensity observed from the top surface and cross section of the interface of Au–TiO₂ calculated using FDTD. (e) The Photoluminescence spectrum (PL) of TiO₂ (black) and Au–TiO₂ (red) under excitation wavelength ($\lambda = 263$ nm).

remained rather low because the samples had a considerably lower surface area compared with current state-of-the-art Gratzel cells. The absolute efficiency can be improved beyond this proof-of-principle study by using host materials with a large surface area, such as TiO_2 nanotubes, or nanowires to increase photon absorption sites.

To develop a comprehensive understanding of the plasmon-induced electric fields, we conducted FDTD simulations of the plasmon-induced electric distribution of the island-like Au film. Figures 2(b)–2(d) show the electromagnetic response of the Au island film, calculated using the FDTD method. We used the scanning electron microscope (SEM) image shown in Figure 2(a) to define the spatial extent of the Au islands in the simulation. Local hot spots were observed between nearly touching Au nanoparticles. Figure 2(d) shows a cross-sectional plot of the electric field distribution of one of these hot spot regions in the z -dimension. In this hot spot region, the electric field intensity at the TiO_2 surface reached 1000 times that of the incident electric field intensity, suggesting that the photon absorption (and hence electron-hole pairs generation) rate was 1000 times higher than that of the incident electromagnetic radiation.

We calculated the enhancement factor on the basis of the results of the FDTD simulation. Because the photon absorption rate is proportional to the electric field squared ($|E|^2$), we integrated $|E|^2$ over the whole film and divided it by the integral of the incident electromagnetic field squared ($|E_0|^2$) as follows:

$$EF = \frac{\int_{-10\text{nm}}^0 dz \int dx dy |E|^2}{\int_{-10\text{nm}}^0 dz \int dx dy |E_0|^2}. \quad (1)$$

In the z -dimension, we integrated only $|E|^2$ from the TiO_2 surface ($z = 0$) with that from one exciton diffusion length below the surface ($z = -10\text{nm}$). The value for the EF when $|E|^2$ was integrated over the entire simulation area ($400 \times 300\text{nm}$) is 12X. This EF value is higher than that observed in our experiment, most likely because of activity-absorbing N719 dye molecules inside the pores of the ATO structure, which are distant from the plasmonic Au film on the top surface of the ATO. In addition, this plasmon-enhanced absorption process competes with the recombination process because of the presence of metal nanoparticles as a recombination center, which was not considered in this FDTD simulation. However, this value is for a random distribution of Au islands that are not optimized geometrically. If we instead integrated $|E|^2$ over the area of only one hot spot, as shown in Figure 2(c), an EF of 190X would be yielded. The investigation of the charge transfer of photogenerated electron-hole pairs can be achieved using the photoluminescence (PL) emission spectrum, the signal of which indicates the recombination of free charge carriers. Figure 2(e) shows the PL spectra of different samples at an excitation wavelength of 263 nm (4.71 eV). According to the PL results, the intensity of emission peaks at approximately 525 nm decreased with the existence of Au NPs, and the weaker emission signal occurred in the Au/dye-loaded TiO_2 sample. These results suggested that the recombination of

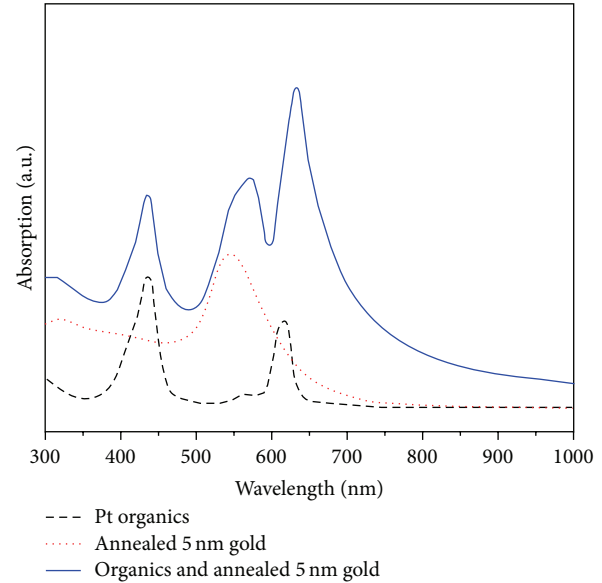


FIGURE 3: Absorption spectra of phosphorescence dye (black), 5 nm gold (red), and dye with 5 nm gold underneath (blue).

charge carriers was significantly reduced when Au NPs and dye-loaded TiO_2 were integrated.

Finally, photoluminescence spectroscopy is carried out in order to rule out the noncharge transfer mechanism of plasmonic energy. Forster transfer (i.e., radiative energy transfer) depends on the interaction of the resonant dipoles between plasmonic NPs and dye molecules. This noncharge transfer pathway can be examined by taking photoluminescence spectra of plasmonic nanoparticles with phosphorescent dye. It is important to choose the proper phosphorescent dye, which is energetically allowed to absorb the plasmon resonant energy from metal nanoparticles. Here, we performed photoexcitation measurements on samples made of sol-gel TiO_2 , rather than ATO, loaded with the phosphorescent dye and platinum tetra (1,3-di-tert-butylphenyl) tetrabenzoporphyrin (Pt tbu (TPBP)) both with and without 5 nm gold films. The purpose of using phosphorescence dye (TPBP) is to create a scenario of nonoverlap absorption spectrum of the phosphorescence dye and plasmonic resonant energy of gold, as shown in the UV-Vis absorption spectra in Figure 3. This nonoverlap of absorption enables us to investigate whether or not Forster energy transfer occurs between the plasmons in the metal NPs and the excitons in the phosphorescent dye. Figure 4 shows the phosphorescent emission of the TPBP dye at 760 nm as a function of the incident of scanning wavelengths with/without gold NPs. However, there is no pronounced peak observed at the plasmon resonant wavelength of 532 nm in Figure 4(b), which is the corresponding plasmon resonant energy of the 5 nm gold film. The absence of a peak at 532 nm in the excitation spectrum indicates that most of plasmon energy is not transferred to the phosphorescent dye for reradiation through the Forster resonance energy transfer mechanism. These results indicate that the improvement of cell performance originates from another path, which we

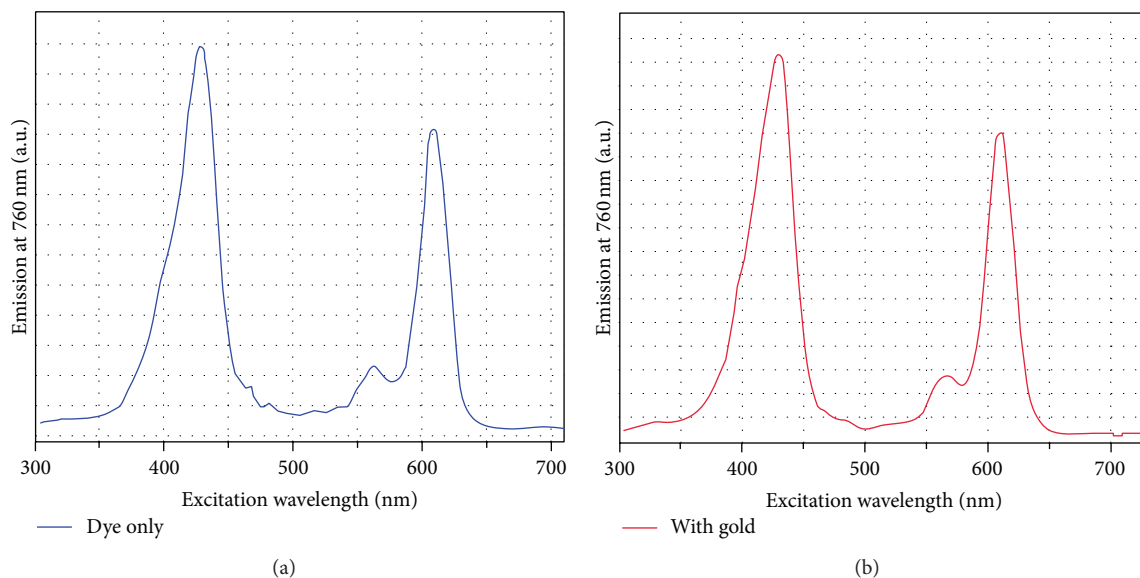


FIGURE 4: Emission spectra of (a) TPBP dye only and (b) TPBP dye with 5 nm gold film.

believe is due to the plasmon-induced electric field surrounding the plasmonic NPs.

In conclusion, we have successfully demonstrated plasmonic enhancement of dye sensitized solar cells with up to 45% improvement in the cell power conversion efficiency by simply integrating a layer of island-like plasmonic gold nanoparticles with an N719/TiO₂ DSSC. FDTD simulations are carried out in order to investigate the distribution of the plasmon-induced electric fields in the 5 nm island-like gold film. Furthermore, we believe the enhancement obtained in the dye sensitized cell is attributed to the plasmon-induced electric fields, which strongly increase the exciton generation rate. Photoluminescence spectroscopy rules out the mechanism of plasmon energy transfer through a Forster resonance energy transfer path.

Conflict of Interests

The authors state that there is no conflict of interests related to this paper.

References

- [1] B. O'Regan and M. Graetzel, "A Low-cost, high-efficiency solar-cell based on dye-sensitized colloidal TiO₂ films," *Nature*, vol. 353, no. 6346, pp. 737–740, 1991.
- [2] M. K. Nazeeruddin, F. de Angelis, S. Fantacci et al., "Combined experimental and DFT-TDDFT computational study of photoelectrochemical cell ruthenium sensitizers," *Journal of the American Chemical Society*, vol. 127, no. 48, pp. 16835–16847, 2005.
- [3] M. Grätzel, "Photoelectrochemical cells," *Nature*, vol. 414, no. 6861, pp. 338–344, 2001.
- [4] J. Nelson, *The Physics of Solar Cells*, Imperial College Press, London, UK, 2003.
- [5] K. Hara, T. Sato, R. Katoh et al., "Molecular design of coumarin dyes for efficient dye-sensitized solar cells," *The Journal of Physical Chemistry B*, vol. 107, no. 2, pp. 597–606, 2003.
- [6] S. M. Zakeeruddin, M. K. Nazeeruddin, P. Pechy et al., "Molecular engineering of photosensitizers for nanocrystalline solar cells: synthesis and characterization of Ru dyes based on phosphonated terpyridines," *Inorganic Chemistry*, vol. 36, no. 25, pp. 5937–5946, 1997.
- [7] R. J. Ellingson, M. C. Beard, J. C. Johnson et al., "Highly efficient multiple exciton generation in colloidal PbSe and PbS quantum dots," *Nano Letters*, vol. 5, no. 5, pp. 865–871, 2005.
- [8] R. D. Schaller, M. Sykora, J. M. Pietryga, and V. I. Klimov, "Seven excitons at a cost of one: redefining the limits for conversion efficiency of photons into charge carriers," *Nano Letters*, vol. 6, no. 3, pp. 424–429, 2006.
- [9] M. Moskovits, "Surface-enhanced spectroscopy," *Reviews of Modern Physics*, vol. 57, no. 3, pp. 783–826, 1985.
- [10] H. H. Wei, H. I-Kai, A. Bushmaker, R. Kumar, J. Theiss, and S. B. Cronin, "Laser directed growth of Carbon-Based nanostructures by plasmon resonant chemical vapor deposition," *Nano Letters*, vol. 8, no. 10, pp. 3278–3282, 2008.
- [11] W. H. Hung, M. Aykol, D. Valley, W. Hou, and S. B. Cronin, "Plasmon resonant enhancement of carbon monoxide catalysis," *Nano Letters*, vol. 10, no. 4, pp. 1314–1318, 2010.
- [12] X.-Y. Zhu, Q. Yang, and M. Muntwiler, "Charge-transfer excitons at organic semiconductor surfaces and interfaces," *Accounts of Chemical Research*, vol. 42, no. 11, pp. 1779–1787, 2009.
- [13] H. A. Atwater and A. Polman, "Plasmonics for improved photovoltaic devices," *Nature Materials*, vol. 9, no. 3, pp. 205–213, 2010.
- [14] J. H. Lee, J. H. Park, J. S. Kim, D. Y. Lee, and K. Cho, "High efficiency polymer solar cells with wet deposited plasmonic gold nanodots," *Organic Electronics*, vol. 10, no. 3, pp. 416–420, 2009.
- [15] B. P. Rand, P. Peumans, and S. R. Forrest, "Long-range absorption enhancement in organic tandem thin-film solar cells containing silver nanoclusters," *Journal of Applied Physics*, vol. 96, no. 12, pp. 7519–7526, 2004.

- [16] M. D. Brown, T. Suteewong, R. S. S. Kumar et al., "Plasmonic dye-sensitized solar cells using core-shell metal-insulator nanoparticles," *Nano Letters*, vol. 11, no. 2, pp. 438–445, 2011.
- [17] A. P. Kulkarni, K. M. Noone, K. Munechika, S. R. Guyer, and D. S. Ginger, "Plasmon-enhanced charge carrier generation in organic photovoltaic films using silver nanoprisms," *Nano Letters*, vol. 10, no. 4, pp. 1501–1505, 2010.
- [18] D. Duche, P. Torchio, L. Escoubas et al., "Improving light absorption in organic solar cells by plasmonic contribution," *Solar Energy Materials and Solar Cells*, vol. 93, no. 8, pp. 1377–1382, 2009.
- [19] A. J. Morfa, K. L. Rowlen, T. H. Reilly III, M. J. Romero, and J. van de Lagemaat, "Erratum: plasmon-enhanced solar energy conversion in organic bulk heterojunction photovoltaics [Appl. Phys. Lett. 92, 013504 (2008)]," *Applied Physics Letters*, vol. 92, no. 13, Article ID 139901, 2008.
- [20] C. A. Grimes, "Synthesis and application of highly ordered arrays of TiO₂ nanotubes," *Journal of Materials Chemistry*, vol. 17, no. 15, pp. 1451–1457, 2007.
- [21] Z. Liu, W. Hou, P. Pavaskar, M. Aykol, and S. B. Cronin, "Plasmon resonant enhancement of photocatalytic water splitting under visible illumination," *Nano Letters*, vol. 11, no. 3, pp. 1111–1116, 2011.
- [22] D. C. Fu, X. L. Zhang, R. L. Barber, and U. Bach, "Dye-sensitized back-contact solar cells," *Advanced Materials*, vol. 22, no. 38, pp. 4270–4274, 2010.

Research Article

Acute Toxicity of Double-Walled Carbon Nanotubes to Three Aquatic Organisms

Lungile P. Lukhele,^{1,2} Bhekie B. Mamba,³ Ndeke Musee,⁴ and Victor Wepener⁵

¹Department of Applied Chemistry, University of Johannesburg, P.O. Box 17011, Doornfontein, Johannesburg 2028, South Africa

²Department of Zoology, University of Johannesburg, P.O. Box 534, Auckland Park 2006, South Africa

³Nanotechnology and Water Sustainability Research Unit, College of Engineering, Science and Technology, University of South Africa Florida Campus, Roodepoort 1709, South Africa

⁴Nanotechnology Sustainability Research Group, Natural Resources and the Environment, CSIR, P.O. Box 395, Pretoria 0001, South Africa

⁵Unit for Environmental Sciences and Management, North West University, Private Bag X6001, Potchefstroom 2520, South Africa

Correspondence should be addressed to Lungile P. Lukhele; lungi606@gmail.com

Received 6 November 2014; Revised 8 January 2015; Accepted 12 January 2015

Academic Editor: Biswarup Sen

Copyright © 2015 Lungile P. Lukhele et al. This is an open access article distributed under the Creative Commons Attribution License, which permits unrestricted use, distribution, and reproduction in any medium, provided the original work is properly cited.

This study investigated the toxicity of double walled carbon nanotubes (DWCNTs) to three aquatic organisms, namely, *Pseudokirchneriella subcapitata*, *Daphnia pulex*, and *Poecilia reticulata* under the influence of exposure media properties specifically the ionic strength and organic matter represented by humic acid. Results indicated that ionic strength enhanced DWCNTs agglomeration whilst humic acid stabilized the CNTs and in turn inhibited the formation of aggregates. LC₅₀s for *D. pulex* were higher at 2.81 and 4.45 mg/L for pristine and oxidised DWCNTs, respectively; however, *P. reticulata* had lower values of 113.64 mg/L and 214.0 mg/L for the same CNTs correspondingly. *P. subcapitata* had EC₅₀s of 17.95 mg/L and 10.93 mg/L for the pristine and oxidised DWCNTs, respectively. In the presence of humic acid high DWCNTs acute toxicity towards *D. pulex* and *P. reticulata* was observed but ionic strength led to opposite effect irrespective of DWCNTs form. Both humic acid and ionic strength shielded the *P. subcapitata* from toxic effects of DWCNTs. Overall, our findings suggest that the toxicity of DWCNTs in the aquatic systems (i) will be dependent on media properties and (ii) is likely to proceed at different rates to organisms at different trophic levels.

1. Introduction

Carbon nanotubes (CNTs) are the most widely studied class of engineered nanomaterials. This is due to carbon's unique hybridisation properties and the sensitivity to variations in the synthesis conditions allowing tailoring of these nanostructures for specific applications [1]. The science and applicability of CNTs are well understood and that is the main reason why they are quite popular. CNTs vary by the number of graphitic layers in their side walls. The types that have been extensively studied and are commercially available are single-walled carbon nanotubes (SWCNTs), double-walled carbon nanotubes (DWCNTs), and multiwalled carbon nanotubes (MWCNTs) [2, 3]. Double-walled carbon nanotubes (DWCNTs) have attracted much attention in recent years because they are an excellent compromise between SWNTs and

MWNTs [4]. This is because it is possible to functionalise the outer wall to ensure interaction with its external environment while retaining the unique properties of the inner carbon nanotube. Chemical and physical properties of DWCNTs are similar to those of SWNTs [4, 5].

The synthesis and use of CNTs lead to their release into the environment, particularly the aquatic environment. This may be as a result of the use of CNTs and through wastewater containing nanowaste and runoff from landfills [6]. Hence data on the fate and behaviour of CNTs in different types of natural water systems as well as their potential ecotoxicity is essential for the quantitative assessment of environmental risks of nanomaterials [7]. Generally, the development, production, use, and disposal of new technologies have been found to cause a significant impact on the environmental dimension of sustainable development [8].

Hence, proactive investigation on the impact of CNTs in the aquatic environment merits urgent attention. This is because the sustainability of a given technology, from an economical, sociological, environmental, and governance perspective, is dependent on the understanding of its impacts on humans and other biological life forms in the environment [9].

Aquatic toxicology has been identified as a useful tool for assessing environmental risks associated with CNTs [10]. Acute toxicity is the most fundamental of toxicological investigations. It is routinely performed as a regulatory requirement for different substances such as chemicals and wastewater effluents [10]. The results of these tests are used to determine the hazard that may be caused by the tested substance and wastewater effluents [11, 12]. Acute toxicity results also inform the experimental design for subsequent sublethal toxicity investigations [13]. Research on nanoecotoxicology has focused on estimating lethal concentrations, evaluating sublethal effects on organisms, and identifying mechanisms of toxicity on ENMs [7]. The focus has been on biological endpoints at population level such as growth, reproduction, and mortality [11]. Like chemicals, ENMs trigger several of the fundamental toxicity responses. The quantitative toxicity data such as EC_{50} are essential in the estimation of a precise dose-response relationship between organisms and test material [14–16].

The aquatic ecotoxicity of ENMs is greatly influenced by their speciation in aquatic environments [17, 18]. The stability or agglomeration of ENMs in aquatic environments is mainly governed by particle characteristics and physicochemical parameters of water such as ionic strength, pH, and dissolved organic matter [19, 20]. The physicochemical parameters alter the colloidal behaviour of nanoparticles which then has a direct bearing on the nanoparticle-organism interaction in aquatic environments. The change in nanoparticle-organism interactions has been reported to impact the toxicity of ENMs [20, 21]. Hence, it is important to examine the effect of physicochemical parameters on the acute toxicity of ENMs to aquatic organisms.

This study reports the influence of ionic strength (based on Na and Ca) and humic acid on the acute toxicity of pristine and oxidised DWCNTs to three aquatic organisms representing three different trophic levels, that is, primary consumers (algae), *P. subcapitata*; macroinvertebrates, *D. pulex*; and fish, *P. reticulata*. These organisms form part of standard toxicity testing guidelines such as those issued by the OECD and USEPA [10, 11].

2. Materials and Methods

Double-walled carbon nanotubes were synthesised in our laboratories using the catalytic vapour deposition method as described by Flahaut and coworkers [6]. The DWCNTs were oxidised by refluxing the DWCNTs in nitric acid at 55°C for 3 h.

2.1. Characterisation of DWCNTs. Surface morphology and DWCNT diameter were determined using high resolution transmission electron microscopy (HR TEM, JEOL Jem-2100) and scanning electron microscopy (SEM, JEOL JSM

7500F coupled with EDX). Elemental composition of DWCNTs was determined using energy dispersive X-ray spectroscopy (EDX) and surface functionality was determined using Raman spectroscopy (Perkin Elmer Raman Microscope, RamanMicro 200) and Fourier transform infrared spectroscopy (Perkin Elmer Spectrum 100 FT-IR-spectrometer). Hydrodynamic size and zeta potential in aqueous DWCNT suspensions were determined using dynamic light scattering (Malvern Zetasizer Nano series, NanoZS).

2.2. Preparation of Stock Suspensions and Their Characterisation

2.2.1. Preparation of DWCNT Suspensions of Varying Ionic Strengths (Ca^{2+}). Moderately hard reconstituted waters with varying ionic Ca^{2+} strengths were prepared by varying the amount of calcium carbonate. Reconstituted waters with ionic strengths of 0.00449 M Ca^{2+} , 0.0226 M Ca^{2+} , and 0.0339 M Ca^{2+} were prepared. The salts used to prepare reconstituted water were kept constant when Ca^{2+} was varied. The salts were 0.2400 g of $NaHCO_3$, 0.0200 g of KCL, and 0.1500 g of $MgSO_4$ and these were added to 5 L of Milli-Q water. The DWCNT suspensions were prepared by adding 50 mg of DWCNTs to 100 mL of the prepared waters with varying ionic strengths. The suspensions were sonicated for 2 h and were shaken at 30 min intervals. The suspensions were then refrigerated at 4°C for 24 h.

2.2.2. Preparation of DWCNT Suspensions at Varying Humic Acid Concentrations. A stock solution of humic acid was prepared by dissolving 50 mg of humic acid powder containing 20% ash (Fluka) in 100 mL of Milli-Q water. The humic acid powder contained ash estimated to be 20% of the mass of the powder. It was important to first eliminate the ash content from the solution and determine the exact concentration of humic acid in the stock solution. The solution was filtered with a 0.45 μm filter paper under vacuum. A series of standards were prepared using the stock solution and were analysed using a Cary UV 50 scan UV spectroscopy and the dissolved carbon was analysed using a total organic carbon analyser. A calibration curve was plotted to obtain an equation that was used to calculate the TOC value of the stock solution using readings at 254 nm. The dissolved organic carbon was determined using the Tekmar Apollo 9000 total organic carbon (TOC) analyser.

2.2.3. Preparation of DWCNT Suspensions at Varying Ionic Strengths (Na^+). Double-walled carbon nanotubes stock suspensions were prepared by adding 5 mg of carbon nanotubes (pristine and oxidised) to 100 mL of Milli-Q water (pH 7). Sodium chloride was added to the DWCNT suspension to vary the ionic strength in suspensions from 0.00335, 0.00585, 0.00835, and 0.0139 M NaCl. The suspensions were then sonicated for 2 h and refrigerated at 4°C for 24 h (to stabilise the suspensions).

The hydrodynamic particle size was determined and zeta potential measurements were done for each of the different

salinity and humic acid conditions using dynamic light scattering.

2.3. Bioassays

2.3.1. *Pseudokirchneriella subcapitata* Growth Inhibition Test. The algal toxicity tests were carried out using the Algaltoxkit sourced from MicroBioTests Inc. (Cat. # 030229). The test kit contained prepared nutrient stock solutions for the culturing medium, matrix dissolving medium, algal beads, and plastic long cells. In our tests, the long cells were replaced with glass Erlenmeyer flasks.

Algal culturing medium (2 L) was prepared by adding 20 mL of nutrient stock solution A and adding 2 mL (each) of nutrient stock solutions B, C, and D. The medium was aerated and set aside. The *P. subcapitata* culture was prepared by first dissolving the alginate matrix (used to form the beads) in matrix dissolving medium in order to recover viable and cultivable cells and thereafter rinsing the cells in culture medium 3 times. The algal culture was resuspended in 25 mL of culture medium. The cell density was determined using a spectrophotometer and was confirmed using manual cell counting.

The DWCNT stock solution was prepared by mixing 10 mg of dry DWCNT and 100 mL of culture medium in 100 mL Schott bottles. The mixture was then sonicated for 2 h in an ultrasonication bath. The suspensions were prepared 24 h before toxicity tests were carried out and were refrigerated at 4 °C.

A total of six exposure concentrations arranged in a geometric series with a separation factor of 2 were prepared, with the highest DWCNT concentration being 100 mg/L. The diluted DWCNT suspensions (25 mL in each flask) were placed in Erlenmeyer flasks. A total of 10 000 algal cells (volume of stock solution added was calculated using the cell density in stock solution) were added to each Erlenmeyer flask. Each DWCNT concentration was prepared in duplicate. Controls consisting of duplicate negative (i.e., no DWCNTs added) and positive (reference toxicant CdCl₂, 100 mg/L) were included in each bioassay. The algae were incubated for a period of 96 h in an incubator under a 16 : 8 h, light : dark regime.

Two samples (0.5 mL) from each Erlenmeyer flask were collected at 24 h intervals. Algal cell densities in samples were determined by cell counting using a haemocytometer chamber under a light microscope. Calculations of growth inhibition were done according to the OECD guidelines [22].

Algae cells were counted using a haemocytometer chamber with at least two counts for each replicate. Manual cell counting was required because the determination of cell density by UV/Vis absorption was not possible due to the large variations in the background spectrum of the test suspensions containing CNT. The lack of quicker, less laborious, and validated methods to quantify green algae in the presence of CNT and particulate matter in general has made manual cell counting the only option.

2.3.2. *Daphnia* (Invertebrate) Immobilisation Test. Test organisms, *Daphnia pulex*, were sourced from in-house

cultures maintained in the aquarium at the University of Johannesburg. *Daphnia pulex* was cultured in a temperature controlled room at 22 ± 2 °C under 14 hr illumination. The daphnids were cultured in moderately hard synthetic water and were fed dried yeast. The *D. pulex* bioassay was conducted in a 25 mL volume using 60 mL glass beakers under static nonrenewal conditions for 48 h. A total of five neonates were exposed to test solution with three replicates per concentration. Exposure solutions were prepared from a DWCNT stock solution and moderately hard reconstituted water was used as a medium for the test [23]. DWCNT concentrations arranged in a geometric series with a separation factor of 1.5 were prepared, with the highest DWCNT concentration being 10 mg/L. The number of mortalities was recorded at 24 h intervals for the duration of the study period. Dead organisms were gently removed from the exposure vessel using a Pasteur pipette. Following exposure, the surviving organisms in each beaker were collected for microscopic analysis.

2.3.3. *Poecilia reticulata* (Fish) Acute Toxicity Test. Fish were sourced from Kirsten Aquaculture, situated at Modimolle, South Africa. The age of the fish used for exposure experiments ranged from 10 d to 21 d. The fish were exposed for 96 h to different DWCNT concentrations (500 mg/L, 250 mg/L, 125 mg/L, 62.5 mg/L, 31.25 mg/L, and 15.6 mg/L) using the static nonrenewal test. The tests were conducted in 600 mL low form glass beakers using moderately hard reconstituted water and five fish were placed in each beaker. The exposure tests were done in triplicate, with four negative controls (no DWCNTs added) and four positive controls (reference toxicant, 1000 mg/L K₂Cr₂O₇). The experiments and controls were prepared in accordance with the OECD Guidelines 203 (2002) (pH 6 to 8.5, dissolved oxygen >80%, conductivity <10 μS/cm, and temperature 21 °C to 25 °C). Fish mortalities were recorded over the 96 h period at 24 h intervals. Dead fish were removed from exposure vessels using a pair of forceps while carefully avoiding the agglomerates surrounding the fish. Abiotic parameters of test solutions were tested before fish were added [24].

2.4. Statistical Analysis. As an estimate of relative lethal toxicity, EC₅₀/LC₅₀ values were based on the cumulative mortality observed at the end of a desired exposure time. EC₅₀/LC₅₀ values for each test species together with their respective 95% confidence intervals (CI) were calculated using the most appropriate statistical method for the specific toxicity data. The USEPA Probit Analysis Program used for calculating LC/EC values (version 1.5) was initially used to calculate the EC₅₀/LC₅₀ values [25]. When data did not fit the assumptions of the Probit method, the data were then analysed using the Trimmed Spearman-Kärber method [26]. To determine whether there were any significant differences between the EC₅₀/LC₅₀ values for the different DWCNT concentrations and treatments, the following formula was used: $f_{1,2} = \text{antilog} \sqrt{((\log f_1)^2 + (\log f_2)^2)}$, where f is the factor for 95% confidence limits of the EC₅₀/LC₅₀ and is calculated by dividing the upper confidence limit by the EC₅₀/LC₅₀. If the ratio of the higher EC₅₀/LC₅₀ to the lower EC₅₀/LC₅₀ exceeds the value of $f_{1,2}$ for both the upper and

lower 95% confidence limits, the EC_{50}/LC_{50} s are considered to be significantly different [27].

3. Results and Discussion

3.1. Characterisation of DWCNTs

3.1.1. Surface Morphology. The SEM micrograph of pristine DWCNTs showed a mixture of catalyst residues and some protruding fibre-like structures (Figure 1(a)). The fibre-like structures are DWCNTs surrounded by excess catalyst and some amorphous carbon. After oxidation, a large amount of the residual catalyst and amorphous carbon were removed leaving DWCNTs. However, small amounts of catalyst residue were still visible (Figure 1(b)).

The surface morphology of DWCNTs was analysed using TEM. Figure 2(a) is a TEM image of pristine DWCNTs and they contain some residual catalyst within the DWCNTs and amorphous carbon around the tubes. Some residual catalyst is still present in oxidised DWCNTs (Figure 2(b)). The average diameter of DWCNTs was found to be 3.60 nm and the majority of CNTs had a diameter range of 2-3 nm (Figure 2(c)).

3.1.2. Surface Functionalisation. Oxidation of DWCNTs was confirmed by FT-IR spectroscopy. The peak at around 1721 nm is characteristic of the C=O group. Some O-H groups were identified at the 3492 nm peak and C-O groups were identified at around 1207 nm for the oxidised DWCNTs but were insignificant in the case of pristine DWCNTs (Figure 3).

The quality of DWCNTs was determined using Raman spectroscopy. The D-band peak which was observed at approximately 1300 cm^{-1} , for both pristine and oxidised DWCNTs, is related to the presence of defects on the walls of CNTs (Figure 4). The G-band observed at approximately 1600 cm^{-1} is associated with the in-plane vibrations of graphene sheets. The D-band/G-band ratio is a general indicator of the extent of disorder within CNTs.

3.2. Elemental Composition. Pristine DWCNTs contained a large amount of magnesium and molybdenum which originated from the magnesium oxide supported Mo/Co catalyst used for the synthesis of DWCNTs. Some oxygen was also present in pristine DWCNTs (Figure 5(a)).

After oxidation, DWCNTs still contained some of the molybdenum. Magnesium oxide in the catalyst is used as a support for the molybdenum and acid treatment removed most of the magnesium oxide leaving the molybdenum (Figure 5(b)).

The oxygen fundamentally found to be present in DWCNTs is a result of oxidation in the presence of nitric acid. Carbon, as expected, was also detected.

Characteristics such as size distribution, surface chemistry, surface charge, and dispersion in aqueous phase have been identified as essential in studying the environmental fate of DWCNTs. Such data are essential because the interactions of environmental and biological systems are dependent on them [7].

Surface morphology and the presence of impurities in pristine DWCNT were determined by TEM and SEM. Pristine DWCNTs had impurities on their surface while oxidised DWCNTs had very few impurities. Elemental analysis using EDX indicated that pristine DWCNTs contained residual magnesium and molybdenum content originating from the catalyst used during synthesis of DWCNTs. Flahaut and colleagues reported a similar finding of metal residue on DWCNTs and attributed these residues to poor dispersion of the metal catalyst. Some amount of oxygen was also present in as-prepared DWCNTs. The oxygen content originated from a MoO_x , a species detected by Flahaut and coworkers through X-ray diffraction [6]. Metal catalyst residues are often very difficult to remove from carbon-based nanoparticles. These metal particles are normally embedded in the tube or particle and their removal involves using harsh acid treatment which can destroy the nanoparticle [2, 7].

Oxidation of DWCNTs was confirmed using FT-IR spectroscopy where vibrational peaks of C=O, C-O, and O-H bonds were detected in oxidised DWCNTs. From the Raman spectra of pristine and oxidised DWCNTs the I_D/I_G ratio of pristine DWCNTs was low (between 0.1 and 0.2), whereas that of oxidised DWCNTs was approximately 1. A low I_D/I_G ratio indicates that the material exhibits high crystallinity while a higher ratio indicates the presence of defects on the surface of DWCNTs confirming the presence of functionalities on the surfaces of DWCNTs [2].

3.3. Effect of Changes in Physicochemical Properties of Water on the Stability of DWCNT Suspensions. Ionic strength (IS) and natural organic matter were found to influence the surface charge on DWCNT surfaces resulting in reduced or increased stability of DWCNTs in water suspensions.

3.3.1. Effect of Ionic Strength. Increasing ionic strength caused an increased aggregation of both pristine and oxidised DWCNTs. The salts used in suspensions to vary ionic strength, CaCO_3 and NaCl , had different effects on the colloidal stability of pristine and oxidised DWCNTs.

3.3.2. The Effect of Na^+ . The addition of sodium chloride in the DWCNTs suspensions resulted in increased aggregation in both pristine and oxidised DWCNTs as the IS was increased (Figure 6). Oxidised DWCNTs had a higher hydrodynamic particle size compared to pristine DWCNTs. Pristine DWCNTs had a slight decrease in particle size at 0.00835 M. In subsequent ionic strengths, an increase in particle size was observed.

A decrease in zeta potential for both pristine and oxidised DWCNTs was observed (Figure 6) with the exception of 0.00835 M IS, where there was an increase for both DWCNTs. There was a greater increase for oxidised DWCNTs since oxidised DWCNTs had a lower zeta potential at 0 M but had a higher zeta potential at 0.00835 M when compared to pristine DWCNTs.

The increase in hydrodynamic size in particles is as a result of higher aggregation caused by the increased salinity in water. The presence of electrolytes in water affects the stabilisation of colloids in the aqueous phase thus lowering

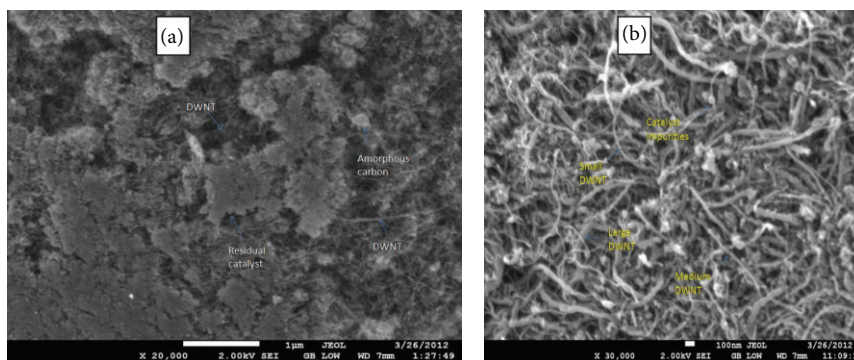


FIGURE 1: (a) SEM micrograph of pristine DWCNTs showing catalyst residues. (b) SEM micrograph of oxidised DWCNTs showing nanotubes of different sizes and some catalyst residues.

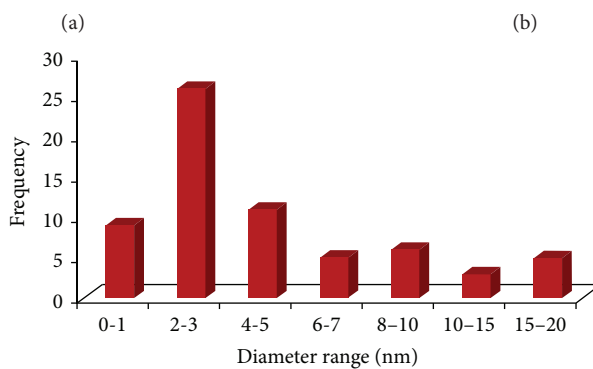
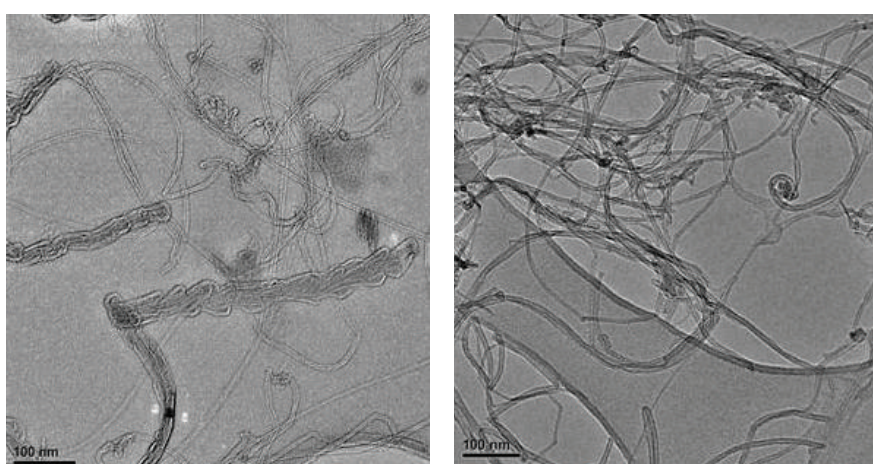


FIGURE 2: TEM micrographs of (a) pristine and (b) oxidised DWCNTs. The pristine DWCNTs have excess catalyst on their surfaces. The oxidised DWCNTs have clean surfaces with scattered dark spots which are catalyst residues. (c) A graph showing the diameter size distribution for the synthesized DWCNTs.

the concentration of smaller particles in the water column [28]. Similar results were reported for MWCNTs in aqueous suspensions where their aggregation increased when the NaCl concentration was doubled in the suspensions [29]. A general decrease in zeta potentials of both pristine and oxidised DWCNTs was observed with increased salinity (Figure 6). However, at 0.00835 M IS, there was an increase in zeta potential for both oxidised and pristine DWCNTs.

This may be attributed to the low Na^+ concentration not having an effect on the electric double layer of DWCNTs. The subsequent decrease in zeta potential for both oxidised and pristine DWCNTs confirms the data obtained for hydrodynamic size that high aggregation resulted from the increase of Na^+ in suspensions. The positively charged metal ion, Na^+ , neutralises the surface charge on the surfaces of DWCNTs and compresses the double layer of the DWCNTs,

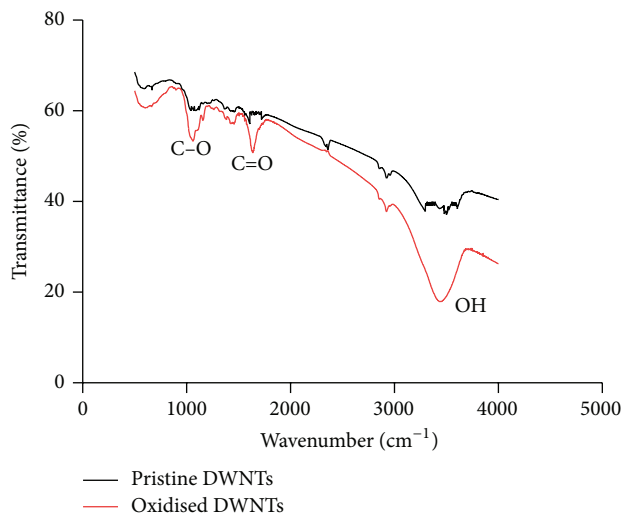


FIGURE 3: FT-IR of both pristine and oxidised DWCNTs illustrating the major functional groups present in oxidised DWCNTs which are not found in pristine DWCNTs.

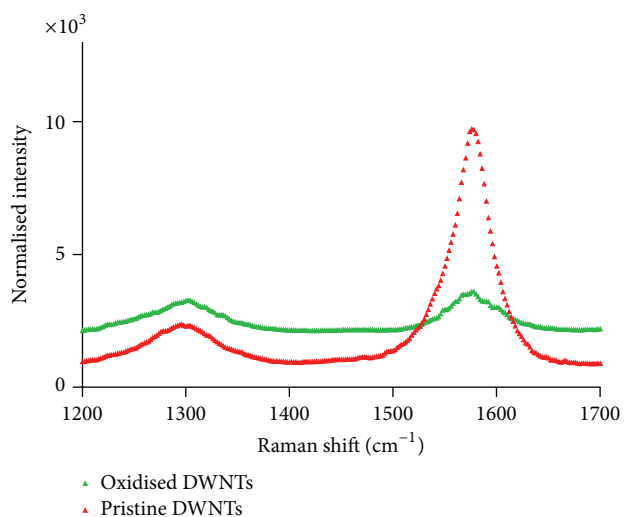


FIGURE 4: Raman spectra of pristine and oxidised DWCNTs showing different intensities of the D- and G-bands in both pristine and oxidised DWCNTs.

resulting in the reduction of electrostatic repulsion between DWCNTs [30]. Na^+ ions were reported to have an influence on the aggregation of MWCNTs at higher concentrations when compared to divalent cations such as Mg^{2+} and Ca^{2+} . Such observations were attributed to the difference in the ionic strength resulting from the presence of monovalent and divalent cations in solution [29].

3.3.3. The Effect of Ca^{2+} . Increased IS in water promotes aggregation in both pristine and oxidised DWCNTs as confirmed by the increased hydrodynamic particle size with increased hardness (Figure 7). Pristine DWCNTs had a larger hydrodynamic size at all water hardness levels.

It was found that zeta potential data correlated with the increased aggregation observed with increased IS. Pristine DWCNTs had a slightly lower average zeta potential at the different IS levels (Figure 7). There was a sharp decrease in zeta potential between 0 M and 0.00449 M for pristine DWCNTs followed by little change in zeta potential between IS of 0.00449 M and 0.0226 M. DWCNTs in IS of 0.0339 M showed a decrease in zeta potential.

Oxidised DWCNTs had a slight increase in zeta potential between IS of 0 M and 0.00449 M. Thereafter a consistent decrease in zeta potential was observed with increased cation content (Figure 7).

Both DWCNT types had increased hydrodynamic sizes as the IS of water was increased. However, there was no noticeable increase in hydrodynamic size of both pristine and oxidised DWCNTs from the IS of 0.0226 to 0.0396 M. The zeta potential of oxidised DWCNTs increased slightly in IS of 0.00449 M and decreased in the higher IS values (Figure 7). The zeta potential decrease at 0.00449 was not significantly different from the zeta potential of oxidised DWCNTs in distilled water. Pristine DWCNTs had decreased zeta potential with increased water hardness. However, the decrease was small (between 0.00449 M and 0.0226 M). Divalent ions in water contribute towards the reduction of the double layer of particles resulting in the shielding of electrostatic charges of particles [31]. Divalent ions such as calcium have been reported to efficiently screen negative charges on CNT surfaces. The screening of the negative charges results in a shift of zeta potentials to less negative values [32]. The presence of calcium in MWCNT suspensions consequently increased their hydrodynamic size [32, 33]. In another study by Smith and coworkers, it was revealed that calcium cations have a greater influence on the aggregation of MWCNTs than sodium ions [29]. These observations were attributed to the higher ionic strength presented by Ca^{2+} in the suspensions at lower concentrations compared to that of Na^+ [29].

3.4. Effect of Humic Acid. There was a higher amount of smaller particles (DWCNT aggregates) suspended in water containing humic acid compared to the blanks. The zeta potentials of DWCNTs confirm that there was an increase in the repulsion energies of DWCNT particles.

Addition of humic acid to DWCNT suspensions resulted in more negative zeta potential values. It was shown that pristine DWCNTs had a consistent reduction in zeta potential up to around 2 mg/L of humic acid (Figure 8). The decrease in zeta potential was relatively small thereafter. This may be related to the maximum amount of humic acid that has an effect on the zeta potential of DWCNTs. There was a sharp decrease in zeta potential values of oxidised DWCNTs when the concentration of humic acid was between 0 mg/L and 1 mg/L humic acid. A slight increase in zeta potential between 1 mg/L and 3.64 mg/L was observed. Oxidised DWCNTs were found to have a higher increase in zeta potential when humic acid was added to oxidised DWCNT suspensions compared to pristine DWCNTs.

Humic substances are a fraction of natural organic matter and are ubiquitous in the aqueous environments. Humic

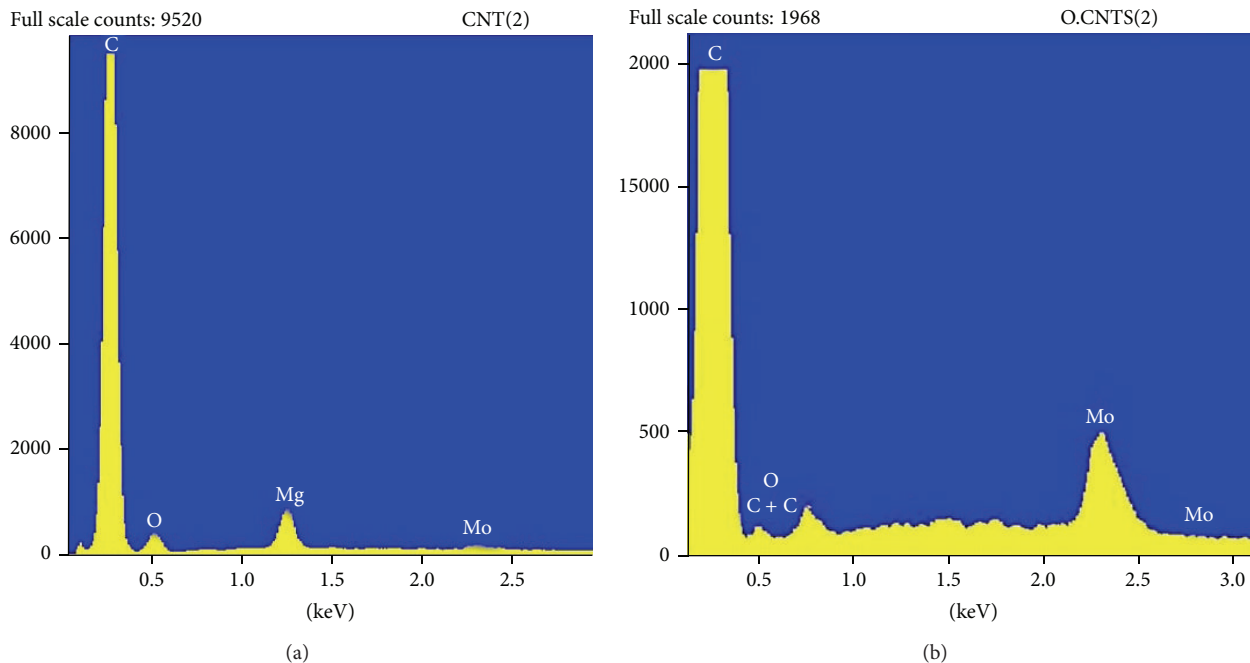


FIGURE 5: EDX spectra of (a) pristine and (b) oxidised DWCNTs showing their elemental composition.

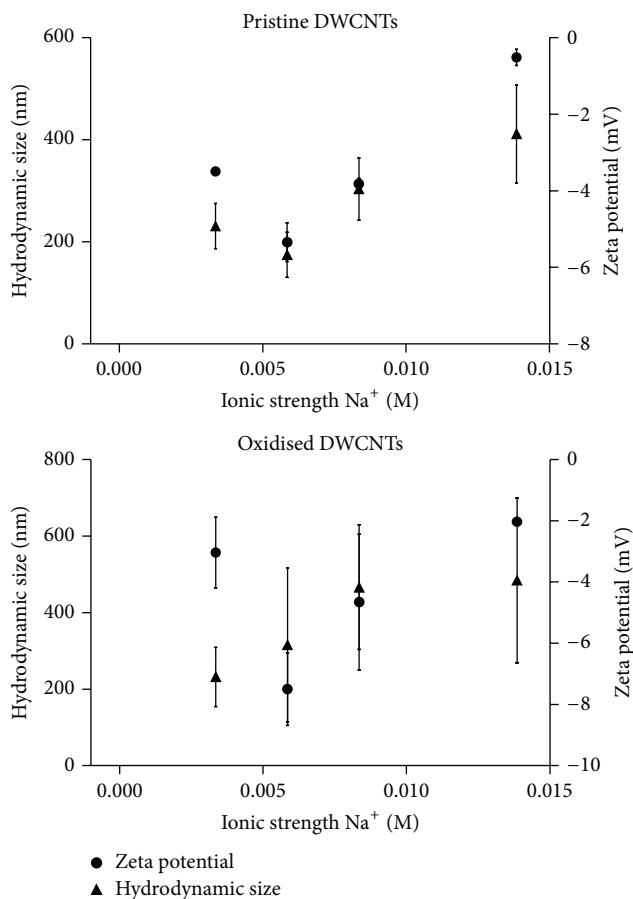


FIGURE 6: Hydrodynamic size and zeta potentials of DWCNTs at different IS (Na⁺) levels (error bars are the ranges of hydrodynamic size and zeta potentials).

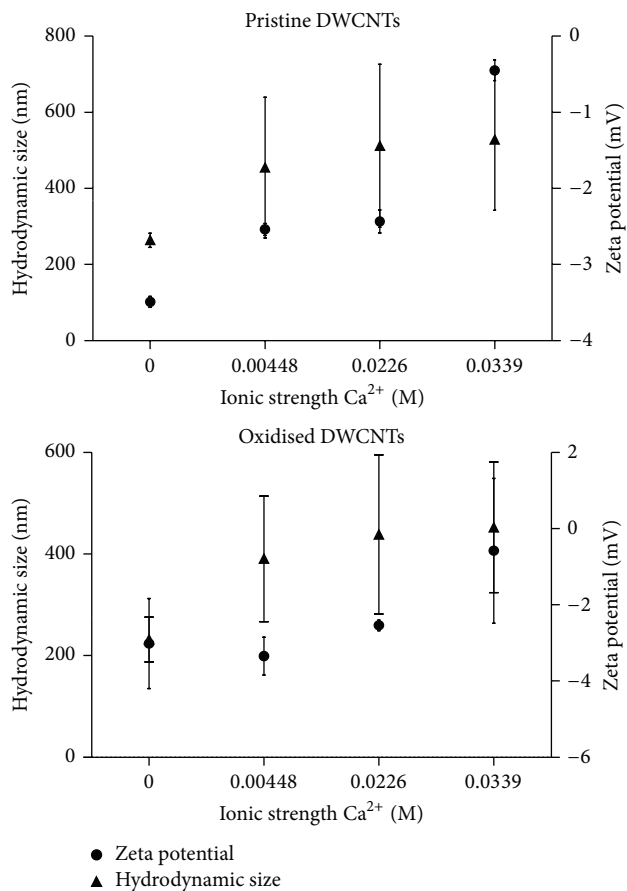


FIGURE 7: Hydrodynamic size and zeta potentials of DWCNTs at different IS (Ca²⁺) levels.

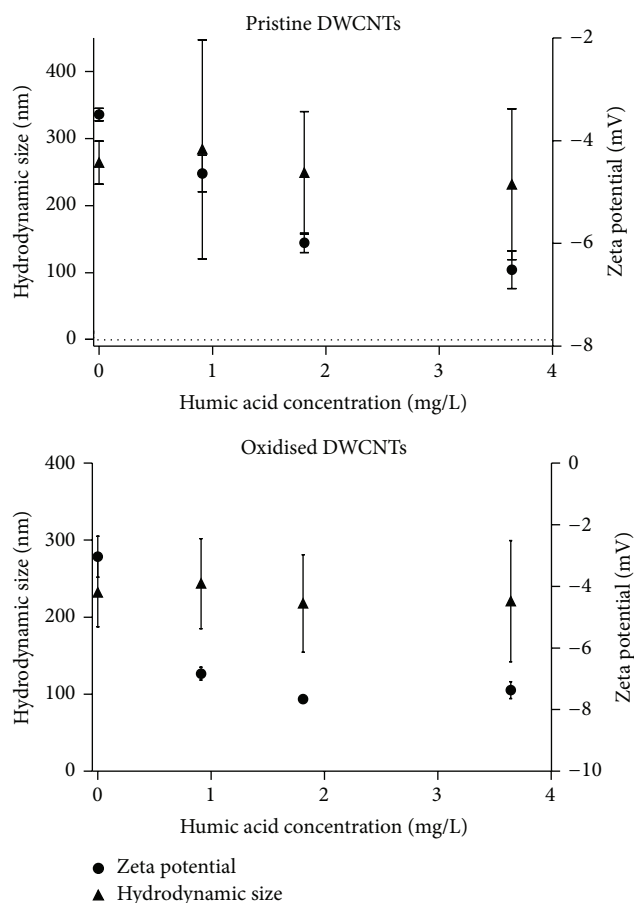


FIGURE 8: Hydrodynamic size and zeta potentials of DWCNTs at different humic acid levels.

acids are rich in aromatic moieties which, in theory, can interact with electron-rich surfaces such as graphene surfaces. Humic substances are known to decrease sedimentation rates of carbonaceous nanomaterials in aqueous suspensions [34]. The hydrodynamic size of particles in water containing humic acid decreased with an increase in humic acid concentration. Humic acid brings about a stabilising effect on MWNTs [32, 35, 36]. Pristine DWCNTs had a higher hydrodynamic particle size when compared to oxidised DWCNTs in humic acid. An increase in hydrodynamic particle size at approximately 1 mg/L of humic acid for pristine DWCNTs was observed. At higher humic acid concentrations, a consistent decrease in hydrodynamic particle size was noted. For oxidised DWCNTs, no change in hydrodynamic particle size at 1 mg/L humic acid was observed. In subsequent humic acid concentrations, however, a decrease in hydrodynamic particle size was observed. Corresponding zeta potentials were observed where more negative surface charges of DWCNTs were observed confirming that smaller hydrodynamic particle size is a result of steric stabilisation of DWCNTs in aqueous suspensions [37]. It should be noted that π - π interactions are the main mechanism governing the sorption of humic acid on graphene surfaces of CNTs. The presence of electron-donating substituents on surfaces of MWCNTs enhances the sorption of polar moieties which are electron acceptors

[38, 39]. Moreover, oxygen containing functionalities on CNT surfaces have also been hypothesised to interact with humic acid through hydrogen bonding [36, 38]. The latter, however, was identified as a less important driving force for the adsorption of humic acid to CNTs [36, 38]. Schwyzer and colleagues reported that MWCNTs containing 4% surface oxygen provided a better colloidal stability when suspended in Suwannee River humic acid (SRHA) than MWCNTs containing 2% surface oxygen [32]. Schierz and Zänker also discovered that acid-functionalised MWNTs were more stable in water containing humic acid compared with pristine MWNTs [31]. Since humic acid is adsorbed on carbon nanotubes' surfaces, the sorbed humic acid inhibits aggregation through steric interactions imparted by the adsorbed humic macromolecules [35, 37, 40]. Surfactants such as sodium dodecyl sulphate (SDS) have previously been used to disperse DWCNTs in water. The average hydrodynamic size of the aggregates was 290 nm, which was comparable to the average hydrodynamic size of oxidised DWCNTs in the current study [41].

3.5. *Pseudokirchneriella subcapitata* Growth Inhibition Test.

The general trend in the exposure experiments done for this study is that there is an increase in growth inhibition with an increase in DWCNT concentration. Figure 4 illustrates the growth inhibition of algae by the different concentrations of agglomerated DWCNTs. It can be noted that the growth inhibition increases with increased DWCNT concentrations. For DWCNT concentrations between 0.708 mg/L and 25 mg/L, there is no significant difference in the algae growth inhibition. A sharp increase can be observed for the highest concentration.

The growth inhibition caused by pristine DWCNTs was higher than that of oxidised DWCNTs. The EC_{50} of pristine DWCNTs was found to be 17.95 mg/L while oxidised DWCNTs had an EC_{50} of 10.93 mg/L. Varied environmental parameters such as humic acid content and ionic strength (using both monovalent and divalent cations) resulted in the reduction of toxicity of both pristine and oxidised DWCNTs to *P. subcapitata*. The addition of humic acid (3.64 mg/L) to the exposure medium almost doubled the EC_{50} s of both types of DWCNTs. The EC_{50} of oxidised DWCNTs increased from 10.93 mg/L to 20.56 mg/L and the EC_{50} of pristine DWCNTs also increased from 17.95 to 31.65 mg/L. The effects of ionic strength were determined by adding varying amounts of calcium carbonate and sodium chloride. It was found that decreased ionic strength (Ca^{2+}) resulted in lowered toxicity of DWCNTs. Also, increased ionic strength (Ca^{2+}) resulted in doubled EC_{50} . Changing the ionic strength by adding lower amounts of Na^+ in exposure experiments resulted in significantly lowered toxicity of both pristine and oxidised DWCNTs. The ionic strength of 0.0139 M Na^+ resulted in EC_{50} s above the highest exposure concentration (50 mg/L) for both pristine and oxidised DWCNTs. However, for oxidised DWCNTs the increased ionic strength resulting from added Na^+ did not result in a general decrease in the toxicity. In 0.00585 M NaCl, the EC_{50} was 16.11 mg/L while in 0.00335 M, the EC_{50} was 26.22 mg/L. It was found that

only the highest Na^+ and Ca^{2+} concentrations resulted in significantly higher EC_{50} s than the other exposures (Table 1).

The algal cells were found to agglomerate with DWCNTs where a large amount of cells are entrapped in the DWCNT agglomerates. Figure 9 illustrates agglomeration of *P. subcapitata* with DWCNTs while some loose *P. subcapitata* cells surround the agglomerate.

Carbon nanotubes, SWCNT, DWCNTs, and MWCNT, have been reported to have an effect on the growth rates of various algal species [4, 42–45]. Such an effect has been found to be dose-dependent in all of these studies. Several researchers have reported that shading effect and agglomeration were the main causes of growth inhibition [43, 44]. They further stated that each of these factors influenced growth to different extents [43]. The extent of aggregation of DWCNTs played a major role in the growth inhibition of *P. subcapitata*.

Humic acid reduced agglomeration of DWCNTs (Figure 8) and as a result, DWCNTs in the algal tests did not form large agglomerates that could trap algal cells and deprive them of illumination. At the highest humic acid concentration, growth inhibition resulting from exposure to both pristine and oxidised DWCNTs was lowered because at this humic acid concentration, DWCNTs formed smaller agglomerates reducing the amount of algae trapped in agglomerates. Schwab and coworkers [44] reported that NOM increased the toxicity of MWCNTs. It is worth noting that the NOM used in their study was about 20 times more than the concentration used in the current study. They concluded that the toxicity of CNTs is due to a hydrogen-bond based interaction between algal cells and NOM covered CNTs that causes the clogging of algae with CNTs [44]. However, such hydrogen bridges may have been very weak between humic acid and DWCNTs since the concentration of humic acid was much lower and hence the interaction could have been compromised.

Moreover, the amounts of shading presented by smaller agglomerates may have been lower than with larger agglomerates. This may be due to the fact that humic acid reduced the hydrodynamic size of DWCNT agglomerates in the exposure medium and increased the specific surface area for the interaction of algal cells with the DWCNTs. Shading effect has been reported to be the major contributor in the toxicity of CNTs to algae [44]. According to Long and colleagues, illumination is vital for cell propagation and the blockage from illumination by carbon nanotubes has a negative impact on the growth rates of algae [43]. However, Bennett and coworkers found that shading did not have a significant effect on the reduced growth rates observed in their study [44]. Such inconsistencies in engineered nanomaterials (ENMs) data are as a result of altered standard protocols. For algal toxicity tests, the major sources of error are the methods employed to quantify growth [10]. Due to their particulate matter and dark colour, CNTs interfere with signal detection in spectrophotometric methods commonly employed to quantify algal growth. Consequently, manual cell counting used in this study has been identified as a reliable method for monitoring algal growth [10, 43, 44].

To vary the ionic strength, divalent and monovalent cations, respectively, were added to the exposure bioassays.

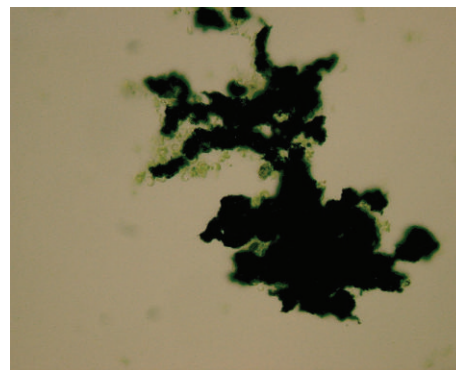


FIGURE 9: A light microscope picture of agglomeration of *P. subcapitata* with DWCNTs (some loose cells can be seen around agglomerate).

These cations influence the rate of agglomeration of nanoparticles such as DWCNTs since Ca^{2+} and Na^+ cause rapid agglomeration of CNTs. From Figures 6 and 7, it can be seen that these cations reduced the zeta potential of both pristine and oxidised DWCNTs and resulted in the formation of large agglomerates. We propose that, during the exposure experiment, the algae addition stage is likely to have taken place after DWCNTs had formed agglomerates and had settled at the bottom of the flask. These agglomerates had not trapped algal cells as they settled and had limited impact on the growth inhibition. However, this scenario does not eliminate the interaction between algae and the agglomerates.

Double-walled carbon nanotubes have been reported to have different toxicities to a marine algal species, *Thalassiosira pseudonana*, depending on the method of mixing. Sonicated DWCNTs had an EC_{50} of 1.86 mg/L while stirred DWCNTs had an EC_{50} of 22.7 mg/L [4]. The EC_{50} of MWCNTs to another marine algae species, *Dunaliella tertiolecta*, was 0.82 ± 0.02 mg/L. In this study, however, the method of mixing was not specified [46]. The EC_{50} is comparable to the EC_{50} of sonicated DWCNTs in the former mentioned study. A fixed concentration, 0.5 mg/L, of single-walled carbon nanotubes dispersed in 0.023% gum Arabic resulted in ca. 60% reduction in growth rates of *P. subcapitata* [42].

The acute toxicity of CNTs reported in the literature varies by orders of magnitude, especially for MWCNTs. The main reason for such variation is a result of differences in methods used to conduct toxicity tests and methods of evaluating cell densities in the algal toxicity test [10].

Oxidised DWCNTs were generally more toxic than pristine DWCNTs in all experiments. Wei and coauthors suggest that the toxicity is mediated through initial interaction between algal cells and CNTs [46]. With oxidised DWCNTs, there is a high probability that the interactions between the DWCNTs and algae cells were increased since oxidised DWCNTs had lower agglomeration compared to pristine DWCNTs. Wei and colleagues further observed that the interaction between algal cells and CNTs was stronger than steric and electrostatic repulsions between the negatively charged CNTs and algae [46]. The increased interaction between oxidised CNTs has been attributed to the formation

TABLE 1: Growth inhibition (EC_{50} s and 95% confidence intervals) for *Pseudokirchneriella subcapitata* following 72 h exposure to pristine and oxidised DWCNTs at different ionic strengths and humic acid (HA) concentrations. EC_{50} s with common alphabetical superscript do not differ significantly ($P < 0.05$).

| Exposure | Physicochemical characteristics | EC_{50} (mg/L) | Confidence limits (mg/L) |
|----------|--|--------------------|--------------------------|
| Pristine | 0.00335 (control reconstituted water) M Na | 17.95 ^a | 9.8–26.72 |
| | 0.00585 M Na | 29.47 ^a | 22.95–37.65 |
| | 0.00835 M Na | 30.89 ^a | 18.06–40.4 |
| | 0.0139 M Na | 52.31 ^b | 33.96–76.1 |
| Oxidised | 0.00335 (control reconstituted water) M Na | 10.93 ^a | 6.71–15.59 |
| | 0.00585 M Na | 27.22 ^a | 19.56–38.9 |
| | 0.00835 M Na | 16.11 ^a | 11.59–22.42 |
| | 0.0139 M Na | 49.31 ^b | 27.24–58.89 |
| Pristine | 0.00449 M Ca | 23.26 ^a | 17.04–28.00 |
| | 0.0226 M Ca | 25.57 ^a | 16.07–34.93 |
| | 0.0339 M Ca | 31.52 ^a | 21.56–50.92 |
| Oxidised | 0.00449 M Ca | 22.86 ^a | 15.59–42.42 |
| | 0.0226 M Ca | 22.91 ^a | 12.95–40.89 |
| | 0.03395 M Ca | 24.61 ^a | 13.37–34.44 |
| Pristine | 0 (control reconstituted water) M Na | 17.95 ^b | 9.80–26.72 |
| | 0.9 mg/L HA | 22.75 ^a | 14.39–31.70 |
| | 1.81 mg/L HA | 26.56 ^a | 10.95–34.61 |
| | 3.64 mg/L HA | 31.65 ^a | 10.87–42.19 |
| Oxidised | 0 (control reconstituted water) M Na | 10.93 ^a | 6.71–15.59 |
| | 0.9 mg/L HA | 13.59 ^a | 8.71–21.19 |
| | 1.81 mg/L HA | 18.01 ^a | 16.71–24.93 |
| | 3.64 mg/L HA | 20.56 ^a | 6.58–34.15 |

of hydrogen bonds between cell surfaces and oxygen defects [44]. This hydrogen bond formation was also the reason why interactions between DWCNTs with humic acid and algal cells increased and consequently increased the toxicity of these DWCNTs.

3.6. *Daphnia pulex* Immobilisation/Lethality Test. The acute toxicities of both pristine and oxidised DWCNTs to *D. pulex* were determined and the LC_{50} s were found to be in different orders of magnitude with *D. pulex* being the most sensitive in all experimental conditions studied. The mean EC_{50} s of *D. pulex* ranged between 1.801 mg/L and 4.480 mg/L (for both pristine and oxidised DWCNTs). Table 2 illustrates the average EC_{50} s of DWCNT under the experimental conditions studied.

Oxidised DWCNTs were generally less toxic to *D. pulex* than pristine DWCNTs. The EC_{50} of oxidised DWCNTs was 3.565 mg/L and addition of both humic acid and ionic strength (Ca^{2+} and Na^+) increased the toxicity of both pristine and oxidised DWCNTs. Addition of humic acid reduced the EC_{50} of pristine DWCNTs to below 2 mg/L while Na^+ reduced the EC_{50} to about 2.5 mg/L. Pristine DWCNTs in daphnia medium had an EC_{50} of 4.48 mg/L and the addition of humic acid and Ca^{2+} and Na^+ reduced the EC_{50} to about 3 mg/L for all experimental conditions.

The exposed organisms were studied under a light microscope to visualise how the organisms interact with the

DWCNTs. *Daphnia pulex* were found to have large amounts of dark material in their gut tract after exposure to DWCNTs. Ingestion was the main mode of uptake of DWCNTs by *D. pulex*. Figure 10 displays *D. pulex* after exposure to DWCNTs and the amount of DWCNTs in the gut tract of *D. pulex* was found to be dependent on the DWCNT concentration in exposure solutions. A similar trend was observed for both pristine and oxidised DWCNTs. Similar findings were reported for *D. magna* exposed to several nanoparticles such as SWCNTs, C_{60} , MWCNT, and titanium dioxide [47].

Visual inspection of *D. pulex* at 40x magnification under a light microscope suggested that the acute toxicity of DWCNTs was a physical effect attributed to clogging of the daphnid gut tract. Such clogging is likely to interfere with food processing in *Daphnia pulex* [48].

Pristine DWCNTs were found to be more toxic to *D. pulex* than oxidised DWCNTs. Pristine DWCNTs have a greater penchant to aggregate leading to the formation of more structurally complex aggregate arrays that interact differently within the gut of *D. pulex*. Nonfunctionalised MWNTs were reported to be more toxic than functionalised MWNTs to *Ceriodaphnia dubia* [48]. Depuration experiments also revealed that *C. dubia* had difficulty clearing the nanoparticles from the gut tracts even after 48 h. The interactions have been proposed by Kennedy et al. to be either physical or chemical [48]. Humic acid generally increased the toxicity of both types of DWCNTs. Since humic acid reduces

TABLE 2: Lethal concentrations (LC_{50} s and 95% confidence intervals) for *Daphnia pulex* following 48 h exposure to pristine and oxidised DWCNTs at different ionic strengths and humic acid (HA) concentrations. LC_{50} s with common alphabetical superscript do not differ significantly ($P < 0.05$).

| Exposure | Physicochemical characteristics | EC_{50} (mg/L) | Confidence limits (mg/L) |
|----------|--|--------------------|--------------------------|
| Pristine | 0.00335 (control reconstituted water) M Na | 2.801 ^a | 1.58–3.95 |
| | 0.00585 M Na | 2.710 ^a | 1.21–7.58 |
| | 0.00835 M Na | 2.835 ^a | 0.82–5.66 |
| | 0.0139 M Na | 3.163 ^a | 2.10–6.02 |
| Oxidised | 0.00335 (control reconstituted water) M Na | 4.480 ^a | 2.09–7.49 |
| | 0.00585 M Na | 3.320 ^a | 1.88–6.04 |
| | 0.00835 M Na | 3.048 ^a | 1.71–7.05 |
| | 0.0139 M Na | 3.541 ^a | 1.52–6.35 |
| Pristine | 0.00449 M Ca | 3.048 ^a | 1.51–6.43 |
| | 0.0226 M Ca | 2.81 ^a | 1.58–3.95 |
| | 0.03395 M Ca | 3.327 ^a | 1.72–6.44 |
| Oxidised | 0.00449 M Ca | 3.77 ^a | 1.01–5.49 |
| | 0.0226 M Ca | 4.48 ^a | 2.09–7.49 |
| | 0.03395 M Ca | 3.57 ^a | 1.81–7.58 |
| Pristine | 0 (control reconstituted water) M Na | 2.80 ^a | 1.58–3.95 |
| | 0.9 mg/L HA | 1.91 ^a | 1.21–7.58 |
| | 1.81 mg/L HA | 1.89 ^a | 0.82–5.66 |
| | 3.64 mg/L HA | 1.80 ^a | 1.10–6.02 |
| Oxidised | 0 (control reconstituted water) M Na | 4.48 ^a | 2.09–7.49 |
| | 0.9 mg/L HA | 4.07 ^a | 1.88–6.75 |
| | 1.81 mg/L HA | 3.25 ^a | 1.71–7.05 |
| | 3.64 mg/L HA | 3.07 ^a | 1.52–6.87 |



FIGURE 10: Changes in the density of oxidised DWCNTs in the gut tract of *D. pulex* with increasing exposure concentrations.

aggregation in DWCNTs, the average hydrodynamic size of DWCNTs is reduced. With reduced hydrodynamic size, the concentration of DWCNTs in aqueous solution increases and the potential biological effect is increased. In a study carried out by Edgington and coworkers it was reported that increasing DOC concentration (Suwannee River-NOM) did not have an effect on the toxicity [49]. They speculated that the MWCNTs were saturated with the SR-NOM at very low DOC concentration and had no effect on stabilisation of MWCNTs in exposure medium. There was no observable pattern in the results obtained; hence they concluded that increasing DOC concentration had no impact on the toxicity of MWCNTs. This was not the case in the current study as the average LC_{50} s did show an increase in toxicity with increased DOC concentrations (Table 2). The observed increase for both pristine and

oxidised DWCNTs was, however, statistically not significant ($P < 0.05$). These results suggest that reduced aggregation resulting from the addition of humic acid (Figure 8) increased probabilities of DWCNT uptake by *D. pulex*.

The increase in ionic strength decreased the toxicity of both pristine and oxidised DWCNTs. Increase of Na^+ did not have an effect on the toxicity of pristine DWCNTs but reduced the average LC_{50} of oxidised DWCNTs. Data on hydrodynamic size results show that increased ionic strength increased the hydrodynamic size of both pristine and oxidised DWCNTs with increased Ca^{2+} having a greater effect than increased Na^+ . The concentration of DWCNTs in these suspensions per unit volume is decreased and thus the amount of DWCNTs ingested by daphnia in such exposure conditions is low and results in lower biological effect. It is

TABLE 3: Lethal concentrations (LC₅₀s and 95% confidence intervals) for *Poecilia reticulata* following 96 h exposure to pristine and oxidised double-walled carbon nanotubes at different ionic strengths and humic acid (HA) concentrations. LC₅₀s with common alphabetical superscript do not differ significantly ($P < 0.05$).

| Exposure | Physicochemical characteristics | EC ₅₀ (mg/L) | Confidence limits (mg/L) |
|----------|--|-------------------------|--------------------------|
| Pristine | 0.00335 (control reconstituted water) M Na | 113.64 ^a | 43.34–267.66 |
| | 0.00585 M Na | 261.0 | 110.7–447.20 |
| | 0.00835 M Na | >500 | |
| | 0.0139 M Na | >500 | |
| Oxidised | 0.00335 (control reconstituted water) M Na | 214 ^a | 89.9–269 |
| | 0.0083585 M Na | >500 | |
| | 0.00835 M Na | >500 | |
| | 0.0139 M Na | >500 | |
| Pristine | 0.00449 M Ca | 112.53 ^a | 50.60–316.60 |
| | 0.0226 M Ca | 113.64 ^a | 43.66–113.64 |
| | 0.03395 M Ca | >500 | |
| Oxidised | 0.00449 M Ca | 274.17 ^a | 113–439 |
| | 0.0226 M Ca | 214 ^a | 89.9–269.1 |
| | 0.03395 M Ca | >500 | |
| Pristine | 0 (control reconstituted water) M Na | 113.64 ^a | 43.34–267.66 |
| | 0.9 mg/L HA | 106.93 ^a | 66.88–139.03 |
| | 1.81 mg/L HA | 84.15 ^a | 28.00–171.27 |
| | 3.64 mg/L HA | 64.56 ^a | 19.23–122.02 |
| Oxidised | 0 (control reconstituted water) M Na | 214.00 ^a | 89.90–269.1 |
| | 0.9 mg/L HA | 193.77 ^b | 97.44–287.11 |
| | 1.81 mg/L HA | 195.33 ^b | 91.7–322.30 |
| | 3.64 mg/L HA | 184.0 ^b | 100.3–316.10 |

possible that the DWCNT concentration per unit volume did not decrease when Na⁺ was increased as it did in the case of Ca²⁺.

Daphnia species are filter feeders and can take up large volumes of water when compared to body size [50]. They can ingest particles in the size range of 0.4 μm to 40 μm. This range includes algae and inorganic and organic particles [50, 51]. The single DWCNTs and their aggregates are within the lower end of the size range that can be ingested by *Daphnia* species.

In a study carried out on *D. magna* by Zhu and coworkers, they reported that the LC₅₀ of nonfunctionalised SWCNTs was 2.425 mg/L while unfunctionalised MWCNTs had an LC₅₀ of 22.751 mg/L [47]. The LC₅₀ of DWCNTs (2.81 mg/L) falls in between these values but is within the same order of magnitude of SWCNTs. Such findings suggest that the size of carbon nanotubes plays a role in the mediation of toxicity in *Daphnia* species. Theory suggests that smaller particles are likely to be more toxic as a result of their larger specific surface area which is conducive to greater nanoparticle-cell interaction.

Moreover, the presence of DWCNTs in the gut tract of *D. pulex* suggests that the gut is the main organ that interacts with DWCNTs. Zhu and coauthors suggested that the gut is where cell death occurs and consequently results in organism mortality [47].

3.7. *Poecilia reticulata* Lethality Test. Pristine DWCNTs were found to be more toxic to *P. reticulata* than oxidised DWCNTs. The average LC₅₀ of pristine DWCNTs was 113.64 mg/L while oxidised DWCNTs had an LC₅₀ of 214 mg/L. In the bioassays assessing the effect of humic acid and ionic strength, pristine DWCNTs were more toxic than oxidised DWCNTs in all conditions. In varied ionic strength (Na⁺), both pristine and oxidised DWCNTs had lowered toxicity as the salinity increased. At an ionic strength of 0.00585 M and 0.0139 M Na⁺, the LC₅₀ of both pristine and oxidised DWCNTs had lethal concentrations higher than the concentration of the stock suspensions (500 mg/L). In ionic strengths of 0 M Ca²⁺ and 0.00449 M Ca²⁺, reduced toxicity for both pristine and oxidised DWCNT was observed. At an ionic strength of 0.0226 M, the highest ionic strength (Ca²⁺), the toxicity was lowered such that the LC₅₀ in hard water was higher than the concentration of the stock suspensions (500 mg/L).

In experiments on the effect of humic acid, the toxicity of DWCNTs was increased as the concentration of humic acid increased. For pristine DWCNTs, the LC₅₀ at 0 mg/L humic acid was 113.64 mg/L and at the highest humic acid concentration, it was 3.64 mg/L (Table 3).

Fish have been reported to ingest CNTs through the gastric tract. The amount of ingested CNTs depends on the colloidal stability of ENMs in solution [21]. The high agglomeration of DWCNTs at high ionic strengths (Figures 2

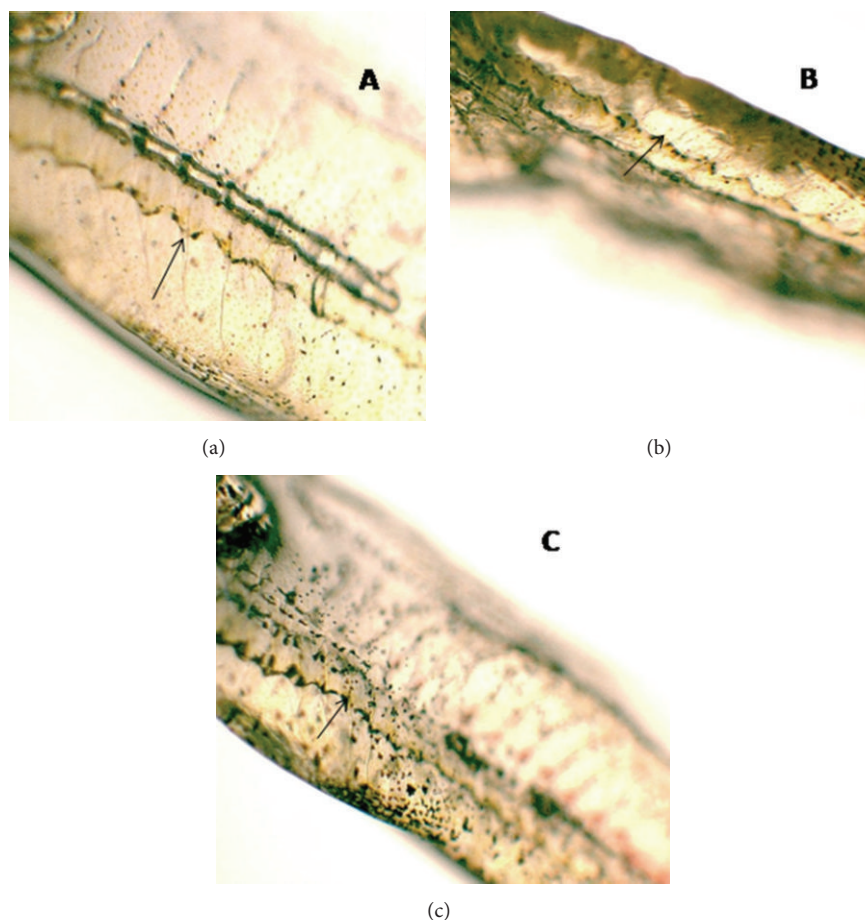


FIGURE 11: Pictures illustrating the gut of fish exposed to fish medium only (a), to 62.5 mg/L DWCNTs (b), and to 250 mg/L DWCNTs (c).

and 3) removed some of the test material through the settling of DWCNTs at the bottom of the exposure vessels. However, when humic acid was added to exposure experiments, it stabilised some of the DWCNTs in solution and this has been reported to increase the concentration of DWCNTs per unit volume in the water column, increasing the probability of the ingestion of DWCNTs by the fish [52]. This may be the reason for the slight increase in toxicity of the DWCNTs when there are some stabilised CNTs in solution. Figure 11 shows the digestive tract of *P. reticulata* that were exposed to DWCNT suspensions. It can be noted that the amount of DWCNTs increases when the exposure concentration increases.

Freshwater fish such as *P. reticulata* has water intake proportional to their body mass at a given time [53]. Studies on medaka and rainbow trout demonstrated the presence of nanoparticles, including CNTs, in the gut of fish [54, 55]. Such data suggest that while drinking water, freshwater fish ingest nanoparticles. The internalised nanoparticles lead to stress-induced drinking, consequently leading to an increased amount of internalised nanoparticles [53]. This uptake mechanism is dependent on the aggregation state of DWCNTs [10, 53, 55]. The agglomeration of DWCNTs removed some of the test material through the settling of DWCNTs at the bottom of the exposure vessels. The addition

of humic acid in exposure experiments stabilised some of the DWCNTs in solution and this has been reported to increase the amount of carbon nanoparticles internalised by the fish [42, 55]. The acute toxicity of both pristine and oxidised DWCNTs in increased humic acid content increased because *P. reticulata* ingested more DWCNTs and DWCNT aggregates with lower hydrodynamic sizes.

The stabilisation of DWCNTs in the water column by humic acid increases the probability of contact between fish and nanoparticles through diet, hence the slight increase in toxicity [55]. Capping agents such as natural organic matter, tannic acid, Tween 20, and gum Arabic (GA) have been reported to have an effect on the toxicity of ENMs such as MWCNTs [35, 56–58]. These dispersants or capping agents alter the ENM-cell contact opportunities and consequently alter the toxicity of such materials [55]. In the gut, DWCNTs are likely to be trapped in the mucus layer of the gut, increasing the likelihood that the DWCNTs will interact with the apical surface of the epithelium, hence the slight increase in toxicity. Gill mucus of rainbow trout trapped SWCNTs and increased gill pathology [54]. In this scenario, the surface charge, whether anionic or cationic, does not determine the interaction of the nanoparticles and cells. The nonspherical shape of DWCNTs enables them to get

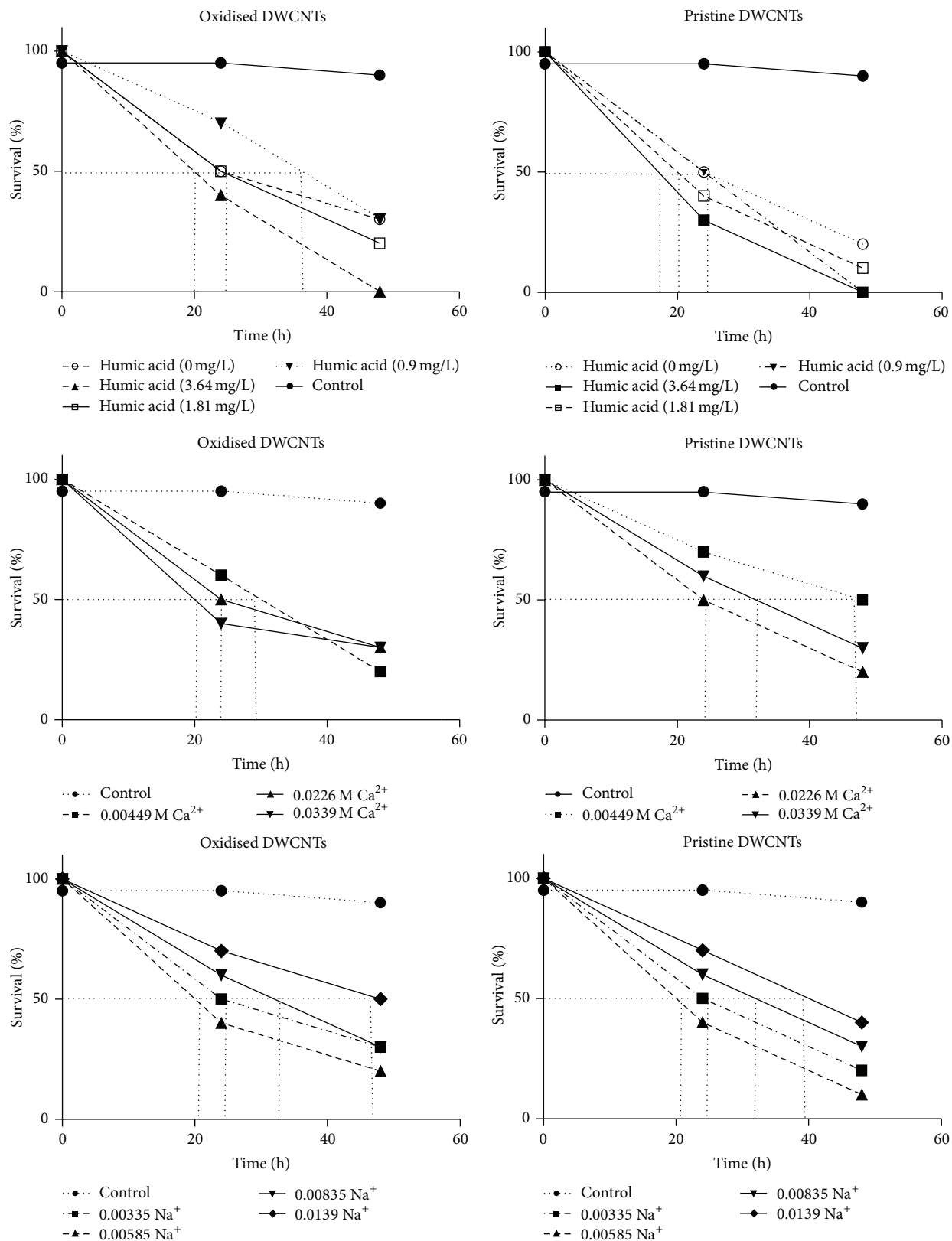


FIGURE 12: Survival of *D. pulex* at set time intervals for the different exposure conditions.

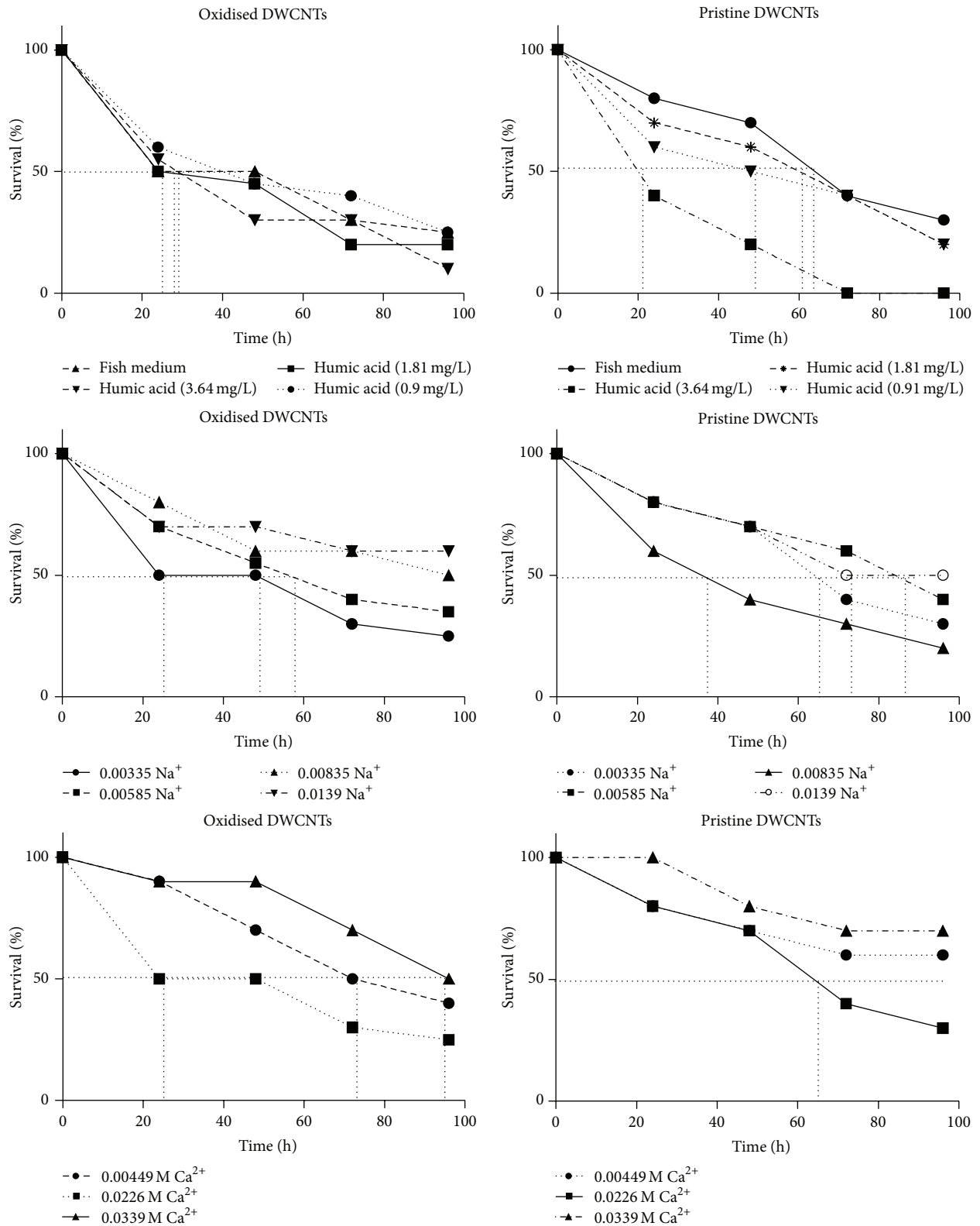


FIGURE 13: Survival of *P. reticulata* at set time intervals for the different exposure conditions.

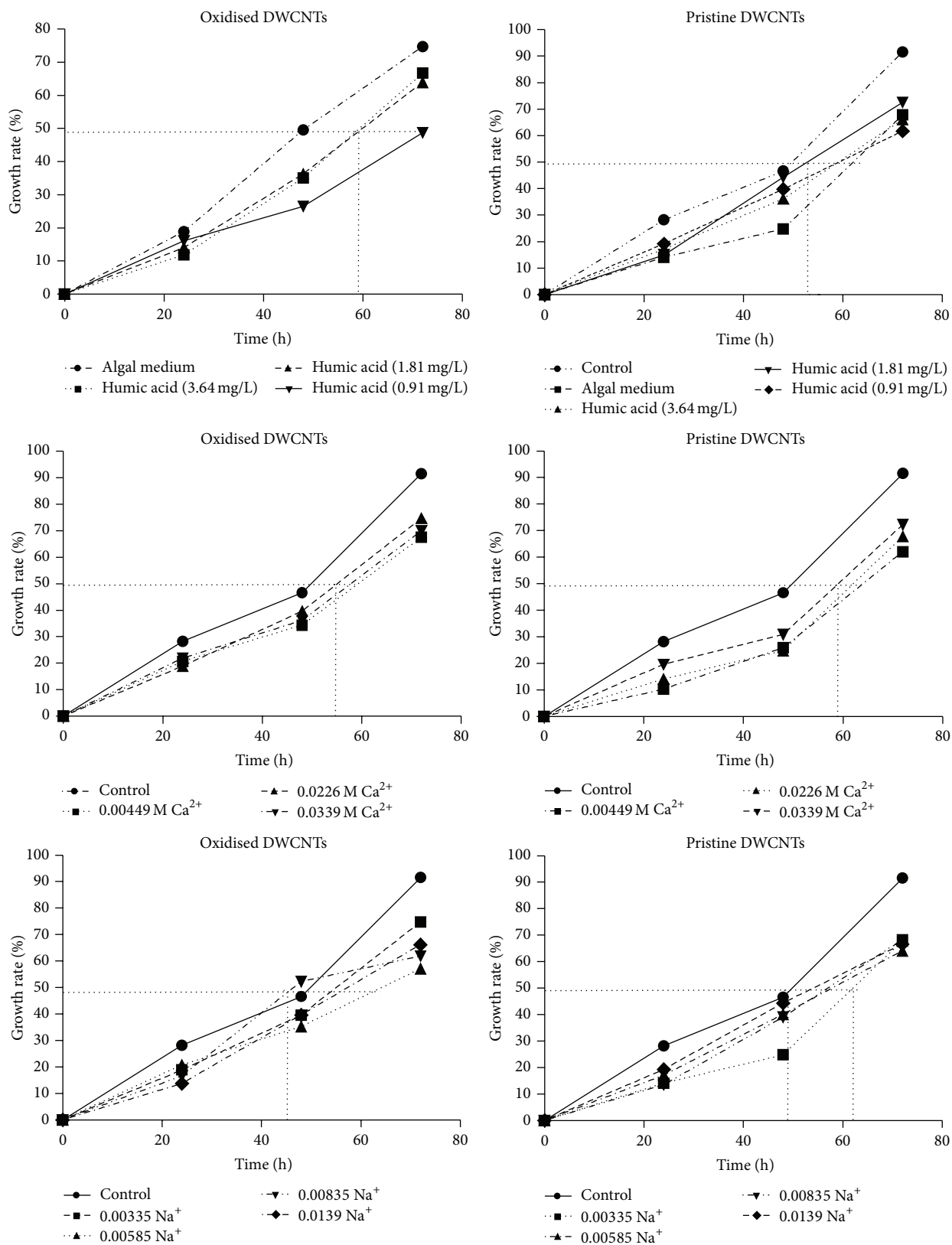


FIGURE 14: Growth rate *P. subcapitata* at set time intervals for the different exposure conditions.

entangled with mucus strands leading to their interaction with cells [55]. Elemental analysis using EDX revealed that DWCNTs contained residual molybdenum catalyst and it could be argued that toxicity of DWCNTs is partly due to residual metal catalysis. However, these metal particles are normally embedded within the tube or particle and their removal using harsh acid treatment is difficult [44, 47, 48, 59]. In such situations, the probability for metal catalysts leaching into exposure medium is quite low. Bennett and coworkers reported that less than 1% of metal residue leached from purified SWCNTs and the leached metals had no effect on the toxicity of SWCNTs to aquatic organisms [45].

The inverse was observed in the case of increased ionic strengths where LC_{50} s were found to be higher than 500 mg/L. This is because DWCNTs in these conditions formed larger aggregates that settled at the bottom of the flask and *P. reticulata* ingested fewer suspended DWCNTs or the gill surfaces were not in contact with the DWCNTs.

3.8. Time-Based Acute Toxicity of DWCNTs to *D. pulex*, *P. reticulata*, and *P. subcapitata*. Acute toxicity can also be expressed using cumulative mortalities/survival plotted over time. These plots often illustrate whether a toxicant is toxic to part of the population within a certain period during the exposure experiment or whether mortality occurs at different rates within the exposure period.

The cumulative survival of *D. pulex* within each exposure experiment under the various conditions is shown in Figure 12.

At the beginning of the exposures, the percentage survival of *D. pulex* population within each test was 100%. The highest humic acid concentration resulted in a decrease in percentage survival of 50% (LC_{50}) in 18 h and 20 h for both pristine and oxidised DWCNTs, respectively, and both reached 0% by the end of 48 h. In the ionic strength treatments, the 0.0339 M Ca^{2+} and 0.0226 M Ca^{2+} treatments resulted in a percentage survival of 50% in 20 h and 24 h, respectively, for oxidised DWCNTs while for pristine DWCNTs, the 0.0226 M Ca^{2+} treatment, 50% survival was reached in 24 h. For all the treatments, the toxicity of DWCNTs did not cease after the initial die-off.

The *P. reticulata* negative control had a 100% survival for the first 72 h and at the end of exposure experiments, the percentage survival was at 95% (Figure 13). The highest humic acid concentration (3.64 mg/L) resulted in a decrease in percentage survival of 50% (LC_{50}) in 21 h for both pristine DWCNTs and all oxidised DWCNTs humic acid treatments reached 50% survival within 30 h. In the ionic strength treatments, the 0.0226 M Ca^{2+} treatments resulted in a percentage survival of 50% in 24 h while the rest of the ionic treatments took longer to reach 50% mortalities.

The algal growth rates for all treatments and negative control reached 50% after 40 h (Figure 14). For both pristine and oxidised DWCNTs, the lowest growth rate was observed at a humic acid concentration of 0.9 mg/L while growth rates comparable to that of the negative control were observed at the highest humic acid concentration. The ionic strength of 0.00449 M Ca^{2+} treatment produced 50% growth rates

between 50 h and 60 h for both pristine and oxidised DWCNTs. The 0.00335 M Na^+ ionic strength treatment showed the lowest growth rate reaching the 50% growth rate mark at 62 h. The growth rates observed during all other treatments were similar to that of the negative control. Over prolonged exposure to SWCNTs, *P. subcapitata* growth rates decreased and later recovered [42]. However, the concentrations of SWCNTs were below 1 mg/L.

Time-response acute toxicity plots are essential in highlighting the effect of a particular toxicant over the set period of exposure. These plots, however, are not common in nanoecotoxicity tests. The time-response plots for the three organisms show that toxicity of DWCNTs proceeds at varying rates throughout the exposure periods. None of the plots showed point of inflection which further illustrates that DWCNTs are not just toxic to that part of the test population that was exposed.

4. Conclusion

The toxicity of DWCNTs to the three organisms was found to be significantly different, with *D. pulex* being the most sensitive followed by *P. subcapitata* and *P. reticulata* being the least sensitive. The multitrophic approach provides information on the potential impact of DWCNTs on aquatic environments at concentrations ranging from 2 to 500 mg/L. The mode of interaction of DWCNTs and organisms was found to play a significant role in the toxicity of DWCNTs. The agglomeration of double-walled carbon nanotubes entrapped *P. subcapitata* cells and deprived the cells of light. The light deprivation resulted in growth inhibition of the algal cells. In *D. pulex* and *P. reticulata*, the DWCNTs interacted with these organisms via their gut tracts. Humic acid increased the toxicity of DWCNTs to *D. pulex* and *P. reticulata* while increased ionic strength reduced the toxicity of DWCNTs to these organisms. Both humic acid and increased ionic strength reduced the toxicity of DWCNTs in *P. subcapitata*. The effect of the abovementioned parameters was found to be a direct consequence of their impact in the aggregation state of DWCNTs. The toxicity of DWCNTs proceeded at varying rates throughout the exposure periods for all organisms. There were no abrupt die-offs observed at the initial stages of exposure for all three organisms.

Conflict of Interests

The authors declare that there is no conflict of interests regarding the publication of this paper.

References

- [1] A. Aqel, K. M. M. A. El-Nour, R. A. A. Ammar, and A. Al-Warthan, "Carbon nanotubes, science and technology part (I) structure, synthesis and characterisation," *Arabian Journal of Chemistry*, vol. 5, no. 1, pp. 1–23, 2012.
- [2] S. Osswald, E. Flahaut, H. Ye, and Y. Gogotsi, "Elimination of D-band in Raman spectra of double-wall carbon nanotubes by oxidation," *Chemical Physics Letters*, vol. 402, no. 4–6, pp. 422–427, 2005.

- [3] J. N. Coleman, U. Khan, W. J. Blau, and Y. K. Gun'ko, "Small but strong: a review of the mechanical properties of carbon nanotube-polymer composites," *Carbon*, vol. 44, no. 9, pp. 1624–1652, 2006.
- [4] K. W. Kwok, K. M. Leung, E. Flahaut, J. Cheng, and S. H. Cheng, "Chronic toxicity of double-walled carbon nanotubes to three marine organisms: influence of different dispersion methods," *Nanomedicine*, vol. 5, no. 6, pp. 951–961, 2010.
- [5] N. Musee, "Nanowastes and the environment: potential new waste management paradigm," *Environment International*, vol. 37, no. 1, pp. 112–128, 2011.
- [6] E. Flahaut, C. Laurent, and A. Peigney, "Catalytic CVD synthesis of double and triple-walled carbon nanotubes by the control of the catalyst preparation," *Carbon*, vol. 43, no. 2, pp. 375–383, 2005.
- [7] V. Stone, B. Nowack, A. Baun et al., "Nanomaterials for environmental studies: classification, reference material issues, and strategies for physico-chemical characterisation," *Science of the Total Environment*, vol. 408, no. 7, pp. 1745–1754, 2010.
- [8] A. Fairbrother and J. R. Fairbrother, "Are environmental regulations keeping up with innovation? A case study of the nanotechnology industry," *Ecotoxicology and Environmental Safety*, vol. 72, no. 5, pp. 1327–1330, 2009.
- [9] M. C. Roco, B. Harthorn, D. Guston, and P. Shapira, "Innovative and responsible governance of nanotechnology for societal development," *Journal of Nanoparticle Research*, vol. 13, no. 9, pp. 3557–3590, 2011.
- [10] R. D. Handy, G. Cornelis, T. Fernandes et al., "Ecotoxicity test methods for engineered nanomaterials: practical experiences and recommendations from the bench," *Environmental Toxicology and Chemistry*, vol. 31, no. 1, pp. 15–31, 2012.
- [11] M. Crane, R. D. Handy, J. Garrod, and R. Owen, "Ecotoxicity test methods and environmental hazard assessment for engineered nanoparticles," *Ecotoxicology*, vol. 17, no. 5, pp. 421–437, 2008.
- [12] K. Aschberger, C. Micheletti, B. Sokull-Klüttgen, and F. M. Christensen, "Analysis of currently available data for characterising the risk of engineered nanomaterials to the environment and human health—lessons learned from four case studies," *Environment International*, vol. 37, no. 6, pp. 1143–1156, 2011.
- [13] R. A. Becker, L. M. Plunkett, J. F. Borzelleca, and A. M. Kaplan, "Tiered toxicity testing: evaluation of toxicity-based decision triggers for human health hazard characterization," *Food and Chemical Toxicology*, vol. 45, no. 12, pp. 2454–2469, 2007.
- [14] S. L. Harper, J. L. Carriere, J. M. Miller, J. E. Hutchison, B. L. S. Maddux, and R. L. Tanguay, "Systematic evaluation of nanomaterial toxicity: utility of standardized materials and rapid assays," *ACS Nano*, vol. 5, no. 6, pp. 4688–4697, 2011.
- [15] M. Farré, K. Gajda-Schranz, L. Kantiani, and D. Barceló, "Ecotoxicity and analysis of nanomaterials in the aquatic environment," *Analytical and Bioanalytical Chemistry*, vol. 393, no. 1, pp. 81–95, 2009.
- [16] B. Orthen, *Nanotechnology: Health and Environmental Risks of Nanomaterials—Research Strategy*, Bundesanstalt für Arbeitsschutz und Arbeitsmedizin (BAuA), Dortmund, Germany, 2007.
- [17] I. Blinova, A. Ivask, M. Heinlaan, M. Mortimer, and A. Kahru, "Ecotoxicity of nanoparticles of CuO and ZnO in natural water," *Environmental Pollution*, vol. 158, no. 1, pp. 41–47, 2010.
- [18] A. Baun, N. B. Hartmann, K. Grieger, and K. O. Kusk, "Ecotoxicity of engineered nanoparticles to aquatic invertebrates: a brief review and recommendations for future toxicity testing," *Ecotoxicology*, vol. 17, no. 5, pp. 387–395, 2008.
- [19] J. I. E. Gao, S. Youn, A. Hovsepian et al., "Dispersion and toxicity of selected manufactured nanomaterials in natural river water samples: effects of water chemical composition," *Environmental Science & Technology*, vol. 43, no. 9, pp. 3322–3328, 2009.
- [20] K. van Hoecke, K. A. C. de Schamphelaere, P. van der Meeren, S. Lucas, and C. R. Janssen, "Ecotoxicity of silica nanoparticles to the green alga *Pseudokirchneriella subcapitata*: importance of surface area," *Environmental Toxicology and Chemistry*, vol. 27, no. 9, pp. 1948–1957, 2008.
- [21] B. J. Shaw and R. D. Handy, "Physiological effects of nanoparticles on fish: a comparison of nanometals versus metal ions," *Environment International*, vol. 37, no. 6, pp. 1083–1097, 2011.
- [22] OECD, *OECD Guidelines for the Testing of Chemicals 201: Freshwater Alga and Cyanobacteria, Growth Inhibition Test*, 2002.
- [23] OECD, *OECD Guidelines for the Testing of Chemicals 202: Daphnia sp., Acute Immobilisation Test and Reproduction Test*, OECD, 2004.
- [24] OECD, "203: fish, acute toxicity test," in *OECD Guidelines for Testing of Chemicals*, pp. 1–10, 2002.
- [25] United States Environmental Protection Agency (USEPA), *Probit Program. Version 1.5*, Ecological Monitoring Research Division, Environmental Monitoring Systems Laboratory, 1991.
- [26] M. A. Hamilton, R. C. Russo, and R. V. Thurston, "Trimmed Spearman Karber method for estimating median lethal concentrations in toxicity bioassays," *Environmental Science & Technology*, vol. 11, no. 7, pp. 714–719, 1977.
- [27] APHA, *Standard Methods for the Examination of Water and Wastewater*, American Public Health Association (APHA), Washington, DC, USA, 1992.
- [28] C. Desai, S. A. Ntim, and S. Mitra, "Antisolvent precipitation of hydrophobic functionalized multiwall carbon nanotubes in an aqueous environment," *Journal of Colloid and Interface Science*, vol. 368, no. 1, pp. 115–120, 2012.
- [29] B. Smith, K. Wepasnick, K. E. Schrote et al., "Colloidal properties of aqueous suspensions of acid-treated, multi-walled carbon nanotubes," *Environmental Science and Technology*, vol. 43, no. 3, pp. 819–825, 2009.
- [30] R. Barrena, E. Casals, J. Colón, X. Font, A. Sánchez, and V. Puentes, "Evaluation of the ecotoxicity of model nanoparticles," *Chemosphere*, vol. 75, no. 7, pp. 850–857, 2009.
- [31] A. Schierz and H. Zänker, "Aqueous suspensions of carbon nanotubes: surface oxidation, colloidal stability and uranium sorption," *Environmental Pollution*, vol. 157, no. 4, pp. 1088–1094, 2009.
- [32] I. Schwyzer, R. Kaegi, L. Sigg, R. Smajda, A. Magrez, and B. Nowack, "Long-term colloidal stability of 10 carbon nanotube types in the absence/presence of humic acid and calcium," *Environmental Pollution*, vol. 169, pp. 64–73, 2012.
- [33] I. Schwyzer, R. Kaegi, L. Sigg, and B. Nowack, "Colloidal stability of suspended and agglomerate structures of settled carbon nanotubes in different aqueous matrices," *Water Research*, vol. 47, no. 12, pp. 3910–3920, 2013.
- [34] M. M. Alloy and A. P. Roberts, "Effects of suspended multi-walled carbon nanotubes on daphnid growth and reproduction," *Ecotoxicology and Environmental Safety*, vol. 74, no. 7, pp. 1839–1843, 2011.
- [35] H. Hyung and J.-H. Kim, "Natural organic matter (NOM) adsorption to multi-walled carbon nanotubes: effect of NOM characteristics and water quality parameters," *Environmental Science and Technology*, vol. 42, no. 12, pp. 4416–4421, 2008.

- [36] X. Ren, C. Chen, M. Nagatsu, and X. Wang, "Carbon nanotubes as adsorbents in environmental pollution management: a review," *Chemical Engineering Journal*, vol. 170, no. 2-3, pp. 395-410, 2011.
- [37] N. B. Saleh, L. D. Pfefferle, and M. Elimelech, "Influence of biomacromolecules and humic acid on the aggregation kinetics of single-walled carbon nanotubes," *Environmental Science & Technology*, vol. 44, no. 7, pp. 2412-2418, 2010.
- [38] X. Wang, L. Shu, Y. Wang et al., "Sorption of peat humic acids to multi-walled carbon nanotubes," *Environmental Science and Technology*, vol. 45, no. 21, pp. 9276-9283, 2011.
- [39] D. Lin and B. Xing, "Tannic acid adsorption and its role for stabilizing carbon nanotube suspensions," *Environmental Science and Technology*, vol. 42, no. 16, pp. 5917-5923, 2008.
- [40] I. Schwyzer, R. Kaegi, L. Sigg, A. Magrez, and B. Nowack, "Influence of the initial state of carbon nanotubes on their colloidal stability under natural conditions," *Environmental Pollution*, vol. 159, no. 6, pp. 1641-1648, 2011.
- [41] V. Datsyuk, P. Landois, J. Fitremann et al., "Double-walled carbon nanotube dispersion via surfactant substitution," *Journal of Materials Chemistry*, vol. 19, no. 18, pp. 2729-2736, 2009.
- [42] S. Youn, R. Wang, J. Gao et al., "Mitigation of the impact of single-walled carbon nanotubes on a freshwater green algae: *Pseudokirchneriella subcapitata*," *Nanotoxicology*, vol. 6, no. 2, pp. 161-172, 2012.
- [43] Z. Long, J. Ji, K. Yang, D. Lin, and F. Wu, "Systematic and quantitative investigation of the mechanism of carbon nanotubes' toxicity toward algae," *Environmental Science & Technology*, vol. 46, no. 15, pp. 8458-8466, 2012.
- [44] F. Schwab, T. D. Bucheli, L. P. Lukhele et al., "Are carbon nanotube effects on green algae caused by shading and agglomeration?" *Environmental Science & Technology*, vol. 45, no. 14, pp. 6136-6144, 2011.
- [45] S. W. Bennett, A. Adeleye, Z. Ji, and A. A. Keller, "Stability, metal leaching, photoactivity and toxicity in freshwater systems of commercial single wall carbon nanotubes," *Water Research*, vol. 47, no. 12, pp. 4074-4085, 2013.
- [46] L. Wei, M. Thakkar, Y. Chen, S. A. Ntim, S. Mitra, and X. Zhang, "Cytotoxicity effects of water dispersible oxidized multi-walled carbon nanotubes on marine alga, *Dunaliella tertiolecta*," *Aquatic Toxicology*, vol. 100, no. 2, pp. 194-201, 2010.
- [47] X. Zhu, L. Zhu, Y. Chen, and S. Tian, "Acute toxicities of six manufactured nanomaterial suspensions to *Daphnia magna*," *Journal of Nanoparticle Research*, vol. 11, no. 1, pp. 67-75, 2009.
- [48] A. J. Kennedy, M. S. Hull, J. A. Steevens et al., "Factors influencing the partitioning and toxicity of nanotubes in the aquatic environment," *Environmental Toxicology and Chemistry*, vol. 27, no. 9, pp. 1932-1941, 2008.
- [49] A. J. Edgington, A. P. Roberts, L. M. Taylor et al., "The influence of natural organic matter on the toxicity of multiwalled carbon nanotubes," *Environmental Toxicology and Chemistry*, vol. 29, no. 11, pp. 2511-2518, 2010.
- [50] E. J. Petersen, J. Akkanen, J. V. K. Kukkonen, and W. J. Weber Jr., "Biological uptake and depuration of carbon nanotubes by *Daphnia magna*," *Environmental Science and Technology*, vol. 43, no. 8, pp. 2969-2975, 2009.
- [51] A. Feswick, R. J. Griffitt, K. Siebein, and D. S. Barber, "Uptake, retention and internalization of quantum dots in *Daphnia* is influenced by particle surface functionalization," *Aquatic Toxicology*, vol. 130-131, pp. 210-218, 2013.
- [52] R. D. Handy, T. B. Henry, T. M. Scown, B. D. Johnston, and C. R. Tyler, "Manufactured nanoparticles: their uptake and effects on fish—a mechanistic analysis," *Ecotoxicology*, vol. 17, no. 5, pp. 396-409, 2008.
- [53] R. D. Handy, F. von der Kammer, J. R. Lead, M. Hassellöv, R. Owen, and M. Crane, "The ecotoxicology and chemistry of manufactured nanoparticles," *Ecotoxicology*, vol. 17, no. 4, pp. 287-314, 2008.
- [54] A. A. Sharbidre, V. Metkari, and P. Patode, "Effect of methyl parathion and chlorpyrifos on certain biomarkers in various tissues of guppy fish, *Poecilia reticulata*," *Pesticide Biochemistry and Physiology*, vol. 101, no. 2, pp. 132-141, 2011.
- [55] C. J. Smith, B. J. Shaw, and R. D. Handy, "Toxicity of single walled carbon nanotubes to rainbow trout, (*Oncorhynchus mykiss*): respiratory toxicity, organ pathologies, and other physiological effects," *Aquatic Toxicology*, vol. 82, no. 2, pp. 94-109, 2007.
- [56] S. J. Klaine, P. J. J. Alvarez, G. E. Batley et al., "Nanomaterials in the environment: behavior, fate, bioavailability, and effects," *Environmental Toxicology and Chemistry*, vol. 27, no. 9, pp. 1825-1851, 2008.
- [57] P.-H. Chen, K.-M. Hsiao, and C.-C. Chou, "Molecular characterization of toxicity mechanism of single-walled carbon nanotubes," *Biomaterials*, vol. 34, no. 22, pp. 5661-5669, 2013.
- [58] H. Hyung, J. D. Fortner, J. B. Hughes, and J.-H. Kim, "Natural organic matter stabilizes carbon nanotubes in the aqueous phase," *Environmental Science and Technology*, vol. 41, no. 1, pp. 179-184, 2007.
- [59] J.-F. Colomer, L. Henrard, E. Flahaut, G. van Tendeloo, A. A. Lucas, and P. Lambin, "Rings of double-walled carbon nanotube bundles," *Nano Letters*, vol. 3, no. 5, pp. 685-689, 2003.